Quantum dot solar cells and electrochemical doping of QD films

Abiseka Akash Ganesan

TU Delft
Delft
University of
Technology

Challenge the future

Quantum dot solar cells and electrochemical doping of QD films

by

Abiseka Akash Ganesan

in partial fulfillment of the requirements for the degree of

Master of Science
in Sustainable Energy Technology

at the Delft University of Technology,
to be defended publicly on Tuesday July 4, 2018 at 01:00 PM.

Supervisor:	Dr. R. W. Crisp	
Thesis committee:	Prof. A. H. M. Smets,	TU Delft, PVMD, EEMCS
	Dr. A. J. Houtepen,	TU Delft, OM group, ChemE
	Dr. T. J. Savenije,	TU Delft, OM group, ChemE

This thesis is confidential and cannot be made public until December 31, 2018.

An electronic version of this thesis is available at http://repository.tudelft.nl/.

TUDelft Delft University of Technology

Abstract

Quantum dots (QDs) are nano-crystal semiconductors (1-100 nm) in which charge carriers (electrons and holes) are confined in all 3 dimensions by potential barriers that cause them to behave differently from conventional bulk semiconductors. QD research in the past decade has progressed rapidly, allowing a deeper understanding of the physics behind the functioning and the effective synthesis of such materials. The wide spread opto-electronic applications of such QD semiconductors in LEDs, lasers, electrochemistry and solar cells with the potential to outperform traditional bulk semiconductors has fuelled inspired research in this field.

Quantum dot solar cells (QDSC) are solution-based third generation solar cells that possess the potential to overcome the Shockley-Queisser limit using multiple exciton generation (MEG). The large Bohr radius, wide bandgap tunability and large light absorption coefficients of PbS QDs have made them the most common material used in the absorber layer of such solar cells and shall also be the material used in this thesis. PbS QDs are used in conjunction with an n-type metal oxide to form a heterojunction that enhances charge separation at the interface. ZnO and TiO_2 are common metal oxides used for this purpose while different synthesis methods of the same metal has been observed to show different results. While different research groups have used different metal oxide layers, there has been no systematic study on the interaction of the metal oxide layer synthesized by different methods with the absorber layer. Such a study could help improve understanding of the heterojunction interface and shall be briefly looked into in this thesis. Another area of improvement in device performance is the depletion region across the heterojunction. Varying the doping of the n-type material affects the depletion width which has been explored in the past by adding impurity atoms to the metal oxide. However, the emergence of an alternate method to dope ZnO electrochemically has triggered an interesting novel pathway to integrate doped materials into solar cells. In this thesis, we have successfully fabricated PbS QD solar cells for the first time in TU Delft at the Synthesis lab of the Applied Sciences faculty with power conversion efficiencies exceeding 5%. Additionally, a systematic study on the absorber layer and the metal oxide layer was also carried out to optimize the device performance and set protocols for any future work. Finally, electrochemical doping of the PbS absorber layer was attempted to develop a precise doping mechanism for QD films.

Contents

List of Figures

List of Tables

List of Abbreviations

ACN Acetonitrile.

Ag Silver.

Au Gold.

AZO Aluminum doped zinc oxide.

CB Conduction band.

CBM Conduction band minimum.

CdO Cadmium oxide.

CdS Cadmium sulphide.

Cl$^-$ Chloride.

CM Carrier multiplication.

CQD Colloidal quantum dot.

DFT Density functional theory.

DMF N,N-Dimethylformamide.

E$_g$ Band gap energy.

ED Electrochemical doping.

EDT 1,2-ethanedithiol.

EQE External quantum efficiency.

ETL Electron transport layer.

F.F. Fill factor.

FTO Fluorine doped tin oxide.

FWHM Full width half maximum.

HOMO Highest occupied molecular orbital.

HTL Hole transport layer.

I$_2$ Iodine.

II Impact ionization.

InCl$_3$ Indium chloride.

ITO Indium doped tin oxide.

J$_{SC}$ Short circuit current density.

J-V curve Current density-Voltage curve.

LbL Layer by layer.

LCOE Levelized cost of electricity.

LP Lithium perchlorate.

LUMO Lowerst unoccupied molecular orbital.

MAI Methylammonium iodide.

MEG Multiple exciton generation.

MO Molecular orbital.

MoO$_x$ Molebdenum oxide.

MPA 3-mercaptopropionic acid.

N$_2$ Nitrogen.

NC Nanocrystal.

ODE 1-Octadecene.

OLA Oleylamine.

PbCl$_2$ Lead chloride.

PbI$_2$ Lead Iodide.

PbS Lead sulphide.

PCE Power conversion efficiency.

PL Photoluminescence.

PLQY Photoluminescence quantum yield.

PV Photo voltaics.

QD Quantum dot.

QDSC Quantum dot solar cell.

RH Relative humidity.

SQ Shockley Queisser.

TBAI Tetrabutylammonium iodide.

TCO Transparent conductive oxide.

TiO$_2$ Titanium dioxide.

TMS$_2$S bis-Trimethylsilyl sulphur.

TOP-S Trioctylphosphine sulpur.

TRMC Time resolved microwave conductivity.

UV Ultra violet.

V$_{oc}$ Open circuit voltage.

VB Valence band.

ZnO Zinc oxide.

1

Introduction

1.1. Background

Energy consumption across the world has steadily been on the rise over the last few decades due to the increasing population and improved quality of life. As seen in Figure 1.1a, the predicted 28 % increase in worldwide energy requirement by 2040 (as compared to 20151), makes it an uphill task for us to meet this significant increase in energy demand. Currently, fossil fuels are burnt to meet a substantial part of this energy demand[1] which has led to large spikes in global pollution and temperatures[2]. However, increased awareness about the environment has also led to the widespread adoption of renewable energy resources: the year 2016 saw an addition of 136 GW of renewable energy capacity (excluding hydro energy); the global installed capacity of solar photovoltaics (PV) grew by 75 GW[3, 4] and the Paris Climate Treaty was ratified in November 2016 which limits its signed members to curtail global temperature rise to below 2°C above that of the pre-industrial levels[5]. To achieve the targets set by this treaty, countries have begun developing robust environmental policies and promoting research and development in every field of sustainable energy. A few nations in the European Union have henceforth, decided to reduce their carbon foot print by banning fossil fuel driven cars in the coming decade while other countries have focussed on driving down the price of sustainable technologies to increase the chances of their diffusion into the energy market. Since the discovery of PV cells in 1956 by Bell Labs, USA, the efficiency of silicon PV cells, the most common solar cells, have risen from 6%[6] to a current record of 26.63%[7] and their cost has fallen from $76 per watt[8] to $0.22 per watt[9]. This unprecedented drop in prices of solar cells has been attributed to China's heightened commitment in the recent years to increase the share of renewables in its energy mix as emphasized by the exponential growth in China's PV installed capacity seen in Figure 1.1b. Cheap labour and strict laws have led to the emergence of China as the world leader in the implementation of renewable energy[3] followed by a flooding of the PV market with cheap solar cells. This has resulted in a 73% drop in the levelized cost of electricity (LCOE) of utility-scale PVs from 2010[10] making it one of the most attractive renewable energy technologies. However, silicon PV's bulky nature and technological limitations make it desirable to look for alternate PV materials. Second generation solar cells, also known as thin film solar cells have shown promise to negate the bulkiness of silicon solar cells. However, their inability to beat the Shockley Queisser limit (SQ limit) has encouraged researchers to investigate third generation solar cell technologies, one of which is the use of solution-based synthesis of nanocrystal (NC) materials as the light absorber in solar cells. This thesis explores past efforts at fabricating such solar cells and tries a novel method at improving their performance.

1.2. Motivation

The SQ limit gives the maximum theoretical efficiency of a single junction solar cell under 1 sun condition. For a semiconductor with a bandgap of 1.1 eV bandgap, this limit has been calculated to be 33% under AM1.5 solar spectrum[11]. As seen in Figure 1.2, thermalization losses due to the cooling of excited, high energy electrons contribute the most towards power loss in solar cells while the remaining losses are split between losses due to photons with energies below bandgap and losses while extracting

(a)   (b)
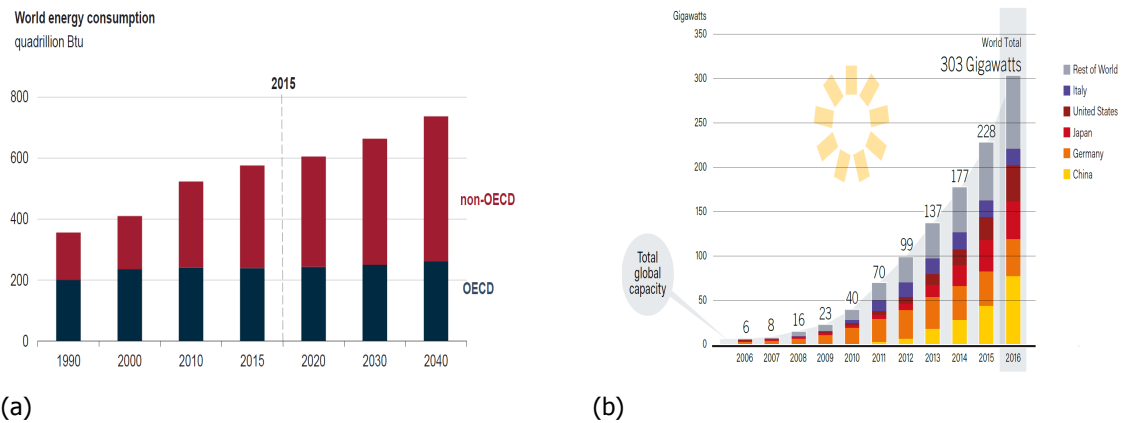
Figure 1.1: a. Expected increase of 28% in world energy consumption from 580 quadrillion British thermal units (BTU) to 740 BTU, [1]. b. Increase in global installed capacity of PV. 85 % of the 75GW of PV installed in 2016 was contributed by China which shows it commitment to renewable energy[3]
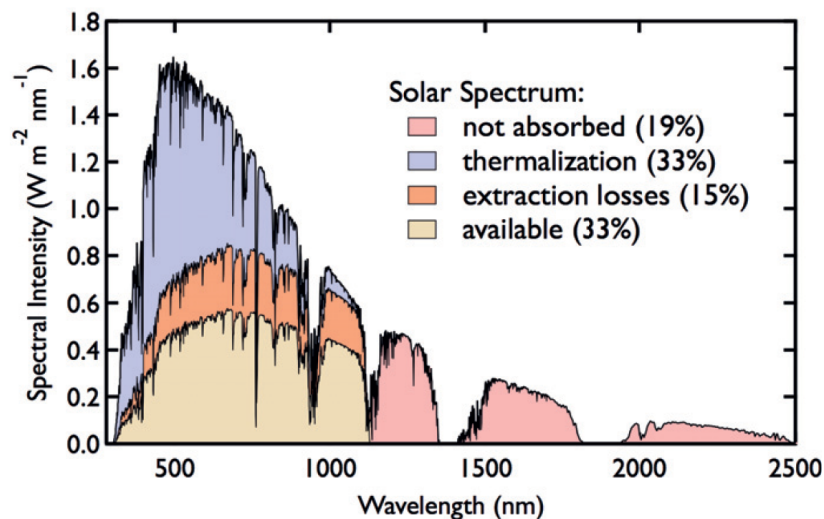
Figure 1.2: Spectral analysis of the power loss in a semiconductor with a band gap of 1.1eV. While cooling of high energy electrons to the bandgap (thermalization) contributes the most to power loss in solar cells, 15 % of the power lost is due to inevitable thermodynamic losses involved in the extraction of photo excited charge carriers that give rise to losses in the open circuit voltage. Reprinted from reference[13], copyright Elsevier Ltd. 2012.

photoexcited electrons. However, third generation solar cell concepts look at overcoming these limitations to further push the efficiency limit of solar cells. Tandem PVs which use multiple semiconductor materials to more effectively utilize the entire solar spectrum, and concentrated solar PVs that focus the sun's light are currently the two of the most prominent third-generation technologies[12]. Despite holding the world record power conversion efficiency (PCE), the proliferation of these technologies in the market has been impeded by high costs of manufacturing and thus relevance only to a niche market. This has led to a collective interest in realizing cheaper technologies that can overcome the SQ limit and compete with the current economies of scale achieved by silicon PV cells. Quantum dot solar cells (QDSC) are a relatively new third-generation solar cell concept that has gained popularity in the last decade due to its potential to meet both these requirements. Quantum Dots (QDs) are semiconductor nanocrystals (NCs) that exhibit quantum confinement effects in all three dimensions. These quantum confinement effects allow their optical and electronic properties to be tuned by adjusting their shape and size which makes their use in optoelectronic materials interesting[13, 14].

Quantum dot semiconductor materials have been shown to exhibit multiple exciton generation (MEG). Also known as carrier multiplication (CM), MEG is a process that produces more than one electron hole pair with the absorption of one photon. This provides a pathway to reduce one of the

thermodynamic losses present in solar cells which in turn opens the possibility for QDSCs to exceed the SQ limit[15, 16]. The ability to synthesize these QD materials *via* solution based chemical reactions also provides a secondary impetus to this technology due to its possible application in roll to roll fabrication technologies that can be easily scaled up. With a current record PCE of 13.4%[17], this technology's potential to reach photo conversion efficiencies greater than 33% provide the primary motivation for research in QDSCs.

1.3. Research question

This thesis aims at developing a working application for the quantum dot research in the synthesis lab at the Applied Sciences faculty at TU Delft. Establishing a protocol for the fabrication of PbS QDSCs that can further be built upon to perform experiments was the primary goal of this thesis. Following this, two additional objectives were added to the goals of the thesis: a study on the metal oxide layer was adopted due to the lack of a systematic study on it in literature and an attempt to find a novel route to dope thin PbS QD films in a device. These goals and objectives led to the following research question :

" What are the major parameters that affect the development of lead sulphide quantum dot solar cells ? "
    The sub questions to be answered in the thesis are:

1. How does ambient moisture and ambient oxidation affect device performance ?

2. How does the thickness of the individual layers in the device affect device performance.

3. Why do the different synthesis methods of the metal oxide layer affect device performance in PbS QDSCs ?

4. Can quantum dot films be directly electrochemically doped in devices ? If so, how can we use electrochemical doping to make the PbS QD films more intrinsic (from their general n-type behaviour) ?

2

Theory

2.1. Semiconductors and quantum dots

Semiconductors are a class of materials that exhibit conductivities between metals and insulators. Elements like silicon (Si) and germanium (Ge) that occupy group IV in the periodic table are used as elemental semiconductors while elements in groups III and V, II and VI or IV and VI combine to form binary or ternary compound semiconductors. In elemental semiconductors, atoms are held together by covalent bonds that involve sharing of electrons with the neighbouring atoms. When several such atoms are covalently bonded to each other extending into an ordered array of atoms, the resulting structure is termed a crystal lattice. At temperatures above 0K, the bonds in a semiconductor crystal lattice begin to break giving rise to free electrons and points devoid of electrons also known as holes. These holes and electrons are called charge carriers in a semiconductor and the movement of these charge carriers gives rise to currents in a semiconductor[18, 19]. Figure 2.1 shows the formation of charge carriers in an atomic semiconductor lattice.
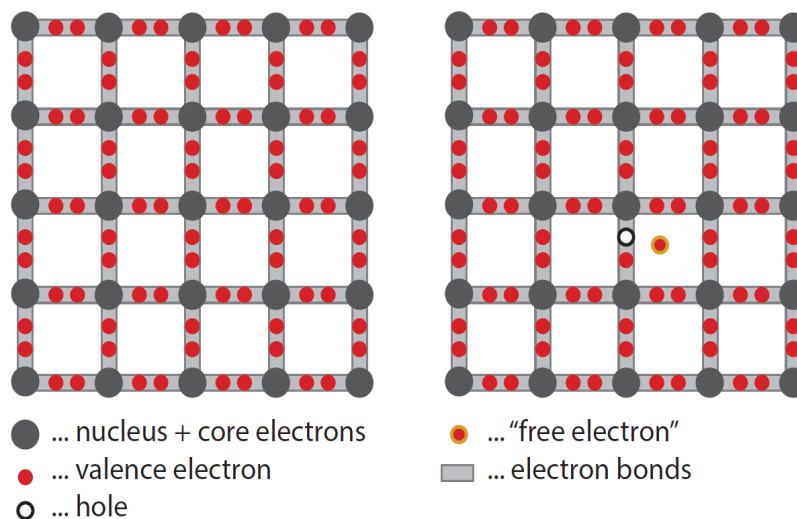
Figure 2.1: Covalent bonds in Si at T = 0 K (left) and T > 0 K (right). The free electron (unit negative charge) breaks out of its bonded state on gaining thermal energy, leaving behind a hole (unit positive charge). Reprinted from reference [18], copyright UIT Cambridge Ltd.

In quantum mechanics, an electron in space is described by its energy and its position, which is given by its wavefunction (Ψ). Considering an atom to be an infinite potential well and solving Schrodinger's equation for an electron in an infinite potential well, we obtain discreet energy levels where electrons are allowed to exist inside an atom. Any intermediate energy level is forbidden for the existence of an electron[19]. As per the molecular orbital theory, the bonding of 2 atoms leads to the interaction of their atomic orbitals (energy levels) that results in the formation of molecular orbitals

5

(MO). A constructive interaction of the wave functions of the atomic orbitals gives rise to a lower energy "bonding" MO while a destructive interaction of their wave functions gives rise to a relatively less stable, higher energy "anti-bonding" MO[20]. The splitting of these orbitals is also accompanied by the formation of intermediate forbidden energy levels between the two orbitals. When several such atoms arrange themselves in an ordered array to form a crystal lattice in an atomic semiconductor, the interaction of each atom with its neighbouring atoms gives rise to atomic orbital splitting with several bonding and anti-bonding MO separated by a distinct gap containing forbidden energy levels. When the density of atoms in the crystal is sufficiently high (in the order of 10^{22} cm^{-3}[21]), the spacing between consecutive MO in the bonding and the anti-bonding regions reduces so much that they can be considered to be a series of quasi-continuous energy levels also known as energy bands with a forbidden energy gap (E_g) separating the two regions. At 0K, all the electrons are at their lowest energy state and hence fill the lower energy band also known as "valence band" (VB) and at higher temperatures, more electrons gain thermal energy that excite them to the higher energy band also known as "conduction band" (CB). Due to this quasi-continuous nature of the "energy bands", charge carriers are considered to be delocalized throughout the energy band in such bulk semiconductors.
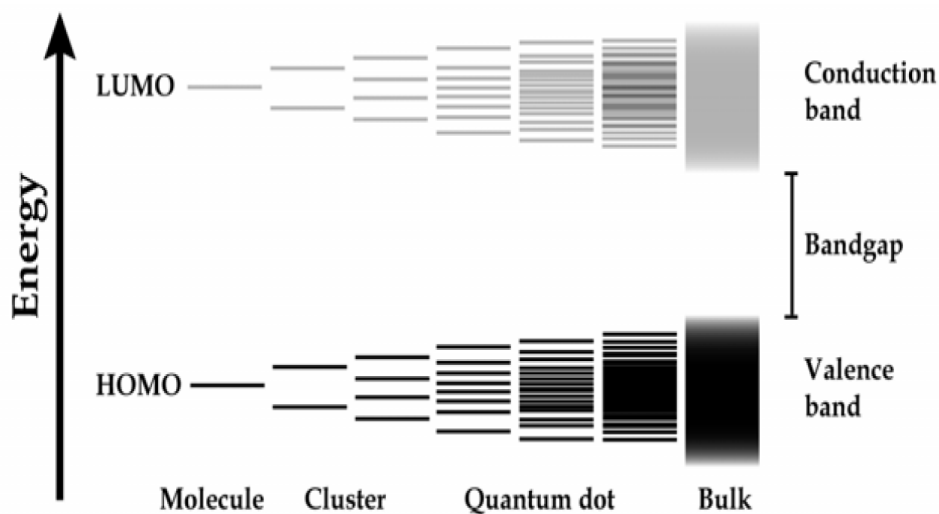
Figure 2.2: An increase in the number of energy states in a system by increasing the number of interacting atoms and a subsequent decrease in bandgap is seen from left to right. The quasi continuous system of energy states leading to a "band like" behaviour is observed in the bulk semiconductor. Reprinted with permission from reference [22].

According to this quantum mechanical model of energy band formation in semiconductors, the number of energy levels in each band reduces with a decrease in the number of atoms in the crystal lattice. When the number of atoms in the crystal reduces to about only a few thousand, the separation between each MO in a "band" is high enough that it can no longer be considered to be a series of quasi-continuous energy levels anymore but a series of discreet energy levels where electrons are localized. This gives rise to the quantum confinement of charged carriers. In addition, this decrease in the number of discreet energy levels from a bulk crystal also leads to an increase in the band gap separation between the highest occupied molecular orbital (HOMO) [also referred to as the valence band maximum] and the lowest unoccupied molecular orbital (LUMO) [also referred to as the conduction band minimum]. This increase in the band gap energy due to quantum confinement can increase by more than 1eV from the value in a bulk crystal[23]. Figure 2.2 shows the spectrum of semiconductors based on their sizes with QDs occupying the central position. QDs are semiconductors that contain between a few hundred and a few thousand atoms grouped together as a crystal in which charge carriers are confined to a small space by potential barriers on all three directions giving rise to quantum confinement effects[13, 16, 22].

Quantum confinement effects begin to show significance only when one dimension of an NC is smaller than the de Brooglie wavelength of electrons and holes[13] and the diameter of the NC is smaller than twice the Bohr's radius of excitons in a bulk crystal[16]. The de Brooglie wavelength of an electron (λ_e) is given by,

(a)   (b)
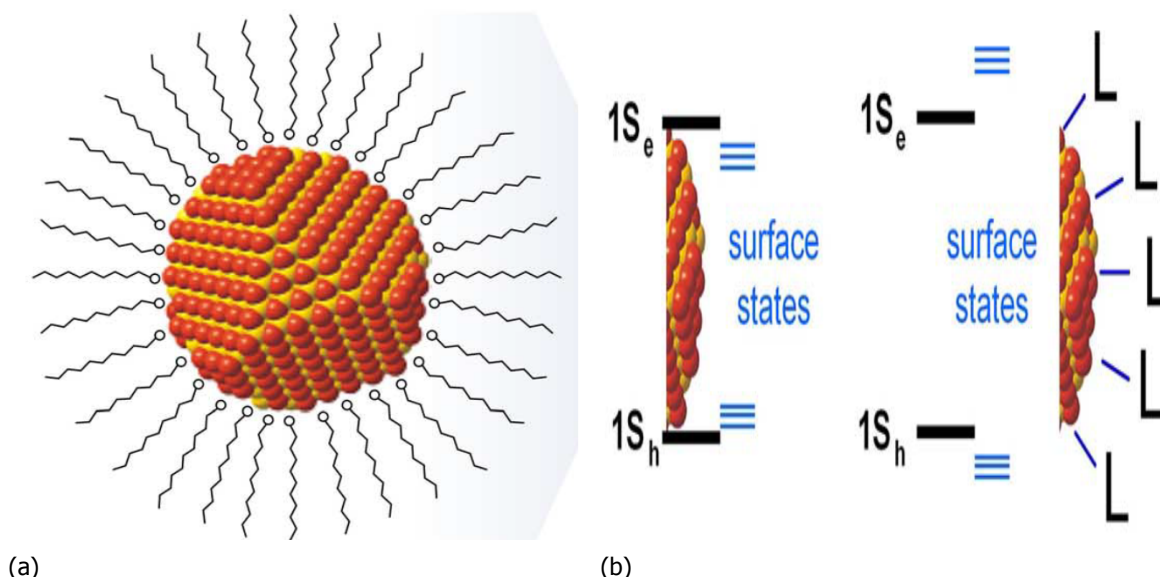
Figure 2.3: a. An inorganic QD core with long chain surfactant (ligand) molecules attached to the uncoordinated surface atoms. b. The passivation of surface states by the ligands (L) push mid band energy levels due to uncoordinated surface bonds into the conduction and valence "bands" and hence quench non-radiative recombination pathways for charge carriers. However, it is to be noted that the theory behind the position of trap states inside the band gap is highly debated and this picture may not depict the true position of trap states. Reprinted from reference [21], copyright AAAS 2016

$$\lambda_e = h/(m_{eff}kT) \qquad (2.1)$$

Where h is the Planck's constant, k is the Boltzmann's constant, T is the temperature and m_{eff} is the effective mass of an electron. Due to dimensions smaller than that of λ_e of carriers along all three axes in QDs, the wave function of charge carriers is spatially completely confined inside a QD. The Bohr's radius describes the distance of separation between a bound electron and a hole. When the size of crystal particles become smaller than the Bohr radius, the high electrostatic binding forces between the carriers prevent them from separating but instead, interact in a confined volume known as an exciton. This is unlike in a bulk crystal where the binding forces are weaker than kT (product of Boltzmann's constant and the temperature), that allows them to split easily. As a result of quantum confinement of carriers and the formation of excitons, the electronic behaviour of QD semiconductors is different from bulk semiconductors.

2.2. Charge transport in semiconductors

QDs have been synthesized since the early 1990s[24] with several improvements having been achieved in the synthesis methods over the years. QDs are synthesized predominantly *via* solution-based methods while vapor phase deposition based syntheses has also been reported in the past[16]. In the solution based synthesis, QD semiconductors are formed by the supersaturation of reaction products in a solution[25], allowed to grow to the required size, washed and then dispersed in a solvent. Long chain organic surfactants present in the solution terminate the QD surface and also aid in the dispersion of the inorganic QDs in a non-polar solvent. Due to their small size, QDs possesses a high surface-to-volume ratio which gives rise to the possibility of several uncoordinated surface atoms that act as recombination centres for charge carriers, also known as trap states. The surfactants (also known as ligands) passivate these surface trap states which gives rise to a series of new energy levels that align outside the forbidden energy gap as shown in Figures 2.3a and 2.3b[21].

To effect charge transport between QDs, ordered QD arrays are made through physical processing methods that evaporate the solvent and tightly pack the QDs next to each other to enable better electronic coupling[16, 21, 26]. In such an ordered film of QDs known as QD solids, neighbouring QDs are separated by ligands which makes charge carrier transport more complicated than in bulk semiconductors. The quasi continuous nature of energy levels in bulk semiconductors allow the diffusion of charge

carriers through the energy bands with a "band-like" transport. In QD films though, the transport of carriers between discreet energy levels from one QD to another has to occur through "carrier hopping" where carriers hop from one QD to the other which is equivalent to the quantum mechanical process of carrier tunnelling. The tunnelling rate is described by the equation[21]:

$$\Gamma \propto exp\left(-(2m^*\Delta E/\hbar^2)^{1/2}\Delta x\right) \tag{2.2}$$

where m* is the effective mass of the charge carrier, $\hbar$ is the reduced Planck's constant, ΔE is the height of the tunnelling barrier and Δx is the width of the tunnelling barrier, which in this case is the inter dot distance. In films of as prepared QD solutions, the long chain organic ligands that separate neighbouring QDs lead to large inter dot distances that inhibits efficient carrier transport. To overcome this limitation, the long chain insulating ligands are exchanged with shorter ligands which increases the tunnelling rate and enhances the electronic coupling between neighbouring QDs due to the direct relation between electronic coupling and the tunnelling rate[21].

(a)   (b)
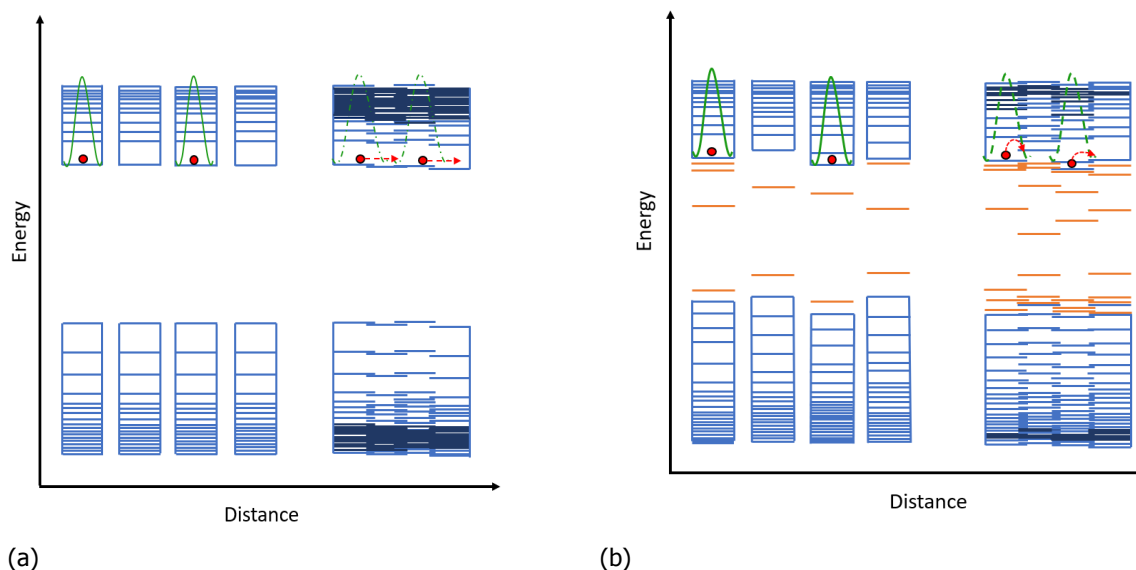
Figure 2.4: a. Energy level splitting in "ideal" QDs. On the left side, discreet energy levels of individual uncoupled QDs with localized, quantum confined electrons. The ride hand side shows their subsequent splitting into energy mini-bands (the darker energy states) accompanied by band like movement of electrons between the QDs with no mid-band trap states. The relaxation in quantum confinement of the electrons due to increased electronic coupling between the QDs is also seen. b. Energy level splitting in "real" QDs. The non-homogeneous QD dispersion in real conditions QDs with varying size (and corresponding bandgap), shape and surface passivation. This results in different density of states in each QDs which gives rise to mid bandgap trap states in uncoupled QDs (left) that further split into more energy levels inside the band gap on coupling (right). Electrons still transport through the hopping mechanism in this case, though there are a few minibands formed at higher CB and VB energies. Adapted from reference [26]

Another parameter that influences charge transport in QDs is the degree of disorder in the structure of QDs packed together in QD solids as shown in Figures 2.4a and 2.4b[26]. In a truly monodisperse collection of QDs where each QD has the same size, shape and surface passivation, these "ideal" QDs arrange themselves in perfect order in QD films analogous to atoms in an atomic semiconductor leading to a homogeneous splitting of energy levels. This gives rise to mini bands like in atomic semiconductors that allow a "band like" carrier transport. However, since even the best experimental procedures synthesize QDs with a 3-5% standard deviation in size, the interaction of such neighbouring "real" QDs in QD solids gives rise to inhomogeneous energy level splitting that prevents the formation of mini-bands and leads to carrier transport by the above mentioned carrier hopping mechanism.

2.3. Charge carrier relaxation dynamics in semiconductors

As mentioned before, carrier relaxation from a high energy state to the band edges contributes the highest towards power loss in solar cells. In atomic semiconductors under thermal equilibrium, charge carriers fill their respective energy bands in a Boltzmann distribution due to their thermal energy [18, 19, 27]
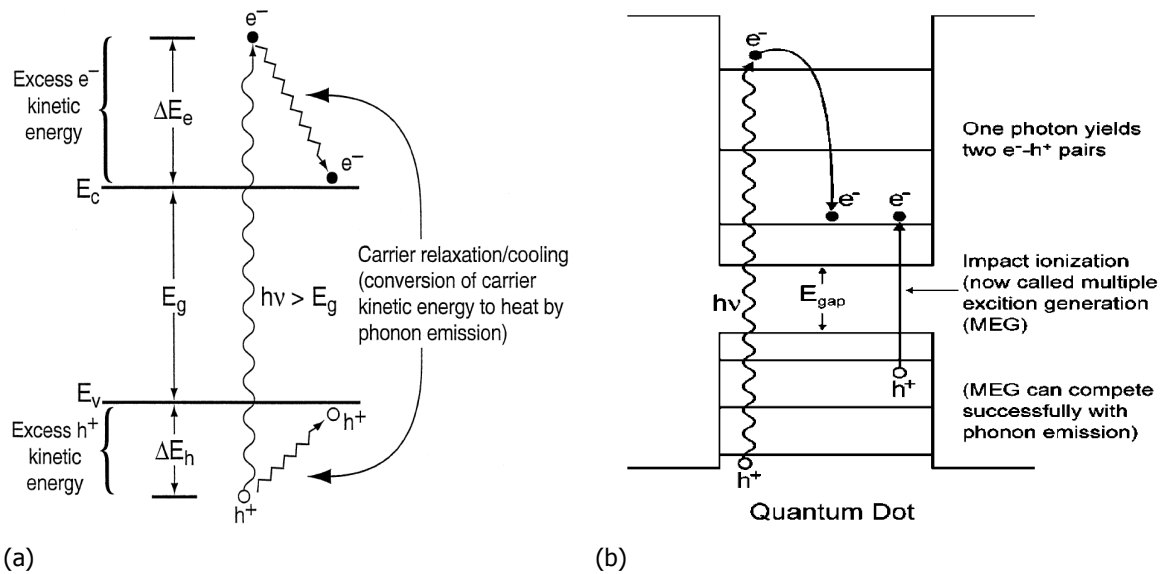
Figure 2.5: a.The thermal relaxation pathway(cooling) of hot carriers in semiconductors. Reprinted from reference [27], copyright Annual Reviews 2001. b. The multiple exciton generation (MEG) pathway expected to be observed in QD semiconductors. Reprinted from reference [16], copyright American Chemical Society 2010.

and an equilibrium exists between the carrier and lattice temperatures. On photoexcitation of such a system, electrons are excited into the CB with varying energies based on the energy possessed by the photon they absorb (given by $h\nu$ where h is the Planck's constant and ν is the frequency of the absorbed photon), leaving behind holes in the VB and causing a perturbation to the Boltzmann distribution and thermal equilibrium. The free charge carriers with excess kinetic energy (ΔE_{excess}=$h\nu$ - E_g) are termed as "hot carriers" since their higher energy makes them "hotter" than the surrounding lattice temperature. To re-achieve thermal equilibrium, these hot electrons cool down by first redistributing themselves to form a new Boltzmann distribution at the elevated temperature followed by a series of quantized lattice interactions known as phonons[18] that raises the lattice temperature until an equilibrium is achieved[27]. Since this two step cooling of charge carriers takes place in the order of a few picoseconds, it becomes difficult to utilize the excess kinetic energy of these hot electrons.

However, it has been observed in the past that this fast hot carrier cooling pathway can be slowed down by 2 orders of magnitude when the photo generated carrier density is greater than 5 x 10^8 cm^{-3}[16, 27] due to the production of an equally high number of phonons that prevents them from readily interacting with the crystal lattice.This allows the possible reabsorption of phonons by the hot carriers that allows them to retain their higher energy for a longer duration. This phenomenon is termed "phonon bottleneck" and can be achieved only under very high light intensities in bulk semiconductors. In quantum confined semiconductors though, it has been theorized that the large energy mismatch between quantized energy steps in the CB (between 150-300 meV) and quantized LO phonon energy levels ($\approx$30meV) could hinder the immediate cooling of hot carriers, thereby, leading to a phonon bottleneck at much lower intensities of light [28].

Interestingly though, experimental data in a few publications have shown only a small increase in hot-electron relaxation times (only by tens of picoseconds) along with the occurrence of photoluminescence which is against the theory of longer hot carrier lifetimes in QDs[16, 28]. This led to the development of the possibility of a second relaxation pathway through Auger recombination. Auger recombination is a non-radiative, three particle process wherein the energy from the recombination of an electron and a hole is transferred to a neighbouring electron/hole. This energy pushes the carrier deeper into the CB/VB which then relaxes to the band edges through phonon transfer to the crystal lattice[16, 18, 19, 26, 27]. In QDs, it was theorized that, cooling of hot carriers would take place by a transfer of energy to a hole *via* the Auger mechanism followed by a fast cooling of the hole (due to a higher effective mass) through phonon emission aided by the closer spaced energy levels for holes in

QDs[27, 28]. The experiments of Klimov *et al.*'s[29] proved the presence of a faster Auger relaxation pathway leading to relaxation of charge carriers in CdSe QDs in the order of 300 fs while Guyot-Sionnest *et al.*[30] showed the electron-hole interaction pathway involved in hot carrier relaxation. The latter also showed the presence of a phonon bottleneck for electrons in the absence of such an electron-hole based Auger recombination by studying the effects of hole isolation *via* surface ligands. Another observation of phonon bottleneck was make by Xu *et al.* [31] who noticed a slowing down of the hole relaxation close to the VB edge due to a possibly low density of VB states close to the edge giving further evidence of a phonon bottleneck in QDS. While the quantization of energy levels in QDs is expected to reduce the electron-phonon coupling due to significant differences between the energy steps of electron and phonon energies, recent studies have shown otherwise. Bozyigit *et al.* quantitatively show the existence of higher energy phonon states that arise due to the mechanical softness of the QD surface where atoms vibrate with higher amplitudes than the core atoms[32]. These results show the existence of a higher electron-phonon couping that provides a quick path for hot electron cooling as opposed to the initial hypothesis of the existence of a phonon bottleneck.

The possibility of an Auger pathway in QD semiconductors also opens doors to the possibility of an inverse Auger pathway as shown in Figure 2.5b wherein the photo excitation by a high energy photon ($h\nu$ at least $> 2E_g$) can cause the high energy electron-hole pair to split into two or more electron-hole pairs of lesser energy. This phenomenon is called multiple exciton generation (MEG) or carrier multiplication (CM) and has been observed in QDs at much lower energies as compared to bulk semiconductors [16, 27, 28, 33]. Known as impact ionization (II) in bulk semiconductors (like bulk silicon), II has been observed to be of significance only at photon energies much into the UV range ($> 3eV$) which contributes to less than 1% of the solar spectrum. This is because the strong coupling of electron and phonon states in bulk semiconductors provides a quicker cooling pathway for hot carriers through phonon emission and the need for crystal momentum conservation in long ordered atomic lattices raises the threshold energy required for CM in such bulk semiconductors. The quantum confinement of charge carriers in QDs however has been expected to help overcome these limitations. Due to the small crystal size and quantum confinement along all three dimensions in QDs, the need for crystal momentum conservation is minimized while the mismatch in the electron and phonon states makes the relaxation of hot carriers *via* phonon emission a rather slow process. Additionally, the high electrostatic forces that bind an exciton also increases the chances for MEG before their separation into charge carriers[33] thereby incentivizing MEG as a viable pathway for hot carriers/excitons.The possibility of utilizing the multiple excitons to produce higher photocurrents than in bulk semiconductors has motivated researchers to use such QD semiconductors in solar cells[15]. However, in addition to the generation of multiple excitons, the effective separation of the exciton into charge carriers and their extraction into electron and hole-accepting contacts is equally important in realizing the true potential of MEG based solar cells[34].

Thus it can be concluded that while a few groups have observed an increase in the cooling times of hot electrons[30] and holes (close to the VB edge)[31] due to a phonon bottleneck, there are also reports where researchers have not observed a similar phonon bottleneck process [29, 32, 35]which gives rise to different theories of hot carrier cooling. The contradicting nature of these theories show the various possible carrier relaxation pathways which could in theory, allow or quench the MEG pathway in QD semiconductors. Thus a more detailed understanding of the electronic behaviour of QDs is required to to successfully incorporate QDs into opto-electronic devices.

2.4. Chemical synthesis and optical properties of PbS QDs

The synthesis of solution processed colloidal quantum dots (CQD) took a big leap forward in 1993 with the first synthesis of nearly monodisperse (<5% rms in diameter) CdE samples (where E = S, Se, Te) by Murray *et al.*[24, 36]. This synthesis method utilized the high reactivity of organo-metallic precursors in a hot coordinating solvent to produce discreet nucleation centres that were then grown into NCs of the requried size by controlling the process paramenters. Dimethyl cadmium (Me$_2$-Cd) was the metal precursor used while the chalcogenide precursor was chosen between trioctylphosphine sulphur (TOP-S) and bis-trimethylsilyl sulphur (TMS$_2$S) with TMS$_2$S's commercial availability and higher reactivity generally being preferred over TOP-S's ease of preparation.
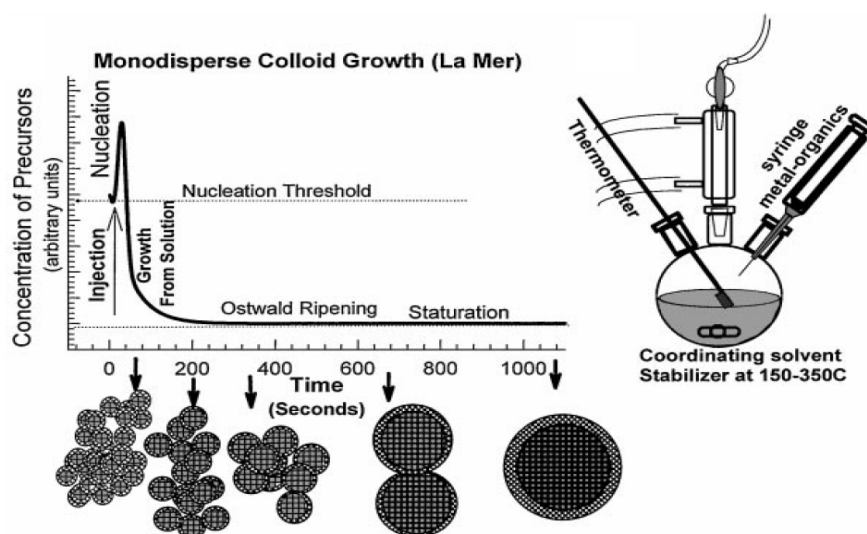
Figure 2.6: The plot on the left shows the different stages of the CQD synthesis process as described by La Mer. The evolution of the particle size with time due to Ostwald ripening is shown below the x axis. The setup on the right side is a typical "hot injection" setup involving the quick injection of the precursor(s) into a hot solvent. Reproduced from reference[36], copyright Annual reviews 2000

The hot injection method adopted in this synthesis follows the reaction steps in line with La Mer's model of nucleation as shown in Figure 2.6. After injection at t=0 seconds, as the precursor concentration in solution increases and exceeds the nucleation threshold of the solution, a burst of nucleation is observed visually. On nucleation, the rate of the precursor consumption begins to increase drastically (to produce more nuclei) and then exceeds the rate of precursor addition at the inflection point in the nucleation zone. Due to a higher consumption rate, the precursor concentration continues to drop and falls below the threshold at which point nucleation stops. After this point, the reaction products are utilized in the uniform growth of all the nuclei in a regime known as the size focussing regime. During this time, all the nuclei grow at the same rate giving rise to a nearly monodisperse solution of nano particles provided there is no further addition of reactants. Since all these changes occur within seconds, it is essential that the injection of the precursor(s) is very quick if not the nucleation step and the size focussing regime overlap, leading to a polydisperse sample. Once all the reactants are utilized and the concentration approaches zero, the size focussing regime ends. However, the high surface energy of small NCs push them to dissolve into the solution and precipitate on the larger NCs leading to a second temperature and time dependant growth regime also known as Ostwald's ripening[25, 36]. Figure 2.6 shows the effect of time on the particle size due to the ripening.

In 2003 Hines *et al.* adopted a similar approach to synthesize lead sulphide (PbS) NCs with high levels of monodispersity using lead oleate and TMS_2S[37]. The lead oleate was prepared by heating lead oxide (PbO) in a coordinating solvent of oleic acid at 150°C followed by the hot injection of TMS_2S at different temperatures to obtain NCs of the requried size. The samples from this synthesis showed a narrow size dispersion as evidenced by a full width at half maximum (FWHM) measurement of ≈100meV and a photo luminescence quantum yield (PLQY) of 20% relative to a standard IR125 dye. The lead oleate ligands passivate the QD surface and help in dispersing the QDs in a nonpolar solvent. Following this, Cademartiri *et al.* adopted a new diffusion controlled route to synthesize PbS NCs[38]. In this method, lead chloride ($PbCl_2$) is mixed with oleylamine (OLA) which complexes on heating at elevated temperatures (> 120°C) to form a viscous solution. The viscosity of the solution controls the diffusion of the injected precursor (elemental sulphur dissolved in OLA, S:OLA) through the solution by reducing the mass transfer coefficient of the reaction. This forces the reaction to follow a diffusion controlled path that enhances the size focusing nature of the reaction. As a result, higher magnitudes of monodispersity (≈52meV at FWHM) and a higher PLQY of 40% (referenced to an IR-125 dye) was observed. In addition to lead oleate passivation, the presence of chloride ions (Cl^-) on the surface was

also observed through XPS and EDAX measurements. One disadvantage of the Cademartiri synthesis is that it produces larger PbS QDs with diameters in between 4.2 and 6.4 nm (corresponding to first exciton absorption peaks of 1200 nm and 1600 nm respectively[39]) compared to the Hines synthesis (diameter range of 2.6nm - 7.2 nm) that has prompted modification by other research groups. Moreels *et al.*. used tri-n-octylphosphine sulphur (TOP-S),a low-reactivity sulphur precursor, along with S:OLA to prolong the QD growth regime without the onset of Ostwald ripening[40] which resulted in a wider size range (3-10 nm) and higher monodispersity at larger sizes. Weidman *et al.*[41] discovered that using excess lead precursor (upto a Pb:S precursor ratio of 24:1) in the Cademartiri synthesis could delay the onset of Ostwald's ripening by upto 6 hours leading to highly monodisperse ($\sigma_d \approx$ 3-5%) PbS CQD solutions between diameters 4.3 nm and 8.4 nm. Zhang *et al.*[42] modified this hot injection synthesis into a "heat up" synthesis by injecting more reactive TMS_2S at 30°C instead of the hot injection of lesser reactive S:OLA. This was observed to increase the nucleation threshold of the reaction which gave more size focussed QDs with sizes small as 2.2 nm (bang gap of 1.7 eV) and a size distribution comparable to that of the hot injection method. An important advantage of the Cademartiri synthesis (and all subsequent modifications) is the in-situ chloride passivation of the QD surface (in addition to lead oleate passivation) that reduces the trap state density, increases PLQY and the air stability as seen in all three modifications[38, 40–42].

Cation exchange reactions have been employed in the past to prepare core-shell QD configurations of PbSe-CdSe[43] that presents an interesting pathway to achieve NCs of different compositions and configurations otherwise difficult to be achieved by traditional synthesis methods. In such reactions, the parent NC provides a template wherein the cation in the QD lattice is exchanged for a similar charged cation in a balance between the solvation energy of the exchanged cation and the lattice binding energy before and after the exchange. Zhang *et al.* developed a cation exchange process to synthesize PbS(Se, Te) QDs from pre-synthesized CdS(Se, Te) QDs that involves the use of lead chloride and OLA [44]. As expected, the resultant PbS(Se, Te) QD size was controlled by the starting size of the CdS(Se, Te) QDs used in the synthesis and residual chlorine and cadmium were measured on the QD surface and deduced to be surface passivators. Hendricks *et al.* developed a different approach to PbS QD synthesis by utilizing the variation in the reaction kinetics of different substituted thioureas with lead oleate to give PbS QDs of different sizes[45]. In this thesis, the cation exchange approach has been predominantly adopted to fabricate solar cells with a few measurements also performed on PbS from Hendricks *et al.*'s approach.

2.5. Quantum dot solar cells

A better understanding of the physics of QDs and the development of efficient methods of QD synthesis led to their implementation in light harvesting devices (solar cells) and light emitting devices (LASERs, LEDs). Their solution-based syntheses has opened up cheap avenues of scaling up to the industrial level, required to compete with current electronic technologies. PbS has emerged as the most promising candidate for QDSCs amongst different QD materials due to its large light absorption coefficients, large Bohr radius and wide band gap tunability[46]. PbS QDSCs have predominantly been fabricated in 3 different configurations and this section shall look into the development of such solar cells.

Sensitized solar cells were first fabricated using a porous n-type cathode material sensitized by QD particles resulting in a band alignment as shown in Figure 2.7. Titanium dioxide (TiO_2) was commonly used as the cathode material sensitized by PbS QD particles. Hoyer *et al.* discovered photoconduction in a heterogenous system consisting of a porous TiO_2 thin film filled with PbS QD particles [48] showing a bandgap of $\approx$1.85 eV. It was observed that with only the chosen bandgap (or higher) that the band alignment enabled effective carrier extraction from the QDs. Adding to this work, Ju *et al.* developed PV cells showing a PCE of 3% by adding indium doped tin oxide (ITO) and gold to the above configuration[49]. A decrease in PCE with larger TiO_2 NCs was observed as opposed to an expected increase due to possibly higher carrier extraction from the increased contact area between the PbS and TiO_2. This helped conclude the that the mesoporous structure is unfavourable for QDSCs. Thus, QDSCs development moved towards planar configurations beginning with the Schottky junction.

A Schottky junction QDSC utilizes the work function difference between the ITO and a back-metal
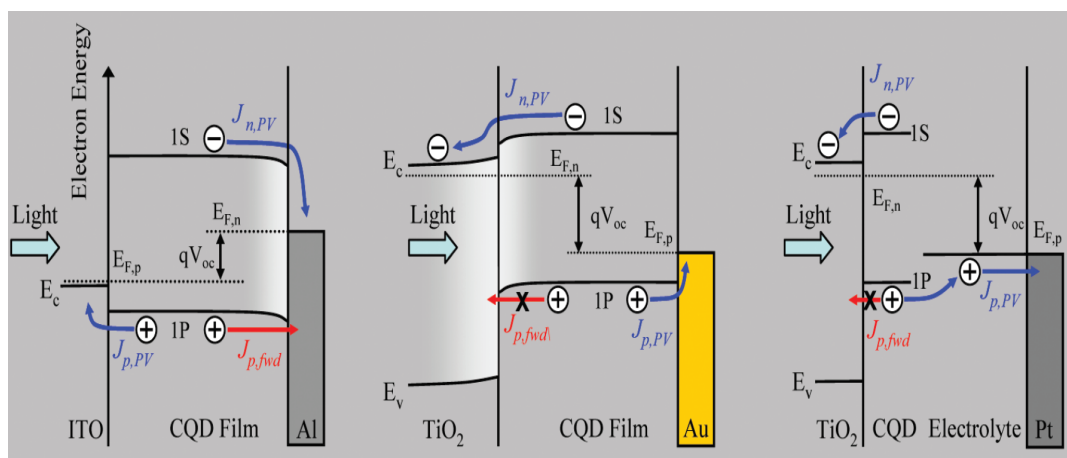
Figure 2.7: A compilation of the band diagrams of the three common PbS QDSC configurations.The left most configuration depicts a Schottky junction solar cell where the charge carrier separation and extraction occurs at the rear junction between the PbS QD layer and the metal electrode. The middle configuration shows a depleted heterojunction solar cell in which the TiO_2 nanoparticles-PbS QD layer interface forms the main junction where charge extraction and separation takes place. The right most configuration shows a TiO_2 sensitized QDSC in which the differences in electron affinity between the TiO_2 and the PbS QD layer causes charge separation. Reprinted from reference [47], copyright American Chemical Society 2010.

contact to generate a photovoltage that splits the excitons and extracts charges through the p-type CQD layer as seen in Figure 2.7. Prior work[50, 51] has showed that the Schottky junction is at the QD/metal contact interface resulting in charge separation at the rear boundary. This poses a challenge as if increases the possibility of recombination of photogenerated charge carriers formed farther away from the junction by the absorption of shorter wavelength photons unless the PbS layer is made thinner than its diffusion length. One advantage of the Schottky junction configuration is its ability to produce current densities over 20mA/cm^2 that has been exploited to make devices with P.C.E $\approx$2% [50]. However, the maximum open circuit voltage (V_{oc}) of these solar cells is limited to half the bandgap of the PbS QDs ($E_g/2q$). This is because, the coincidence of the VB, CB and fermi level of the metallic contact limits the splitting of quasi fermi levels in the absorber side to half the bandgap, failing which the polarity of the contacts inverts. To overcome the limitations posed by Schottky junction cells, planar n-p junction solar cells were developed which utilise a transparent n-type electrode to extract the photoelectrons from the PbS absorber layer and form a heterojunction. Over the years, several changes have been made to the processing steps leading to efficiencies as high as 12%.

One of the most important processing steps involved in QD film formation for devices is the exchange of long insulating ligands with shorter ligands to improve carrier transport. However, ligands have also been observed to dope QDs by inducing a dipole moment on the QD surface. Brown et $al.$ compared the effects of 12 different ligands on the energy levels of PbS QDs and concluded that the intrinsic dipole moment of different ligands shifts the energy levels of the QD by different magnitudes as shown in Figure 2.8a[52]. In addition, the interaction of ligands with the QD surface introduce new energy levels near the CB or VB that act as donor or acceptor states respectively. Consequently, the different ligands influence the Fermi level position differently and hence dope the QDs differently. Density functional theory (DFT) calculations showed that the lack of an intrinsic dipole moment in iodide ligands lead to deeper energy level shifts while thiols with higher intrinsic dipole moments, induced a shallower energy level shift. This has formed the basis for band alignment engineering leading to high efficiency PV cells[54].

QD films have also been doped using remote doping techniques which do not interfere with the QD surface chemistry (as observed with the ligands), size or affect interdot spacing. In this process, solid QD films are immersed in a dopant solution of specific concentration for a specific duration to achieve the required doping. Based on their electron affinity and ionization energies, dopant solutions act as p- or n-type dopants as shown in Figure 2.8b. Kirmani et $al.$ showed that dopants with a deep electron affinity could induce a remote flow of electrons from the VBM of the QD into the LUMO of the dopant due to their close alignment leaving behind a p-doped QD [53]. In addition, higher dopant

(a)   (b)
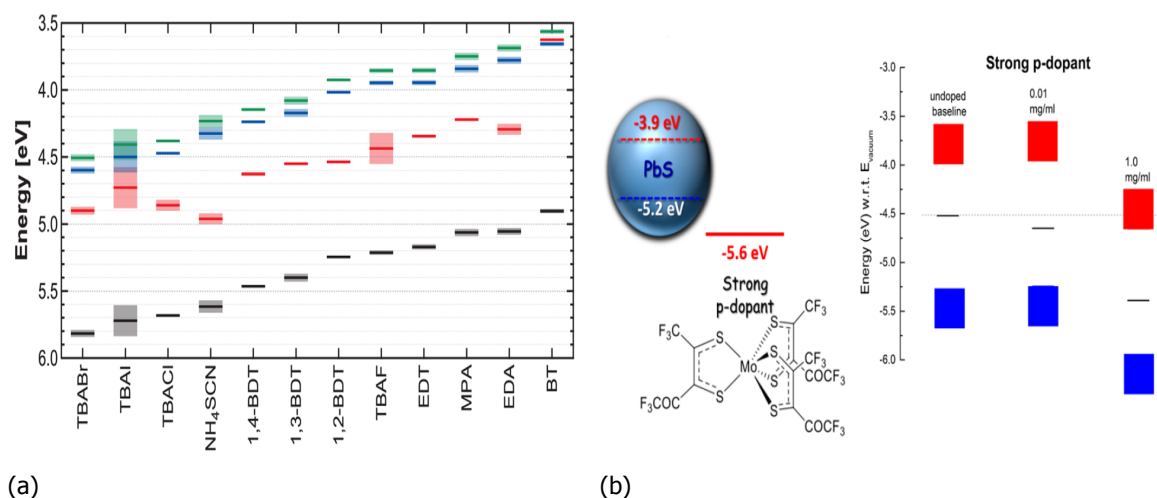
Figure 2.8: a. A change in almost 1eV between butane thiol(BT) and tetrabutylammonium bromide (TBABr) treatments on PbS QDs is observed. In addition, the position of the Fermi levels relative to the valence band is also seen to change with different ligand treatments that proves their doping. Reprinted from reference [52], copyright American Chemical Society 2014. b. The position of the LUMO of the p-dopant induces electron flow into the dopant, leaving behind a hole rich p-doped QD. The energy level diagram on the right side shows the effect of different dopant concentrations on the energy levels of the QD. While lower concentrations push the Fermi level alone, higher concentrations move the CB and VB due to the interface dipole moment induced by the dopant. Reprinted from reference [53], copyright American Chemical Society 2016.

concentrations were also shown to induce a surface dipole moment due to the increased diffusion into the QDs that push the energy levels of the QD similar to that seen in Brown *et al.*'s work.

In 2010, Abraham *et al.*[47] developed a planar depleted heterojunction configuration that incorporated the high short circuit currents (J_{sc}) of Schottky junction solar cells and the high V_{oc} of sensitized cells. These devices were the first to break the 5% P.C.E mark and hence formed the base for future research. The heterojunction is formed between a wide bandgap n-doped electrode like zinc oxide (ZnO) or TiO$_2$ which acts as an electron accepting and hole blocking layer and the light absorbing QD layer. The holes are collected at the back contact using a deep workfunction metal like gold (Au) while the electrons are collected at the top contact which is typically a transparent conductive oxide (TCO) like ITO or fluorine doped tin oxide (FTO). As mentioned in Section 2.2, since real QDs have bandgap states due to incomplete passivation of the QD surface, the diffusion length of minority carriers in the QD films, defined as the average distance travelled by a minority charge carrier before it recombines with a majority carrier, is very small. This leads to significant difficulty in extracting minority charge carriers formed on photo excitation in such planar devices. To tackle this problem, these devices are made to work as drift driven devices where the minority carrier transport is predominantly dependent on an electric field formed by the space charge region (depletion width) at the heterojunction. The QD absorber layer thickness in such a case is limited to the sum of the depletion width and diffusion length which ensures that the charge carrier formed farthest away from the heterojunction can diffuse until it reaches the space charge region and then be transported to the other side of the junction by the electric field. In the following years, this depleted heterojunction has undergone several modifications leading to solar cell P.C.E exceeding 10% [17, 55–61]. The following paragraphs will detail the development of high efficiency heterojunction QDSCs.

In the beginning of depleted heterojunction QDSC development, 1,2-ethanedithiol (EDT) and 3-mercaptopropionic acid (MPA) were commonly used due to their ability to p-dope the absorber layer and their short lengths that allow better electronic coupling between neighbouring QDs in films . While EDT was predominantly used to make such devices, Jeong *et al.* [62] showed that MPA ligand exchanged PbS QD films performed much better than EDT ligand exchanged films due to its ability to better passivate the QD surface and pack QDs closer than with EDT ligands leading to higher carrier mobilities. However, in 2014, Chuang *et al.* [54] developed a novel approach that involved engineering the band alignment of the PbS QDs based on its interaction with 2 different ligands as observed by
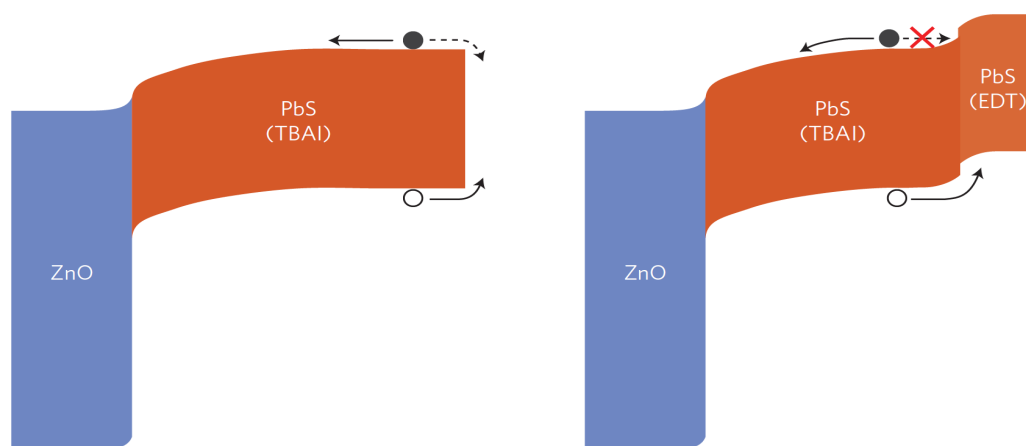
Figure 2.9: A comparison between the normal PbS heterojunction QDSC and "band alignment engineered" PbS heterojunction QDSC. The addition of EDT capped p doped PbS layers with the iodide capped n doped PbS layers causes additional band bending in the rear side thereby enhancing carrier extraction and blocking electrons from collecting in the rear electrode. Reprinted from reference[54], copyright Macmillan Publishers Limited 2014.

Brown *et al.* [52]. The PbS QDSCs fabricated with this method showed a P.C.E of 8.55% that thereafter became the norm in depleted heterojunction QDSCs. In this approach, each deposited layer of the oleate-capped PbS QD films was ligand exchanged with tetrabutyl ammonium iodide (TBAI) except the final two layers that were instead ligand exchanged with EDT. As seen in Figure 2.9, the deep energy levels of iodide capped PbS QD films from TBAI treatment and the shallow energy levels of the EDT capped PbS QD films align such that electrons flow from the EDT capped layers to the iodine capped layers resulting in favourable band bending that forms an electron blocking layer to prevent electron collection at the metal contact. Using the same configuration, other research groups have obtained similar results using other ligand combinations with similar functionalities like lead iodide (PbI_2) and MPA[63]. Following this, researchers have achieved high efficiency QDSCs by attempting to improve different aspects of the solar cell fabrication procedure.

The primary area of improvement that researchers have focused on has been the improvement of the diffusion length of minority carriers in PbS QDs. During the synthesis of PbS QDs, the bulky oleate ligands that bind to the QD surface form a ligand shell around the QD and prevent the subsequent diffusion of other oleate ligands to passivate trap states. While solid state ligand exchange techniques have been shown to effectively displace the oleate ligands attached to the as-prepared QD surface, it does not help in improving the overall passivation of the QD surface. As a result, solution phase passivation techniques were adopted as a post synthesis treatment to improve the surface passivation of the as-prepared QD solutions. It was observed that this process replaced a few of the oleate ligands, while retaining enough to maintain the stability of the QDs in the non-polar solvent (usually octane). This increased the binding of passivating ligands in solution resulting in more completely passivated QDs in solution. Halides with their small size have shown very good passivating capabilities and have been extensively used in solution phase passivation. A few of the solution phase ligands used and tested with QDSCs were cadmium chloride - $CdCl_2$ (provided Cd^{+2} and halide passivation of the S^{2-} and Pb^{+2} vacancies)[64], TBAI[65, 66], molecular iodine (I_2)[55], methyl ammonium iodide (MAI, a milder I source)[56] and Trimethylsilyl chloride (TMS-Cl in n-hexylamine and n-octylamine)[14]. The TMS-Cl passivated QDs have been shown to allow partial fusing of neighbouring QDs that led to superior passivation qualities (due to a decrease in surface area-to-volume ratio of the quantum dot along with improved passivation) giving a diffusion length of $\approx$ 230nm. Of these techniques, MAI treatment produced QDSCs with the highest P.C.E of 10.6% due to its ability to controllably strip oleate ligands and subsequently passivate them well with I^-. The QDSC devices made with I^- ligand passivation were found to be the most air stable amongst the halides due to the ideal size of iodide ligands that ensured optimum steric hindrance for maximum passivation and maximum screening of the QD atoms from the atmospheric O_2.

While all the above devices involved developing the QD absorber layer-by-layer (LbL) deposition methods followed by solid state ligand exchange, a single step solution phase ligand exchange reaction was explored to reduce the total device fabrication time. One of the major hurdles in a such a single step solution phase ligand exchange was finding the best solvent that could maintain stability of the QDs capped with shorter ligands in solution and have a low boiling point for good film formation. Sargent and co-workers developed a strategy as seen in Figure 2.10a that involved a solution phase exchange of the oleate ligands from the PbS QDs in octane with iodide ligands present in a polar solvent like N,N-dimethylformamide (DMF)[67]. Due to the immiscibility of DMF and octane, the solution phase ligand exchange was triggered by vortexing after which the I^- capped QDs automatically re-dispersed in the DMF. The immiscibility of the two solvents allowed easy separation of the two phases formed and the I^- capped QDs were then washed and dispersed in n-butylamine with a very high concentration ($\approx$200mg/mL). This CQD ink was then deposited in a single step (as opposed to LbL deposition) to obtain QD films of the required thickness and uniformity. While MAI, sodium iodide (NaI)[67] and PbI_2[68] have been used as iodine sources, a mixture of PbI_2/ lead bromide ($PbBr_2$)/ammonium acetate (NH_4Ac)[60, 61] showed the best results leading to PbS QDSCs with P.C.Es of 11.28% [60]and 11.6% [61].

In addition to new passivation techniques to improve the diffusion length in PbS QD films, researchers have also worked on increasing the width of the depletion region in the absorber layer to improve drift based carrier transport. The width of the depletion region in the PbS absorber layer (w) is given by:

$$w = \frac{2N_D \epsilon_1 \epsilon_2 (\Psi_{bi} - V)}{q N_A (\epsilon_1 N_D + \epsilon_2 N_A)} \tag{2.3}$$

where N_D and N_A represent the density of free electrons and holes in the n region and p region respectively, ϵ_1 and ϵ_2 are the permitivities of the n and p regions respectively, Ψ_{bi} represents the built-in potential of the junction, while V represents any applied bias[69]. The above equation shows that increasing the N_D concentration can increase "w" which has been exploited by researchers. In PbS QDSCs with a bilayer configuration[54], the existence of 2 junctions, the n+/n heterojunction between ZnO (or TiO_2) and the n/p quantum junction between I^- capped and EDT capped PbS (also called the hole transport layer, HTL) makes it interesting to optimize the device architecture. Techniques like substitutional doping of the ZnO layer by incorporating indium into the ZnO lattice in solgel based ZnO[58], the chloride passivation of oxygen vacancies in ZnO NC films by treating the film with sodium chloride (NaCl)[61] and the soaking of ZnO NC films in ultra violet (UV) light to release gaseous molecules possibly adsorbed onto the ZnO NC surface [70] have demonstrated that increasing the n doping in the n+ layer has indeed resulted in an improved performance of PbS QDSCs. Analogously, increased p doping of the HTL *via* molecular doping[71] and sodium hydrosulphide (NaHS) treatment[72] has also shown to increase the depletion width in the absorber layer in addition to improving band bending at the interface during the maximum power point (MPP) condition leading to high fill factors (F.F.) and high P.C.E solar cells. Introducing extra electron transport layers (ETLs)[73, 74] and HTLs[73, 75–77] at these interfaces have also been reported to improve device performance.

Despite the high performance of heterojunction solar cell, there are some inherent disadvantages associated with such a configuration. The misalignment of bands at the junction could potentially lead to a loss in open circuit voltage and improper charge injection into the n-type window layer for QD films with a smaller bandgap[78]. Thus, the ideal QDSC configuration would be to have a specific bandgap tuned PbS QD film with p and n doping on opposite side of the p-n junction that has the entire p-n junction absorbing light to produce photo generated carriers. Such quantum junction solar cells (QJSCs) have also been developed with p doping being achieved though physical deposition of the oleate capped PbS layer in air followed by tetramethylammonium hydroxide (TMAOH) treatment and air annealing and n doping through iodide treatment inside a N_2 filled glovebox[55, 78]. Further modifications through the addition of an n+ layer in between the iodide treated film and the metal contact[49] and replacing the iodide ligand exchanged n layer with an n-type CQD ink as discussed earlier has resulted in performance enhancement leading to P.C.E as high as 8% [66].

While most of the high efficiency QDSC configurations have utilized a deep work function metal like gold (Au) as the rear metal contact, Gao *et al.'s* [79] work has shown the formation of a Schotkky barrier
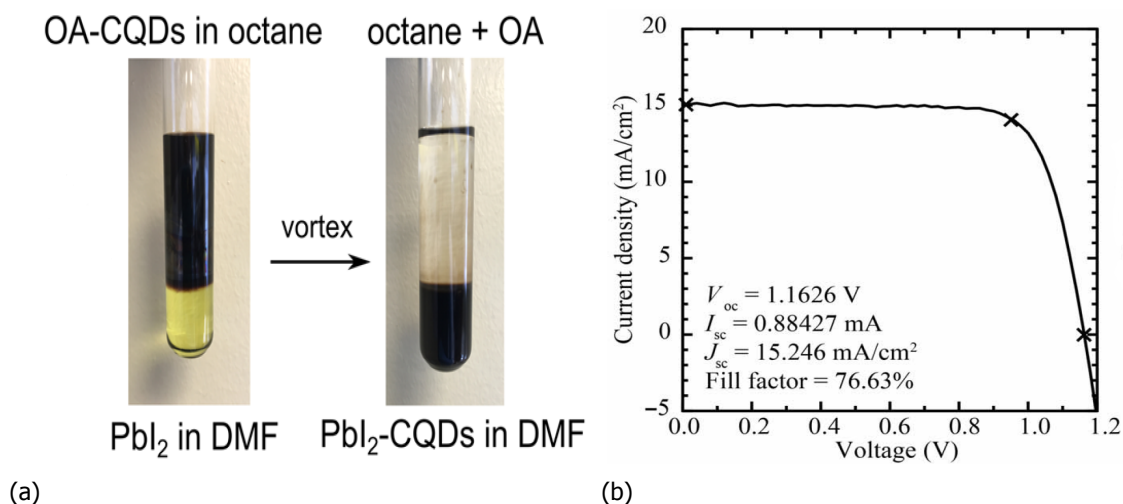
Figure 2.10: a. The steps involved in a complete solution phase ligand exchange resulting in a CQD ink. The immiscibility of octane and DMF has been exploited to completely exchange the long oleate ligands of as prepared PbS QDs with shorter PbI_2 ligands and then separate the octane from the iodide capped PbS in DMF[68], copyright AIP publishing. b. The J-V curve of the current world record QDSC [17], copyright American Association for the Advancement of Science 2017.

for holes at the rear PbS/metal leading to current saturation at higher forward applied voltages. This motivated the use of different combinations of rear metal contacts to induce a favourable band bending for both electrons and holes. While for this purpose, some research groups use a hole selective layer like molybdenum oxide(MoO_x)[80], others use a combination of step wise decreasing work function metals (Au/Ag or MoOx/Au/Ag or AZO/Ag where AZO is aluminum doped zinc oxide and Ag is silver) or simply just Au. While different configurations seemed to have worked for different devices, a systematic study of any possible performance enhancement of this interface using all possible configurations has not yet been studied. In recent years, perovskite based QDs have also been fabricated based on cesium lead iodide ($CsPbI_3$). The performance curve of one such device structure developed at the National Renewable Energy Laboratories (NREL) currently which holds the world record P.C.E of 13.23%[17] is shown in Figure 2.10b. Other world record devices include devices developed by Choi *et al.* with a P.C.E of 11.6% [61] based on a CQD ink and Lu *et al.* with a P.C.E of 11.21% based [59] on solid state ligand exchange.

2.6. Electrochemical doping of porous films

In general, intrinsic semiconductors have their Fermi level located in the middle of the E_g due to an equal density of electrons and holes. In bulk semiconductors, doping is achieved by the addition of impurity atoms into the crystal lattice of the semiconductor which increases the density of one of the charge carriers in the system. This shifts the Fermi level of the system towards either the conduction or the valence band, based on whichever charge carrier density is increased. However, attempts to dope semiconductor NCs using similar doping methods have failed in the past primarily because any charged impurity that is incorporated into the QD lattice, instead of being charge compensated by a free charge carrier, is compensated by ligands that attach to the QD surface[81]. While this challenge has led to the development of several innovative ways of doping QD films like photo doping, remote doping and the action of ligands, all these methods involve uncontrolled doping procedures. Electrochemical gating on the other hand has emerged as an efficient controllable method of doping QD films. This it does by feeding carriers into the films by applying a voltage across the film in an electrochemical setup as shown in Figure 2.11.

On application of a negative potential across the working electrode (W.E) and the reference electrode (R.E), the Fermi level of W.E (and the QD film) is forcibly pushed up (with respect to the vacuum level) until it moves into the C.B of the QD film at which point, electrons begin to flow into the QD film. While this creates a net negative charge in the QD film, counter ions permeate into the porous QD film from the electrolyte solution to help maintain charge balance. This method has been used to introduce upto
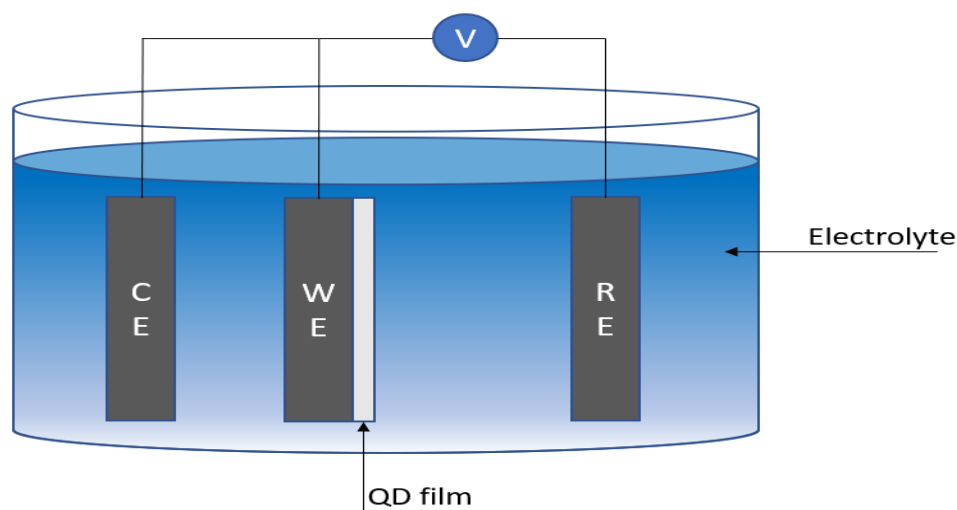
Figure 2.11: A schematic of the electrochemistry setup. Due to direct contact between the working electrode (W.E) and the QD film, their Fermi levels align which is then controlled by application of a voltage across the reference electrode (R.E) and the W.E during electrochemical gating to inject (expunge) electrons into(out of) the C.B. (V.B.). The counter electrode (C.E) acts as a source/sink of electrons that maintains charge neutrality in the electrolyte solution.

$\approx$10 electrons per QD in a reversible way into the QD film[22]. However, the charge stability of such electrochemically doped films has been a matter of concern in the past. Voltage scans have showed that the initial potential after doping decays to the V_{oc} on removing it from the electrochemistry setup, denoting a loss of the injected charges in the system. While it has been conjectured that the movement of counter ions from the QD film back into the electrolyte solution has been the main reason for the lack of charge stability, recently, Gudjonsdottir *et al.*[82] developed a way to freeze the ions inside the QD film which has resulted in good charge stability of the doped QD films. This was achieved by using a high melting point solvent (PEG 6000) and a small sized cation like Li^+ or Na^+. It was also observed that similar results were not obtained with larger sized cations showing that these results were possibly due to the intercalation of the cation into the QDs. Another approach to dope QD films is through charge transfer doping as seen in the work of Hu *et al.*[83]. In this work, doping was performed by introducing an organic salt in the QD film that dissociates into its respective ions in the QD film. On dissociation, the cation (anion) was reduced (oxidized) by accepting (donating) electrons from (to) the QD films thereby leaving behind a p (n)-doped QD film. In this method the organic salt was chosen in such a way that one of its ions forms a stable radical on accepting or donating an electron (depending on which type of doping it induces) while the other ion helps in charge compensation to maintain a neutral system. While the effectiveness of these doping approaches in solar cell devices haven't been realized yet, they have paved the way to interesting pathways to dope QD films electrochemically. A different type of electrochemical doping was attempted as a part of this thesis which shall be discussed in Section 4.3.

3

Experimental Setup

3.1. ZnO NC synthesis

ZnO NCs were synthesized using a recipe similar to that used in other works by our colleagues[82] which was adopted by modifying recipes followed by Wood *et al.*[84] and Mashford *et al.*[85]. 750 mg of Zinc acetate dihydrate ($Zn(OAc)_2.2H_2O$) was dissolved in 50 mL of anhydrous ethanol in a conical flask placed in a water bath heated to 60°C under continuous stirring. Simultaneously 351 mg of potassium hydroxide (KOH) was dissolved in 5 mL of anhydrous methanol by placing the mixture in an ultra-sonication bath. On complete dissolution of the reagents, the KOH-methanol mixture was added dropwise into the conical flask. The reaction was then allowed to continue for 2 minutes following which the conical flask was allowed to cool back to room temperature. The reaction products were transferred to 40 mL vials and an antisolvent (hexane) was added followed by a solvent (ethanol) until the mixture turned cloudy, denoting precipitation. The QDs were then collected by centrifuging the turbid solution at 2000 rpm for 1 minute and the supernatant was decanted. Finally, the QDs were dispersed in 7.5 mL of ethanol, filtered through a PTFE 45 μm filter and stored in a 20 mL vial inside the freezer at -20°C to maintain the size distribution of the NCs. On prolonged exposure to atmospheric temperatures, the ZnO QD solution turns turbid due to possible fusion of the closely spaced NCs that lack any surface ligands . Best results were obtained with anhydrous solvents. Figures 3.1a and 3.1b show the first exciton absorption of ZnO NC solution in ethanol, the absorption onset in annealed ZnO films and the trap state luminescence of ZnO NCs under long wavelength UV light.

3.2. Solgel synthesis

3.2.1. ZnO solgel

ZnO solgel is prepared using the method followed by Ohyama *et al.*[86]. 1.2 g of Zinc acetate dihydrate was dissolved in 12 mL of 2-methoxyethanol and 0.31 mL of ethanolamine by heating the mixture at 60°C under constant stirring. For atomic doping, different amounts of indium chloride ($InCl_3$) was added to dope the solgel solution with indium between 1 and 5 at.%.

3.2.2. TiO$_2$ solgel

TiO_2 solgel was prepared using the method followed by Crisp *et al.*[63]. 125 μL of DI water and 2 drops of 30% hydrochloric acid were added to 5 mL of anhydrous ethanol in a 20 mL vial. Following this, 375 μL of titanium ethoxide was added dropwise into the reaction mixture under constant stirring. Care has to be taken to avoid any precipitate formation during the dropwise addition. The headspace of the vial is filled with nitrogen and the mixture is allowed to stir for 2 hours. The vial is then stored in a freezer at -20°C and is taken out when required.

3.3. PbS QD synthesis

3.3.1. Cation exchange

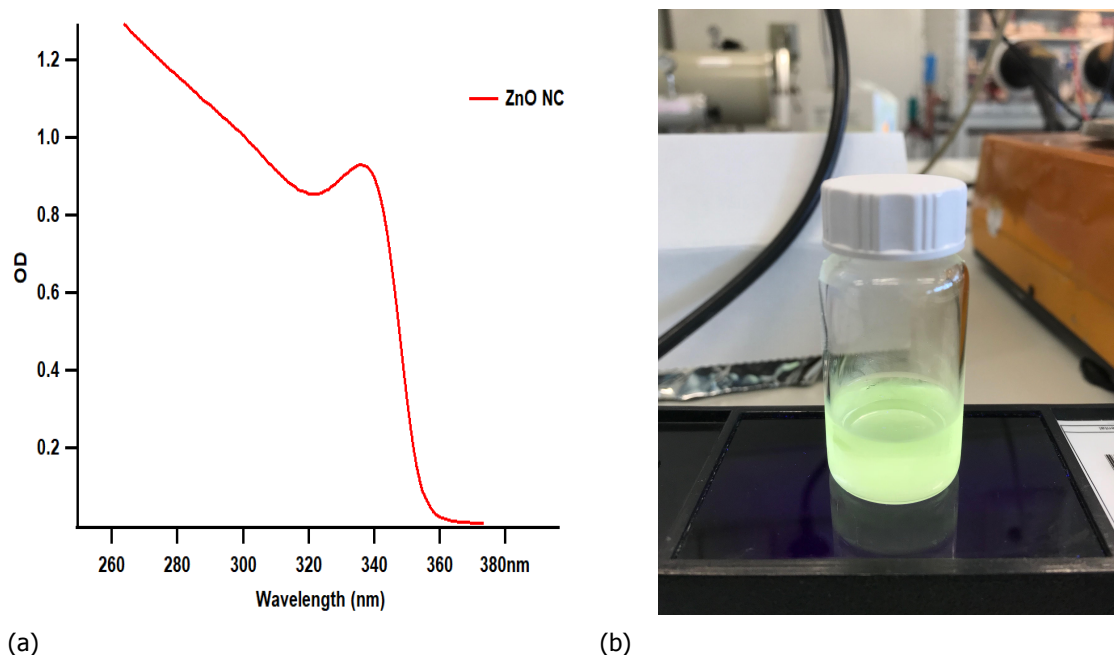(a)   (b)

Figure 3.1: a. Absorbance spectrum of ZnO NC solution in ethanol showing a first exciton absorption peak at 337 nm. b. PL of ZnO QDs in ethanol under long wavelength UV light due to trap states.

CdS QD preparation

A slightly modified version of the method followed by Chernomordik *et al.* was adopted for the cadmium sulphide (CdS) synthesis[87]. 0.66 g of cadmium oxide (CdO), 4 g of degassed, technical grade oleic acid (OA) and 18 g of technical grade 1-Octadecene (ODE) were measured and transferred to a 100 mL round bottom three-neck flask. The mixture was stirred continuously and degassed at 110°C to remove moisture after which the reaction vessel was purged with nitrogen to provide an inert atmosphere in the reaction vessel. The temperature was then increased to 260°C and the reaction let to continue until the burgundy colour of the mixture disappeared leaving behind a colourless solution that denotes the reaction of the constituents to form cadmium oleate as seen in Figure 3.2a. After complete colour change, the heating mantle was removed and the reaction mixture was cooled to a temperature of 32°C. In the meantime, the sulphide precursor was prepared by mixing 850 μL of ammonium sulphide ($(NH_4)_2S$) (48% in H_2O) with 15 ml of degassed oleylamine (OLA) in a 20 mL vial with a partially open lid. This is to allow the outgassing of the vigorous exothermic reaction of the components which form a yellow gel-like mixture. The gel was continuously stirred until a clear yellow mixture of $(NH_4)_2S$ and OLA was obtained. The sulphide precursor was injected into the cadmium oleate at 32°C and the reaction was allowed to continue for an hour under constant stirring. After 1 hour, the flask was removed from the Schlenk line and its contents transferred into two 40 mL vials. The CdS QDs were precipitated by adding a solvent (hexane) and an antisolvent (ethanol) until the clear yellow solution turned turbid following which it was centrifuged at 4000 rpm for 5 minutes to collect the precipitated QDs. The clear supernatant was decanted, the QDs were mixed in 9 mL of toluene, filtered through a PTFE 0.45μm filter and finally stocked in a 20 ml vial. This washing protocol is essential to remove the unwanted by-products of the synthesis that are left behind in the solution. The above procedure repeatably yields CdS QDs with a first exciton absorption peak at ≈362 nm as shown in Figure 3.2b as opposed to 366 nm as reported by Chernomordik *et al.*[87] and Zhang *et al.*[88].

PbS QD preparation

Cation exchanged PbS was prepared using Zhang *et al.*'s[44] method. 400mg of lead chloride ($PbCl_2$) was added to 10 mL of OLA in a round bottom three-neck flask. The mixture was stirred continuously and degassed at a temperature of 100°C to remove any moisture and undesirable short amines. Following degassing, the Schlenk line was purged with nitrogen (N_2) and the reaction temperature increased to 140°C. As the temperature nears 140°C, the solution changes in clarity from cloudy to clear denoting the formation of a complex. The reaction was allowed to carry on for 10 minutes at
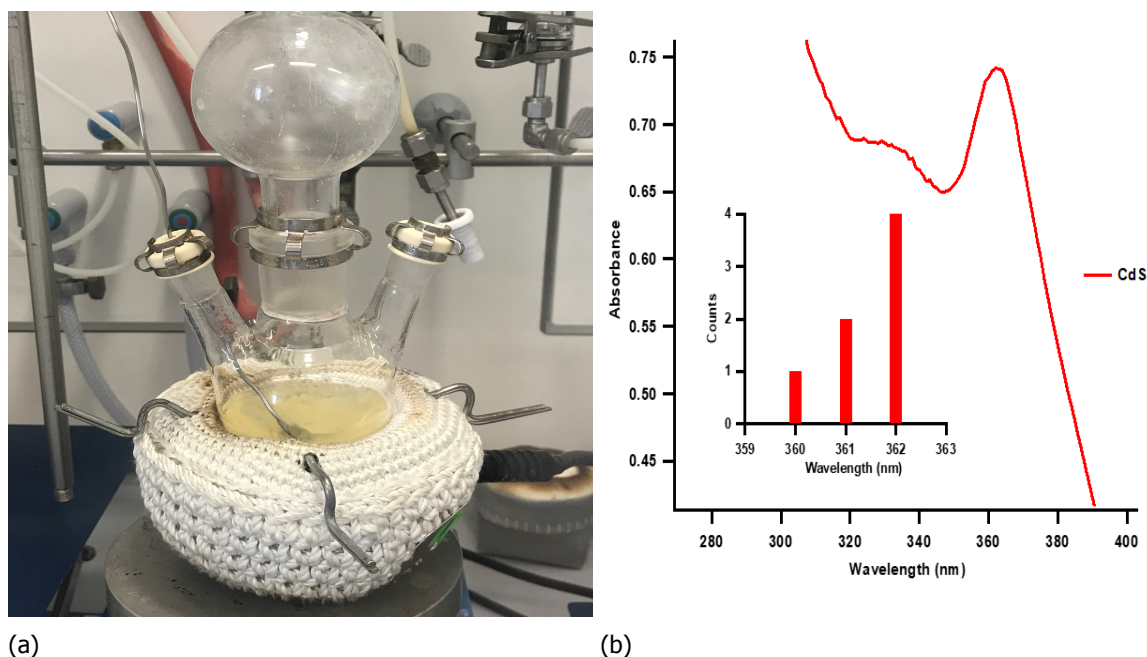
(a)   (b)

Figure 3.2: a. The conversion of burgundy coloured CdO and oleic acid to colourless Cd(oleate)$_2$ in ODE on prolonged heating at 260°C. b. Absorption plot of CdS QDs showing a sharp peak at ≈ 362 nm denoting a highly mono disperse QD solution in toluene. In the inset, a histogram of 7 such CdS syntheses that repeatably yielded QDs with a first exciton absorption peak at ≈ 362 nm.

140°C during which time the cloudiness returned. This is possibly due to the polymerization of the lead-OLA complex. Meanwhile, 2.5 mL of the above prepared CdS QD solution (≈100 mg/mL), 10mL of anhydrous hexane and 5 mL of degassed oleic acid were kept aside in separate syringes with needles unexposed to air. After 10 minutes at 140 °C, the temperature was brought down to 90°C and CdS was swiftly injected through one of the necks of the flask. This resulted in an almost immediate change in colour of the solution from yellow to dark brown. The heating mantle was then removed and replaced by a water bath to quench the hot reaction vessel. At around 70°C, the hexane was injected into the reaction flask followed by OA at 35°C. The oleic acid provides oleate ligands that replace the weakly bound OLA ligands on the surface and aids in the stability of the PbS QDs in a non-polar solution. Figures 3.3a-3.3d capture important steps of the reaction as described above. On addition of OA, the reaction temperature increased to around 45°C which was then cooled down to room temperature. The final product was transferred into a N$_2$ flushed 40 mL vial and the washing protocol was then followed as mentioned in the CdS synthesis using ethanol as the antisolvent. However, due to the air sensitivity of these QDs, care has to be taken to not expose the QD solution (or washed solution) to air at any point. The washing step was repeated once with an antisolvent and once more without an antisolvent to remove the insoluble chlorides in the solution. Finally, the QDs were dispersed in octane with a concentration of 20 mg/mL.

3.3.2. Substituted thiourea based synthesis

PbS NCs were also prepared by the method adopted by Hendricks *et al.*[45]. The substituted thiourea used in this synthesis was N-phenyl-N'-3,5-bis(trifluoromethyl)phenyl thiourea. 1.86g (20 mmol) of phenylamine (aniline) in toluene was added to 5.42 g (20 mmol) of 3,5-bis(trifluoromethyl)phenyl isocynate in toluene and allowed to stir for a few minutes following which the volatiles were removed on the Schlenk line using vacuum. This was done until all the toluene was removed and a solid white mass of the substituted thiourea was left behind. Lead oleate was prepared using lead oxide, trifluoroacetic acid and trifluoroacetic anhydride. 230 mg of lead oleate was then mixed with 10mL of hexadecane in a 25mL three neck round bottom flask inside the glovebox. The substituted thiourea was heated to 60°C in a hotplate and 2 mL of it was taken in a syringe. The three-neck round bottom flask was attached to the Schlenk line and degassed at 100°C. Once base pressure was reached, the temperature was reduced to 90°C and the substituted thiourea was injected. The reaction mixture
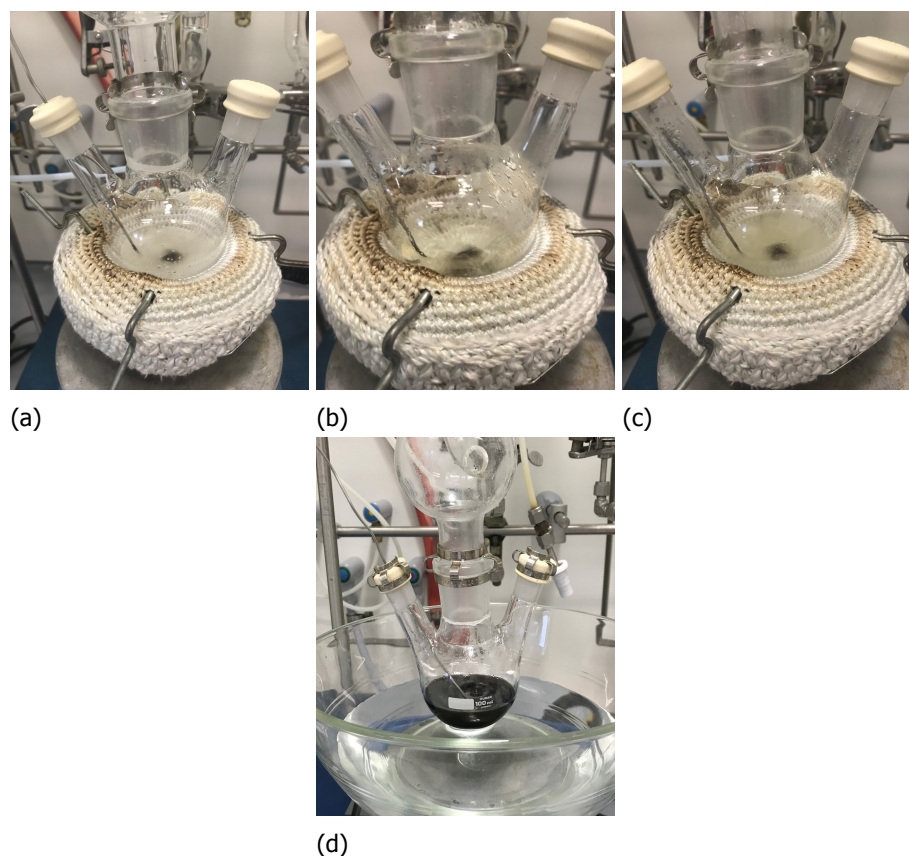
(a)   (b)   (c)

(d)

Figure 3.3: The various stages of the PbS cation exchange reaction in order. a. Cloudy mixture of PbCl$_2$ in OLA under constant stirring. b. Clearing up of the cloudiness in the solution due to a complex formation between PbCl$_2$ and OLA. c. Return of the cloudiness on prolonged heating of the reaction mixture at 140°C due to the polymerization of PbCl$_2$/OLA complexes. d. Final black coloured PbS solution upon cation exchange and subsequent quenching.

changed colour in a few seconds and the reaction temperature was maintained at 90°C for 2 minutes following which it was cooled down to room temperature. The final product was transferred to a N$_2$ sparged 40 mL vial and the QDs were washed by adding a solvent (hexane), antisolvents (ethanol and methanol) and centrifuging at 4000 rpm. The ethanol has to be added first followed by methanol failing which the hexadecane and methanol form an immiscible mixture. The QDs were washed once more and then dispersed in octane with a concentration of 20 mg/mL.

3.4. Device fabrication

Devices were made with (25.4 x 25.4 x 0.7) mm ITO/glass (180 nm ITO thickness, R$_{sheet}$=7-10 Ωcm^2, MTI) as well as (24 x 24 x 2.2) mm FTO/glass (200 nm FTO thickness, R$_{sheet}$ = 30 Ωcm^2, Hartford Glass Co.) substrates. The procedure adopted by Crisp et. al.[63] was followed. Figure 3.4a shows the configuration of the PV devices fabricated and Figure 3.4b shows the finished device.

The ITO substrates were wiped vigorously with ethanol followed by ultra-sonication in hexane, acetone and ethanol respectively. The clean substrates were UV ozone treated for 30 minutes before the start of device fabrication. FTO substrates were prepared in a similar fashion except that they were wiped vigorously with Triton-X solution in DI water followed by ultra-sonication in acetone and ethanol. FTO substrates were mainly used for devices with TiO$_2$ as the n-type window layer since ITO is not thermally stable at the annealing temperatures of 450°C required for TiO$_2$. The following steps were followed during device fabrication:

1. The n-type window layer was spin coated followed by an annealing step in a hot plate in ambient conditions. 130 μL of the solution was pipetted on the ITO/ FTO substrate such that it covered the entire surface of the substrate followed by spin coating at different process conditions based

(a)   (b)
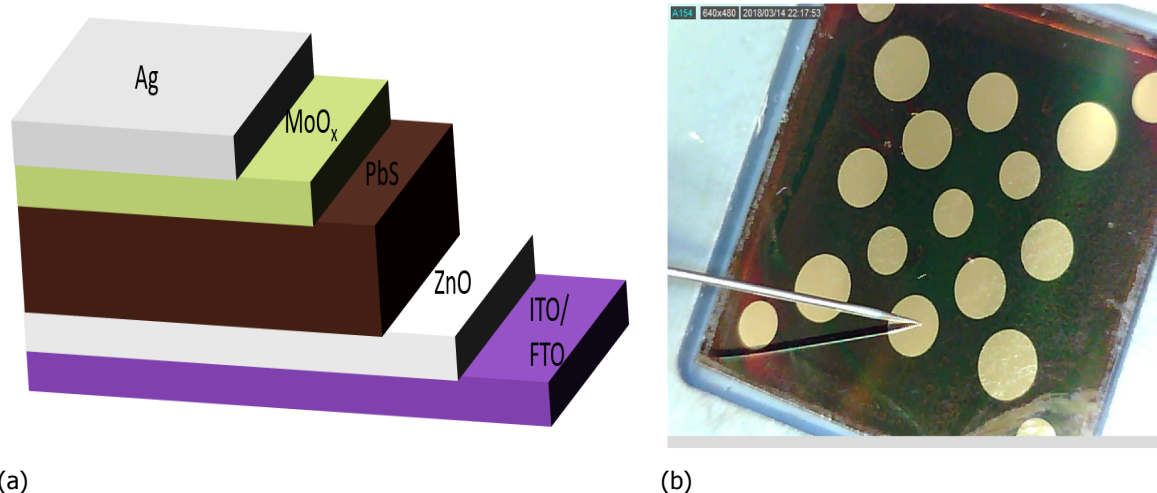
Figure 3.4: a. Structure of the devices fabricated. A superstrate structure was adopted with the TCO (ITO/ FTO) forming the front contact and the silver forming the reflective back contact. b. Each of the 17 pixels in this fabricated device is a working solar cell albeit the bottom right most pixel. This pixel is evaporated directly on the TCO to reduce contact resistance.

on the material used:

    (a) ZnO NC solution was spin coated at 2000 rpm (best result) for 30 seconds and annealed at 260 °C for 30 minutes.

    (b) ZnO solgel solution was spin coated at 3000 rpm for 30 seconds and annealed at 200°C for 10 minutes.

    (c) TiO_2 solgel solution was spin coated at 1400 rpm (best result) for 30 seconds and annealed at 450 °C for 30 minutes. A drying step was followed for TiO_2 in between spin coating and annealing by heating the substrate for 20 minutes at 115 °C.

2. The PbS absorber layer was prepared by layer by layer (LbL) deposition through spin coating or dip coating followed by a solid-state ligand exchange to replace the long chain insulating ligand (oleate ligand) with a shorter and conductive ligand. The layer by layer approach ensures that the volume contraction that occurs during solid state ligand exchange is not high enough for film delamination and that ligand exchange takes place throughout the entire thickness of the film. Though both techniques were used, spin coating was found to produce the most uniform films and was the technique used to make the devices discussed henceforth in the thesis.

    (a) The 20 mg/mL PbS solution in octane was used for spin coating. 90 μL of solution was pipetted on the substrate such that it covered the entire substrate and then spin coated at 1400rpm for 45 seconds with a ramp rate of 3 seconds (500rps). Spin coating with the above parameters yielded a layer of $\approx$ 40 nm thickness (Appendix, Figures A.1a-A.1c).

    (b) The spin coated film was dipped in the ligand exchange solution for a stipulated duration to ensure complete ligand exchange:

        i. PbI_2 ligand exchange: Each spin coated layer was dipped for 2 minutes in a 10 mM solution of PbI_2 (99% trace metal basis, Sigma Aldrich) in DMF.

        ii. MPA ligand exchange: Each spin coated layer was dipped for 15 seconds in 10% vol solution of MPA in methanol.

    (c) After ligand exchange, the substrate was rinsed in clean acetonitrile (ACN) to remove the excess DMF/methanol that doesn't dry quickly. It is to be noted that DMF and methanol are miscible in ACN and PbI_2 ia not appreciably soluble in ACN. Failure to perform this step produced white patches on the substrate due to the precipitation of the displaced oleate ligands that don't get washed away completely. These white patches form ohmic contacts that result in shunted devices.

    (d) In the event of film delamination, the following corrective approaches were followed:

    i. The thickness of each spin coated layer was reduced either by increasing the rotation speed during spin coating or by reducing the concentration or both. A reduction in concentration was preferred due to its linear relation to the film thickness. This reduces the total volume contraction in the film that helps the film to remain anchored to the substrate.

    ii. If ZnO was used as the n-type window layer, the ZnO coated (and annealed) substrates were soaked in a 10%vol solution of MPA in methanol for 30 minutes. The carboxylic acid group in MPA is expected to attach itself to the dangling bonds in the ZnO layer thereby allowing the thiol group to anchor the PbS QDs onto the substrate which potentially can reduce delamination.

(e) The spin coating and subsequent solid-state ligand exchange was performed until the required thickness was achieved. In general, the final two layers of spin coated PbS were ligand exchanged with MPA to form a bi-layer as engineered by Chuang et.al.[54]. All spin coating steps are performed in a controlled N_2 environment inside the glovebox unless specified.

3. The back contact was deposited by thermal evaporation with a shadow mask as shown in Figure A.1d to control the shape of the contacts. 57 nm of Molybdenum trioxide (MoO_3) (99.97 % trace metal basis, Sigma Aldrich) was deposited as a selective hole contact prior to 260 nm of silver (Ag) (99.99% Kurt J. Lesker company) that acts as the reflective back contact. All depositions were performed in an oxygen deficient environment with a pressure between 3 x 10^{-7} and 4 x 10^{-6} mbar. Due to this reason, the MoO_3 deposited is not of exact stoichiometry and hence shall be referred to as molybdenum oxide (MoO_x). Cheung et. al.[89] has however determined the MoO_x deposited by a similar method to be $MoO_{2.6}$. Figures A.2a, A.2b show the profilometry scans of the MoO_x and Ag layers.

4

Results and discussion

4.1. QD solar cell development

The first part of the thesis involved developing a recipe for PbS QDSC fabrication that yielded reproducible results. While our champion device produced a PCE of 4.7% under standard AM1.5 spectrum produced by a Xe lamp and 7.5% under an LED producing an intensity of 1000 W/cm^2, several trends were observed during the development stage and are reported as discussed below.

4.1.1. Effect of synthesis type

The primary method used for PbS synthesis is the cation exchange method as discussed in section 3.3.1. However, in order to measure the effectiveness of this method, we also adopted the substituted thiourea based synthesis (as discussed in section 3.3.2) developed by Hendricks *et al.* [45] and compared the optical properties and performance of devices made using PbS from both synthesis. Figure 4.1a shows the normalized absorption and photolumicescence (PL) curves of PbS from both synthesis. 2.5 μL and 10 μL of PbS solution in octane was diluted in 125 μL of anhydrous octane and 1mL of anhydrous toluene for the absorbance and PL measurements respectively. The cation exchange produces a first absorption peak between 865 nm and 900 nm and a PL peak at $\approx$1010 nm while the thiourea based synthesis produces a peak at 924 nm with a red shifted PL peak at 1050 nm. The size of the PbS QDs made by the cation exchange synthesis ($\approx$ 2.7 nm) largely depends on the initial size of the CdS QDs made prior to exchange leading to a larger bandgap of 1.43 eV compared to the thiourea based synthesis that produced slightly larger QDs, 3 nm in diameter with exciton peaks at 924 nm (corresponding bandgap of 1.34 eV).

Despite producing QDs with the ideal bandgap, a comparison of the PLQY of the PbS from the substituted thiourea based synthesis throws light on an important property of the QDs: surface passivation. A higher surface passivation leads to lesser surface trap state density which quenches the trap state recombination pathway of excited carriers and produces a higher PLQY. The PbS made by cation exchange produces a PLQY of 50% as compared to the 35% of the PbS made from the substitured thiourea denoting better surface passivation of the cation exchange method. This can be attributed to the use of PbCl$_2$ in the cation exchange leading to *in situ* halide passivation unlike the other synthesis method that has no halide precursor. As a result of the improved surface passivation, devices fabricated using the PbS synthesized using the cation exchange perform better than the other synthesis method. Figure 4.1b compares the performance of solar cell devices made using PbS from both synthesis methods through current density vs. voltage curves (J-V curve).

While the dark curves do not differ by much, both the V$_{oc}$ and the J$_{sc}$ of both the curves are very different. This can be explained by the fact that the higher surface passivation of the cation exchange synthesis leads to a better collection of photo generated charge carriers that is reflected in a higher short circuit current. Due to the very similar behaviour of the dark curves of devices made using PbS from both the synthesis methods (Appendix, Figure A.5), it can be approximated that the ideality factors and the saturation current for both devices are comparable to each other. The V$_{oc}$s of both

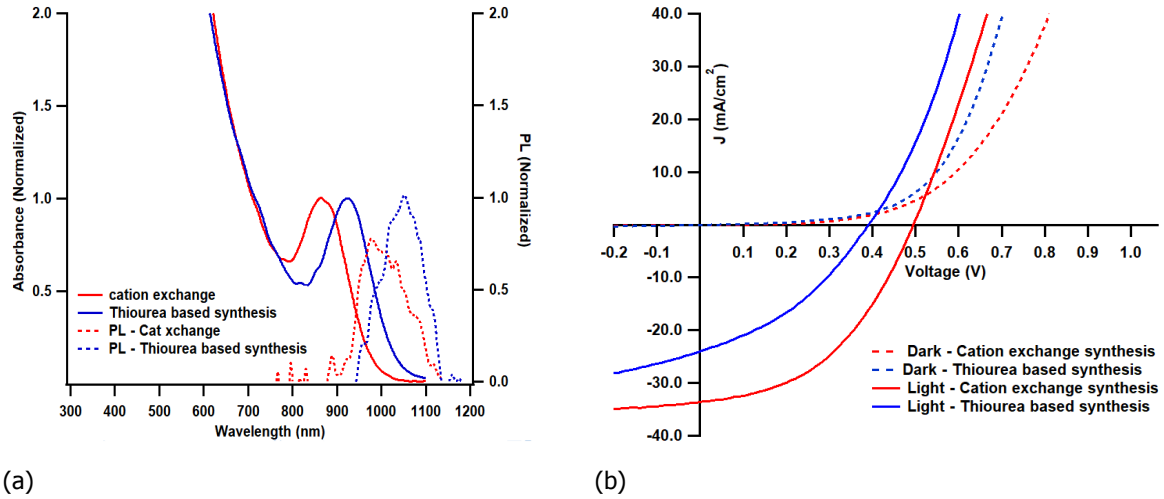(a)   (b)

Figure 4.1: a. A comparison of the absorption and photo luminescence (PL) sepctra of PbS synthesized using different synthesis methods. The PL spectra are red shifted by ≈160 nm and give PL quantum yields (PLQY) of 50% and 35% for the cation exchange and thiourea based synthesis respectively which denotes better passivated QDs in the cation exchange synthesis method. b. The J-V curves of the PbS QDSC devices made using cation exchange and substituted thiourea based synthesis methods are presented here. For this experiment, the J-V curves were measured using an LED lamp that produces light with an intensity equal to 1 sun and spectrum as shown in Figure A.4. As expected, the higher passivation of the QDs made using cation exchange give it a higher V_{OC} and J_{SC} when compared to the thiourea based synthesis.

devices were compared by fitting the above data into equation 4.1 [90] :

$$V_{OC} = nkT/q(ln(J_{SC}/J_o)) \tag{4.1}$$

where, J_o is the saturation current, kT is the product of the Boltzmann constant and temperature, n is the ideality factor and q is the elemental charge. Due to comparable 'n' and J_o values for both the devices, the higher J_SC in the cation exchanged devices lead to a higher V_{OC}. However, since the V_{OC} scales with only the natural logarithm of the J_{SC}, it does not completely reflect the 0.1 V decrease in V_{OC} of the substituted thiourea based devices. While the reason for this is still unclear, it could be that the trap states are close to the band edges which reduces the effective bandgap of the PbS.

To study the optical properties of the absorber layer, spectrometric measurements were performed on the PbS films with different capping ligands. Figure 4.2a shows the normalized absorption curves of PbS QD films with different capping ligands. Compared to the PbS CQD solution, all the PbS QD films show a red shift of ≈30 nm and a broadening of the absorption peak irrespective of the nature of the capping ligand. This can be explained by the increased electronic coupling of the QDs in a film and the subsequent inhomogenous broadening. While reading the J-V curves, two important observations can be made. The first one is that in all J-V curves, the dark and light curves intersect at a finite voltage (as seen in Figures 4.1b, 4.2b) which is uncharacteristic of ideal solar cells. Ideal solar cells follow the following modified diode equation[18, 19]:

$$J = J_0(exp((V/(nkT)) - 1)) - J_{ph} \tag{4.2}$$

where I is the diode current density at voltage V, J_L is the current density due to photo generated carriers, J_0 is the saturation current density, n is the diode ideality factor and kT is the product of the Boltzmann constant and temperature. In the dark, the absence of any photogenerated charge carriers makes the value of I_{ph} zero which amounts to a simple diode equation. However, under light, the photogenerated charge carriers give a finite value to I_{ph} thereby shifting the curve downwards by a finite quantity without any change in its shape in which case there is no intersection of the dark curve with the light curve. However, any change in the basic diode equation under light can change the shape of the light curve leading to an intersection of the two curves. This can be explained by looking deeper into the diode equation. The saturation current density (J_0) is given by the equation[18, 19]:

$$J_0 = qn_i^2\left(\frac{D_N}{N_A L_N} + \frac{D_P}{N_D L_P}\right) \tag{4.3}$$

where D_N and D_P are the diffusion constants of electrons and holes respectively, L_N and L_P are the electron and hole minority carrier diffusion lengths respectively and N_A and N_D are the acceptor and donor doping concentrations. The ZnO film used in the device stack as described in Section 3.4 has been shown in the past to change its doping profile under UV illumination [70] due to the release of trapped gas molecules. Since the standard AM 1.5 spectrum used in the solar simulator contains light in the UV range as well, it is possible that the doping profile in the ZnO changes on illumination leading to a change in the saturation current density. In addition to this, the low doping concentrations of PbS QD films ($\approx 10^{15}$-10^{16} cm^{-3} from literature [91]) possibly leads to a high injection regime where the photogenerated density of charge carriers is comparable or higher than the doping densities. Since the above equation for saturation current density is valid only for low injection regimes, it is possible that the switch to a high injection regime under illumination leads to a change in the shape of the J-V curve under light causing it to intersect with the dark curve (also referred to as "crossover effect"). The second phenomenon prevalent in these QDSCs is current hysteresis. Figure 4.2b shows a difference in the J-V characteristics of solar cells between a forward and reverse voltage sweep. This is understood to be a result of possible movement of ions or charges during the voltage sweep. Since doping of QDs is not atomic in nature but due to variations in net charges present in a film, the voltage scans may induce movement of charges/ions through the different layers of the QDSC stack. In addition, the difference in conductivities of the various layers in the QDSC stack may also lead to the stagnation of these charges in one end (instead of flowing through the external circuit) during a voltage sweep cycle in one direction which then flow through the external circuit during the reverse sweep leading to different performances[46].

Summing up, the cation exchange synthesis led to well passivated QDs capable of being used for fabricating solar cell devices with PCE upto 5% while the substituted thiourea method, though did not lead to good devices, can be optimized to be used to synthesize PbS over a wide range of bandgaps. Additionally QDSC devices has been observed to show a "crossover effect" due to the low doping densities of PbS which leads a high-injection regime during illumination and current-hysteresis due to movement of ions or accumulation of charges at one end.

(a)   (b)
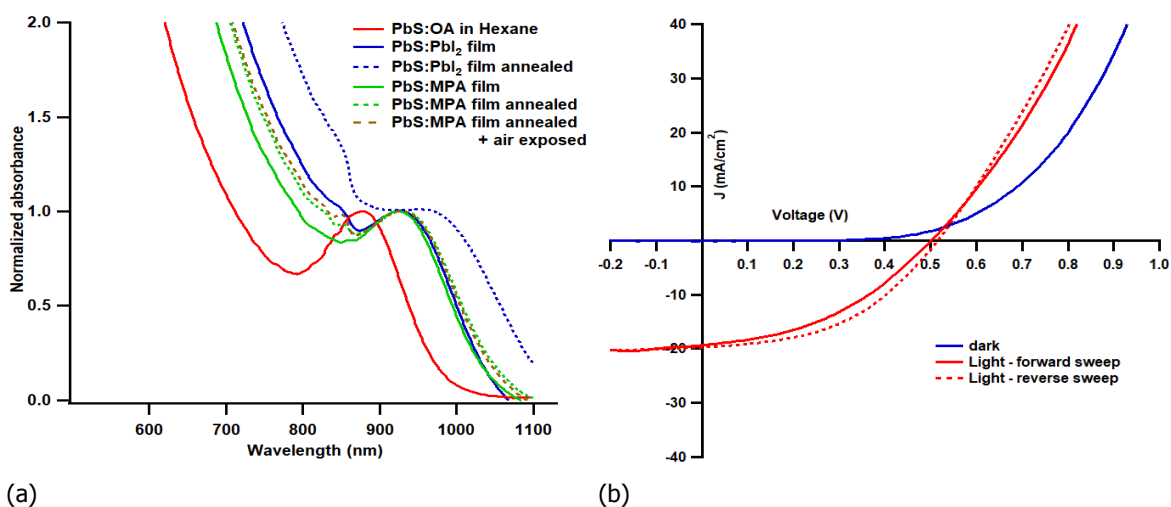
Figure 4.2: a. Comparison of absorption spectra of PbS QD films with different capping ligands. 80 nm thick as-prepared PbS films were made on quartz slides followed by solid state ligand exchange and annealing (if mentioned) between 90 and 115°C. b. Devices are observed to perform differently under a forward (from -1V to +1V) and reverse voltage sweep (from +1V to -1V) with better performance under the reverse voltage sweep (dashed J-V curve).

4.1.2. Effect of humidity and oxygen

During the start of the development of PbS QDSCs for this thesis, the CQD solution was synthesized using normal air exposed solvents and the QDSC stack was fabricated under ambient conditions (as mentioned in literature[63]) with the only exception that relative humidity (RH) levels were as high as 60%. This led to a lot of devices that were either shunted (Appendix, Figures A.7a, A.7b, A.7c) or had delaminated layers due to the interaction of atmospheric moisture with the PbS. Figure 4.3a

compares the J-V performance of devices made under low atmospheric RH (25%) and high RH (50%). It is evident that under high RH, the device loses its rectifying behaviour in the dark though there is a small amount of photo voltaic behaviour under illumination. This could be partially explained by the observations of Tang *et al.*[92] who showed that the exposure of small PbS QDs ($\leq$ 3 nm diameter, $\geq$ 1.3eV bandgap) to atmospheric oxygen produces lead sulphite and sulphate molecules on the QD surface that introduce surface trap states. In addition, Garcia *et al.*[93] recently showed that when the ambient RH levels are high, the $PbSO_x$ impurities arising from the hydrolysis of the sulphur in the QD surface and ligand species of the HTL reshape the quasi-spherical QDs into hexagonal micro crystals and introduce voids in the stack. These voids were found to not only cause QD films to delaminate, but also introduce pinholes that act as shunts in devices. Based on the depth of these voids, the performance of the devices could be affected which is in good agreement with the results observed during the entire duration of this thesis. Another possible reason for the shunted behaviour is that the interaction of moisture with the QDs push the energy levels of the PbS QDs such that the Fermi levels of the metal oxide layer and the PbS align with each other even before equilibrium. In such a scenario, no space-charge region is formed at the interface between the two materials resulting in ohmic behavior of the device.

(a)

(b)

(c)
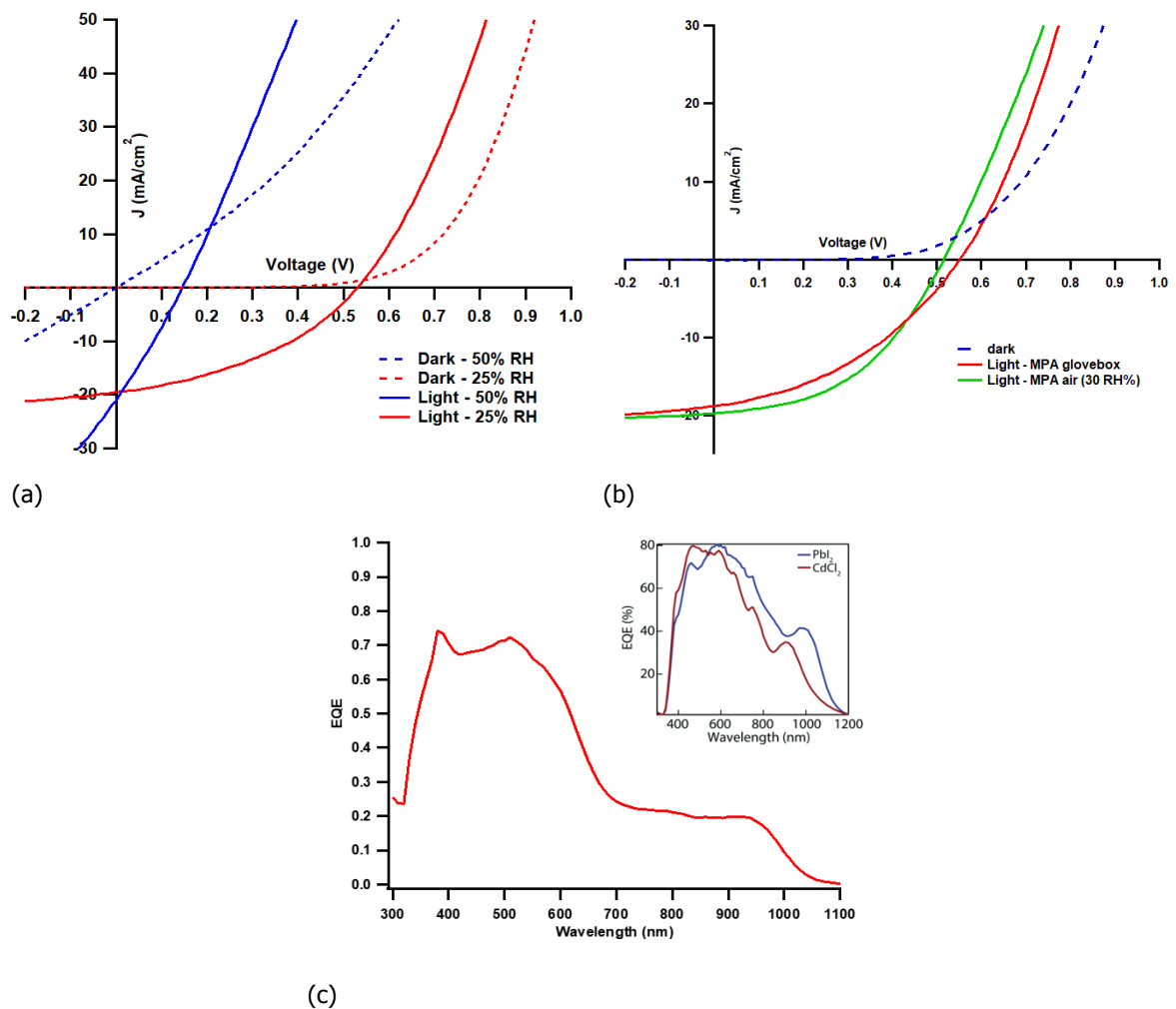
Figure 4.3: a. A comparison of the J-V curves of devices fabricated under ambient conditions with different relative humidity (RH). Higher RH tends to reduce the rectifying behaviour of the devices in the dark and light due to possible impact on the doping levels of the PbS QDs. b. Air exposure (30% RH) of the MPA capped layers of the QD films has been observed to improve device performance. These devices were prepared through LbL deposition by spin coating and ligand exchanging. PbI_2 ligand exchanging was performed inside a N_2 filled glovebox while MPA exchange was performed inside or outside the glovebox (as specified). c. EQE spectrum of the champion device (P.C.E - 4.72%, measured using a solar simulator) showed in Figure 4.3b. A lack of the first exciton peak at $\approx$ 900 nm denotes a possible photo oxidation of the QDs. The insert shows the EQE curve of a device fabricated with similar processing conditions as found in literature[63].

However, the concept of p doping the QD films by air exposure has been used to improve the F.F. and produce more efficient PbS QDSCs. The detrimental effects of moisture exposure of QDs were negated by conducting the synthesis in a moisture free environment using anhydrous solvents, and spin casting and ligand exchanging the various individual layers inside a N_2 filled glovebox. Due to the adoption of a band alignment engineered configuration as described in Section 3.4, these devices possess 2 different p-n junctions- a heterojunction at the ZnO/PbS(PbI$_2$ capped) interface and a homojunction at the PbS(PbI$_2$ capped)/PbS(MPA capped) interface. While most consider the heterojunction to be of significance in controlling the device performance, experiments by Rekemeyer *et al.* [94] show that the homojunction indeed is of higher significance and that holes are the minority carriers in these QD films that determine the solar cell performance under illumination. Since the MPA capped layer (also referred to as a HTL) is comparable in thickness to the diffusion length of minority carrier in PbS QD layers ($\approx$70-100 nm) unlike the PbI$_2$ capped layer(160 nm), increasing the p doping in the top-most HTL could improve band bending at the interface and also increase the depletion width in the bulk of the PbI$_2$ capped PbS absorber layer (as per equation 2.3) while ensuring that the HTL remains depleted throughout. While this leads to improved photo generated carrier collection and a higher J_{SC}, V_{OC} and F.F, introduction of trap states while p doping the top layers could suppress the small increase in V_{OC} and instead, cause it to slightly decrease as seen in Figure 4.3b. Table 4.1 compiles the effect of air exposure of the top QD layers on the FF and P.C.E. Figure 4.3c shows the external quantum efficiency (EQE) curve of the champion device (P.C.E - 4.72%). Compared to literature [63], the curve is blue shifted due to possible photo-oxidation while measuring the J-V response under ambient conditions prior to EQE measurements. Photo oxidation is known to form a thick PbO layer around the PbS QDs and the higher bandgap of the PbO could have influenced the blue shift of the entire spectrum. The absence of an exciton peak at $\approx$900 nm denotes a loss of quantum confinement in the QDs and the reason for such an observation is still quite unclear. Figure A.6 shows the performance of a device made using the same procedure as above but using an iodide ligand precursors that has been used in literature.

From the above discussion we could conclude that the presence of moisture during the PbS synthesis and device fabrication possibly led to an unfavourable band alignment that led to shunted behaviour while air exposure of the top-MPA capped PbS layer of the QDSC stack led to its oxidation which increased its p-doping. This increase in p-doping was used to improve band bending at the homojunction leading to better fill factors in QDSCs. Hence for the purpose of this thesis, moisture free synthesis of PbS and device fabrication was henceforth carried out in moisture and oxygen free conditions expect for the top most-MPA capped PbS layers that were intentionally air oxidized.

Device	average F.F.(%)	max P.C.E (%)
MPA capped layers in GB	39$\pm$0.8	4.13$\pm$0.15
MPA capped layers in air	43$\pm$3.0	4.72$\pm$0.40

Table 4.1: Effect of air exposure of the MPA capped PbS layers in the absorber layer

4.1.3. Effect of absorber layer thickness

The direct bandgap of PbS QD semiconductors gives it large light absorption coefficients that allows maximum light utilization within 1μm thick films. However, the small diffusion lengths of minority charge carriers in QDs limit the maximum thickness of the absorber layer to a few hundred nanometers. As mentioned in Section 2.5, the ideal absorber layer thickness that ensures maximum light absorption and minimum losses due to photo generated carrier recombination is equal to the sum of the depletion layer and the diffusion length. In most QDSCs with ZnO n type layers, this upper thickness limit is around 250 nm. A thickness series was performed to measure the effect of increasing absorber layer thickness on the solar cell performance, the results of which are seen in Figure 4.4. It was observed that devices with 240 nm thick absorber layers showed the best performance after which increasing thickness led to a decrease in performance output. These results are in line with the theory that an increase in the thickness of the quasi-neutral region beyond the ideal absorber layer thickness leads to increased charge carrier recombination leading to lower F.Fs and J_{SC}. Table 4.2 summarizes the performance of devices with different absorber layer thicknesses. While the V_{OC} of all devices is almost

the same, the J_{SC} and F.F. decrease with increasing absorber layer thickness beyond 240 nm due to increased recombination of the photogenerated charge carriers.
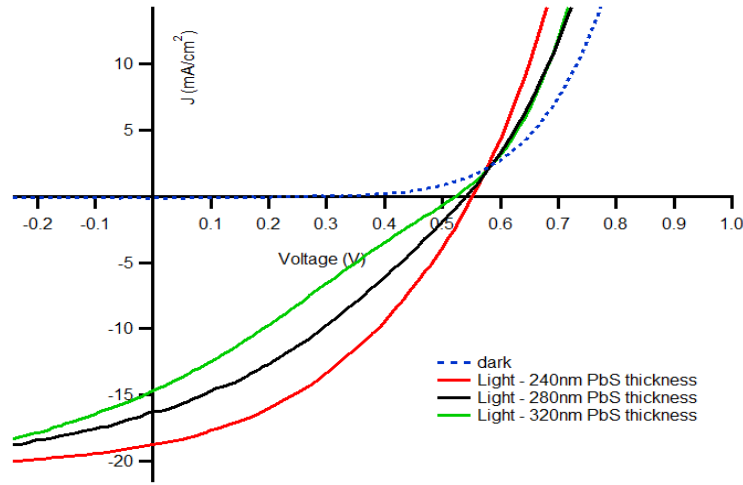

Figure 4.4: Effect of increasing absorber layer thickness on the performance of QDSCs made with all their PbS layers spin coated and ligand exchanged inside a N$_2$ filled glovebox. The dark curves of all three devices did not show much variation. The device with a 240 nm thick absorber layer showed the best performance following which performance deteriorated with a further increase in thickness.

Absorber layer thickness (nm)	V_{OC} (V)	J_{SC} (mA/cm^2)	F.F.(%)	P.C.E (%)
240	0.55±0.01	18.8±0.3	39.9±0.8	4.13±0.15
280	0.54±0.01	16.8±0.7	33.2±2.0	2.92±0.29
320	0.53±0.01	14.8±0.7	26.8±1.8	2.05±0.17

Table 4.2: Effect of PbS absorber layer thickness on the device performance

4.1.4. Charge carrier mobility and lifetime studies

Time resolved microwave conductivity (TRMC) is a technique used to study the mobility and life time of charge carriers in a thin film. Figure 4.5a shows a schematic of the entire experimental setup. In this technique, a thin film of the non conducting sample is placed inside a cell in which a standing microwave in produced as seen in Figure 4.5b. Charge carriers are excited in the sample at the resonant frequency of the microwave by a high intensity laser with 3-5 ns wide pulses which then accelerate in the electromagnetic field formed by the standing microwave. The accelerated movement of the charge carriers extracts work out of the electromagnetic field resulting in a loss of power in the standing microwave which is then measured as ΔP against the inital power (P). The conductance of the sample (G) is related to this loss in power by the following equation [95]:

$$\frac{\Delta P}{P} = -\kappa \Delta G \tag{4.4}$$

where κ is the sensitivity of the cavity which depends on the dimensions and the quality of construction of the cavity. In addition, the change in conductance of the sample is directly related to the the sum of the mobilities of charge carriers in the sample (μ_e, μ_h) and for a known value of κ, the maximum change in conductance (ΔG_{max}), conversion efficiency of an absorbed photon into an electron and hole (ϕ) and the intensity of the laser (I$_0$) (fluence) are related to each other by the following equation [95]:

$$\phi \Sigma \mu = \frac{\Delta G_{max}}{\beta e I_0 F_A} \tag{4.5}$$

where β is the ratio of the width and height of the cavity and F$_A$ is the fraction of light absorbed at the excitation wavelength. Using all these data, the TRMC can be used to obtain reliable information on
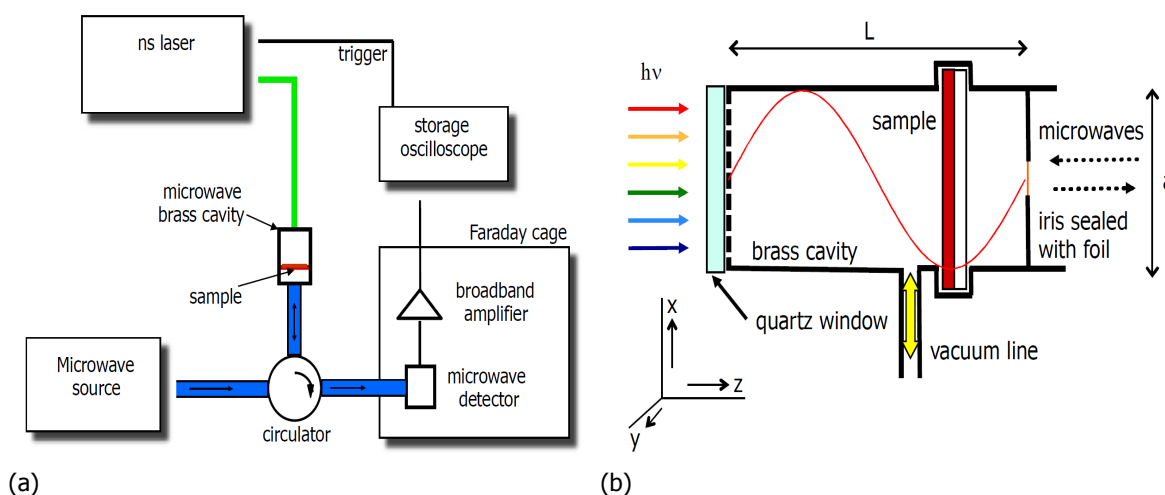
Figure 4.5: a. A schematic of the time resolved microwave conductivity (TRMC) setup used to measure the conductivity of non conducting thin films. While old setups used transmission modes where the microwave was transmitted through the sample and measured for a loss in power on the other side of the microwave source, newer setups use a reflection mode with a microwave circulator to separate the incident microwave from the reflected microwave with marginally lesser power. b. An animation of the brass microwave cavity with height "a" (along 'x' axis) and width "b" (along 'y' axis). A sample of thickness "l" is placed at 3/4ths the length "L" of the cavity (at a maximum of the standing wave) to obtain best results. Light enters the cavity from the left side. Reprinted from reference [95], copyright American Chemical Society 2013.

the mobilities and lifetimes of charge carriers in thin non-conducting films. This technique was used to observe the effects of annealing and air exposure of the QD films on mobility and lifetime of the charge carriers. Due to my limited capabilities with the TRMC experimentation procedure, experiments were carried out by Dr. Ryan Crisp and the results were then discussed and deliberated on. Figure 4.6a shows the effect of different fluences on the combined mobilities of charge carriers in PbS films with different capped ligands. 80 nm films of as prepared PbS QD were prepared by spin coating followed by solid state ligand exchange in the glove box and any physical processing as mentioned. At higher fluences, the high concentration of photo generated charge carriers enhances the Auger recombination pathway which effectively reduces the carrier yield of photons (ϕ) and in turn, the observed combined mobilities of electron and holes ($\Sigma\mu$) in the sample as well. Conversely, as the fluence lowers, the combined mobility increases until a point after which the mobility plateaus even with a reduction in fluence. This plateaued value represents the actual mobility value of the electrons and holes combined in the sample. As expected, the smaller size of PbI_2 as compared to MPA[91], leads to closer packed QDs in films with increased electronic coupling and higher mobility values. While a distinct plateau is not seen, the graphs can be seen to slightly plateau at low fluences as shown by the dashed lines. The combined mobility of charge carriers in unannealed and non-air exposed PbI_2 and MPA capped PbS QD films was observed to be ≈ 0.1 cm^2/Vs and 0.04cm^2/Vs respectively. Annealing the QD films did not seem to show any difference in mobilities as opposed to the assumption it could increase the mobility due to partial fusing of QDs (sintering). Figure 4.6b shows the evolution of the combined mobilities in PbS QD films with different capped ligands with time. After reaching a peak in the first few nanoseconds, the conductivity of the films decay due to increased interaction with other surrounding carriers or trap states where they recombine. While the PbI_2 capped films decay approximately with single slope, the MPA capped QD films (unannealed and annealed ones) decay with a slope until ≈ 130ns following which they decay with different slopes. This could be due to different second order recombination processes of the charge carriers and a consequent variation in the minority carrier lifetimes of both films. Annealed films approximately produce the same results as un annealed films while the annealed and air exposed MPA capped PbS QD film showed a slightly higher intital conductivity value than their unannealed, non air exposed counterparts. This could possibly be due to the oxidation of Pb^{+2} rich surface of the PbS QDs into PbO/ $PbSO_3$ which reduces the number of recombination centres (Pb^{+2} sites) and also introduces new band edge states that act as dopants as described in Section 4.1.2. Fitting the data from the PbI_2 capped films with an exponential equation and the data from the MPA capped films with a double exponential equation, the lifetimes of charge carriers in the different films

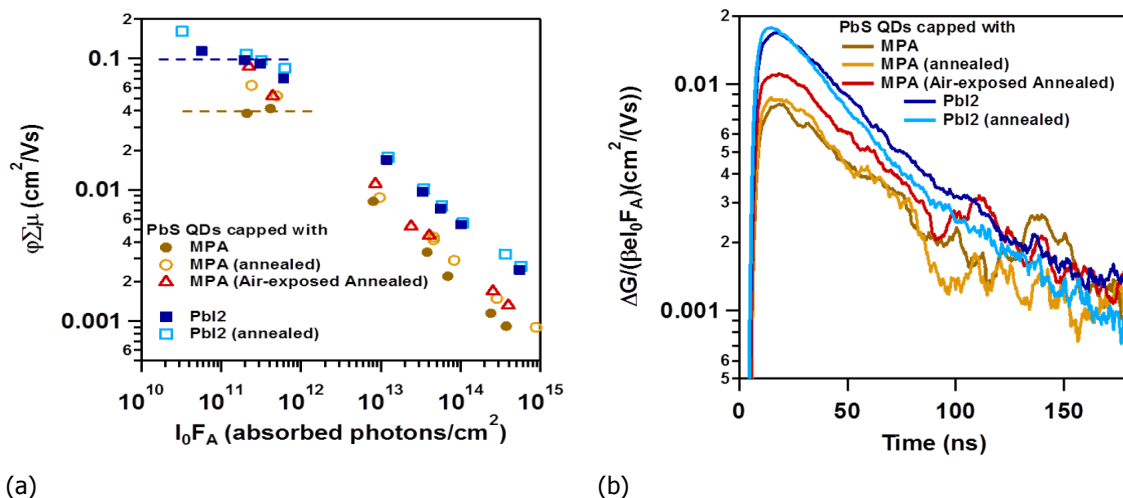(a)   (b)

Figure 4.6: a. A time resolved microwave conductivity (TRMC) plot of the sum of electron and hole mobilities ($\Sigma\mu$) versus fluence considering ϕ is unity. b. A TRMC plot of the film showcasing conductivity decay over time. The lifetime data for this graph use the conductivity data at higher fluences (approx 10^{13} /cm^2) due to the noisy data available at lower fluences. While the data in this graph does not give the exact maximum conductivity values of the carriers in the films, they do provide the trends required to make conclusions about the behaviour of the QD films. All measurements were carried out in a resonant cavity setup.

were obtained as detailed in Appendix Table A.2 and Figure A.8.

Thus, the results from the TRMC experiments on PbS films showed that annealing the films did not help improve the mobility of charge carriers as hypothesized earlier where as air exposure of the MPA capped ligands helped slightly increase mobility and lifetime due to possible passivation of the surface Pb^{+2} states by atmospheric oxygen or oxidation products of sulphur from the thiol group in MPA. These experiments hence provided additional evidence that air exposure of the top most MPA capped layers would be beneficial to the device performance as observed in Section 4.1.2 and Figure 4.3b.

4.2. Systematic study of metal oxide layer

One of the main components of the PbS QDSC configuration is the n type metal oxide layer that aids in electron extraction from the absorber layer and effectively blocks holes. While ZnO NCs, ZnO solgel, TiO$_2$ (undoped or Zirconium doped) have been used extensively to make devices, a systematic study of the effects of the different materials was not found in literature. This section deals with the effect of different n-type metal oxide layers on device performance. We first look into the conduction properties of the different metal oxide materials through TRMC studies followed by their effect on the performance of QDSCs.

4.2.1. Effect of different n-doped metal oxide layer

The TRMC studies on the different metal oxide layers can be summarized by Figures 4.7a and 4.7b. The combined mobility of charge carriers as seen in Figure 4.7a is the highest in TiO$_2$ followed by ZnO prepared by the nanocrystal (NC) and solgel route respectively. The similar results obtained for ZnO NC over two different measurement cycles proves reproducibility of the results obtained. The reason for observed order of mobilities in the different materials is unclear but could be due to the difference in trap state density since a low trap state density leads to high mobility of charge carriers and a correspondingly high photo-conductivity. Combining these results with the carrier lifetime data from Figure 4.7b, a conclusion can be made that TiO$_2$ films have a low trap state density due to their observed high combined charge carrier mobility and longer carrier lifetime. The ZnO films fabricated via the solgel route undergo complex pyrolysis reactions during annealing to give the final ZnO product which could possibly lead to the presence of other impurities (possible hydroxides of Zinc) in the ZnO lattice. While these impurities may lead to low mobilities due to higher coulombic interactions between the impurities and charge carriers, they also increase the trap state density in the ZnO film. However, despite this, their low mobility of carriers could lead to larger lifetimes before they get trapped in trap sites or collide
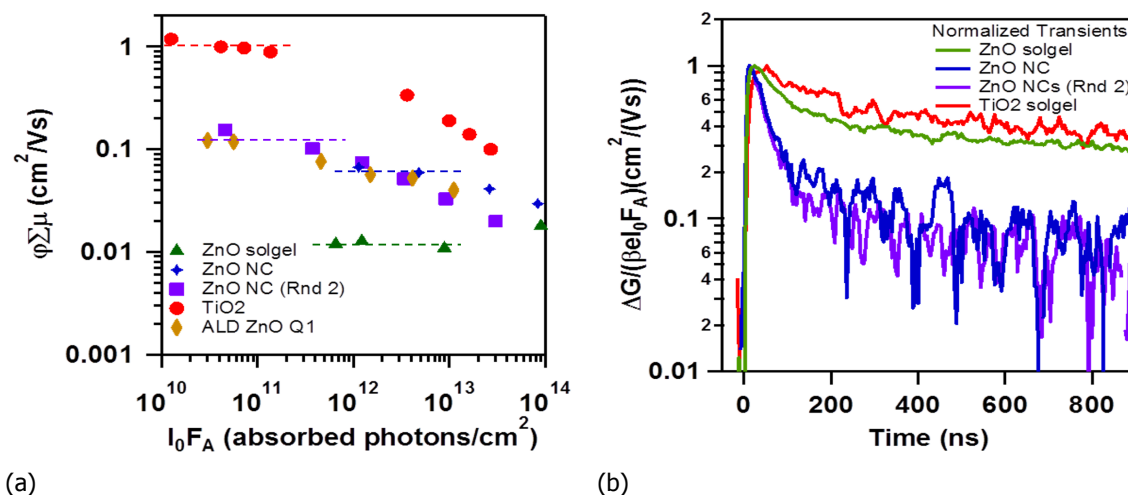
(a)   (b)

Figure 4.7: TRMC plots of the different n type metal oxide layers used in QD heterojunction solar cells. a. Combined charge carrier mobility vs. fluence. The dashed lines approximate the region where the plots plateau giving a value of the combined charge carrier mobility. b. Normalized decay plots of combined charge carrier mobility over time from which the trends of charge carrier lifetime can be observed. While ZnO NCs have higher mobilities relative to ZnO solgel, this leads to lower lifetimes. TiO_2 shows the best results of the 3 different materials

with an impurity atom. On the other hand, ZnO films made from ZnO NCs get their n-doping from oxygen vacancies present in the ZnO NC surface and while the absence of impurities may lead to a higher mobility of carriers in these films compared to the films prepared via the solgel route, the higher mobility also could lead to quicker trapping of charge carriers in the trap sites leading to shorter carrier lifetimes. Combining the mobility and lifetime values for charge carriers in the different layers we can roughly estimate that the diffusion lengths of charge carriers (L_D) in each film (Appendix, Figure A.9 and Table A.3) which follows the trend TiO_2 > ZnO NC > ZnO solgel. Thus from these results, it can be inferred that TiO_2 could be a good metal oxide material for PbS QDSCs.

Figure 4.8a and Table 4.3 compare the J-V plots of devices fabricated under similar process conditions (240 nm thick PbS QD layer, prepared inside the glovebox) with different metal oxide layers. Best results were obtained with 20 nm thick ZnO NC films while TiO_2 films offered the worst results. A distinct "S" shape was seen in the J-V curve of the device with TiO_2 in the power producing quadrant while a slight change in curvature of the plot was seen in the device with ZnO prepared via the solgel route. To further understand device behaviour, an absorber layer thickness series was performed on QDSC devices with TiO_2 as the n type metal oxide layer, the results of which are seen in Figure 4.8b.

Metal oxide layer	V_{OC} (V)	J_{SC} (mA/cm^2)	F.F.(%)	P.C.E (%)
TiO_2	0.49$\pm$0.03	8.2$\pm$1.7	16.0$\pm$1.4	0.6$\pm$0.2
ZnO NC	0.54$\pm$0.03	18.2$\pm$1.0	36.7$\pm$3.5	3.8$\pm$0.5
ZnO solgel	0.54$\pm$0.01	16.7$\pm$0.8	32.8$\pm$2.9	2.9$\pm$0.3

Table 4.3: Compilation of external parameters of the devices with different n type metal oxide layers

The absorber layer thickness series with a constant TiO_2 thickness shows that an increase in the absorber layer thickness leads to poorer performance of the solar cell with an increase in the "S" shape of the curve. This shows that increasing the absorber layer thickness possibly led to an increase in the thickness of the quasi-neutral region which points towards a thinner ideal absorber layer. Additionally, this also opens the possibility of a lower charge carrier density in the TiO_2 since this would lead to a thinner space-charge region (depletion width) in the absorber layer and a thicker quasi-neutral region. In such a case, the "S" shape in the J-V curve would be a result of the increased F.F. that accompanies increased recombination of photo generated charge carriers. While this issue can be tackled with a

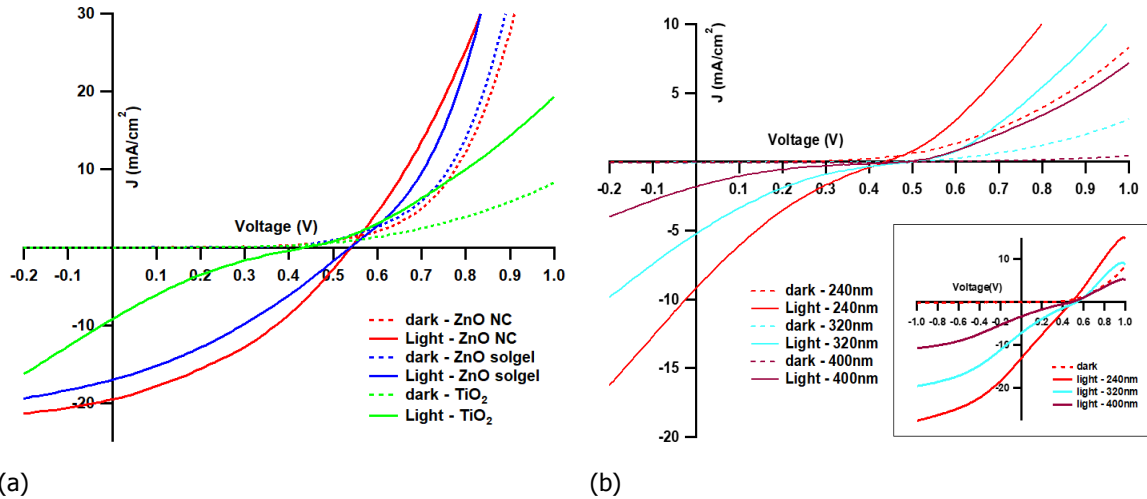(a)   (b)

Figure 4.8: a. A plot comparing the effect of 3 different n type metal oxide layers on solar cell performance. Contrary to the TRMC results, devices with ZnO NC showed best results while devices with TiO₂ (and ZnO solgel) showed a "S" type curve with low F.F. and high series resistances. b. A PbS absorber layer thickness series showed that the thickness of the absorber layer was the not reason behind the poor performance of devices with TiO₂. The inset shows a comparison of the same plots in a reverse voltage sweep. The "S" shape is evident in both forward and reverse voltage sweeps.

thinner absorber layer, it would come at the cost of absorbed photons with longer wavelengths which would also affect the device performance thus making TiO₂ not an ideal metal oxide layer.

Another reason for this "S" shape could be the doping profile and position of electronic bands with respect to the vacuum level of TiO₂. Figures 4.9a and 4.9b shows the different types of band bending that can occur at the metal oxide layer/PbS layer interface. Lesser n type doping density of the TiO₂ would lead to a shallower CBM that is farther away from the Fermi level as seen in Figure 4.9a. In such a case, during the junction formation, when electrons move from the TiO₂ into the deep work function PbI₂ capped PbS layer, an unfavourable band bending occurs as seen in situation (a). On illumination and subsequent J-V characterization, when the applied voltage is in the reverse bias zone, the negative voltage pushes the conduction band minimum (CBM) energy levels of the PbS layer above that of the TiO₂ layer which promotes electron injection into the TiO₂ layer leading to normal diode behaviour. As the voltage becomes less negative, the CBM energy levels of the PbS layer moves below that of the TiO₂ layer leading to accumulation of the photo generated charges at the interface. Since the accumulated charge carriers at the interface do not get collected in the external circuit, there is a flattening of J-V curve giving it the characteristic "S" shape. Once the applied voltage enters the positive bias zone and becomes more positive, the depletion region cancels out and the diode begins to conduct leading to a sharp increase in current density. Figure 4.9b shows a scenario wherein a higher n type doping density and deeper CBM levels lead to favourable band bending that gives rise to a good J-V response to illumination.

While a steep "S" shape is observed in devices with TiO₂, a mild change in the curvature of the J-V curve is observed close to the V_{OC} in devices with ZnO films made by the solgel method. Based on all the above discussions, this would mean that the doping concentration in such films is higher than in the TiO₂ films but still not ideal enough to extract maximum results out of the QDSC. Another test was performed to reaffirm the above hypothesis and to improve the performance of devices with the ZnO films prepared *via* the solgel route. Similar to the experiments performed by Willis *et al.*[70], fully fabricated devices were light soaked (UV soaking) for a duration of 60, 120 and 180 seconds, the results of which are tabulated in Table 4.4 and J-V curves can be seen in Figure 4.10. A clear decrease in the "S" shape of the J-V curve is seen for the first 120 seconds after which the performance seems to stagnate. This could be due to the possible increase in "n" doping of the metal oxide layer under UV light which would improve band bending at the ZnO/PbS interface, increase the depletion layer in the PbS layer and ensure better carrier collection (as proven by the increase in F.F. as seen in the inset of Figure 4.10)
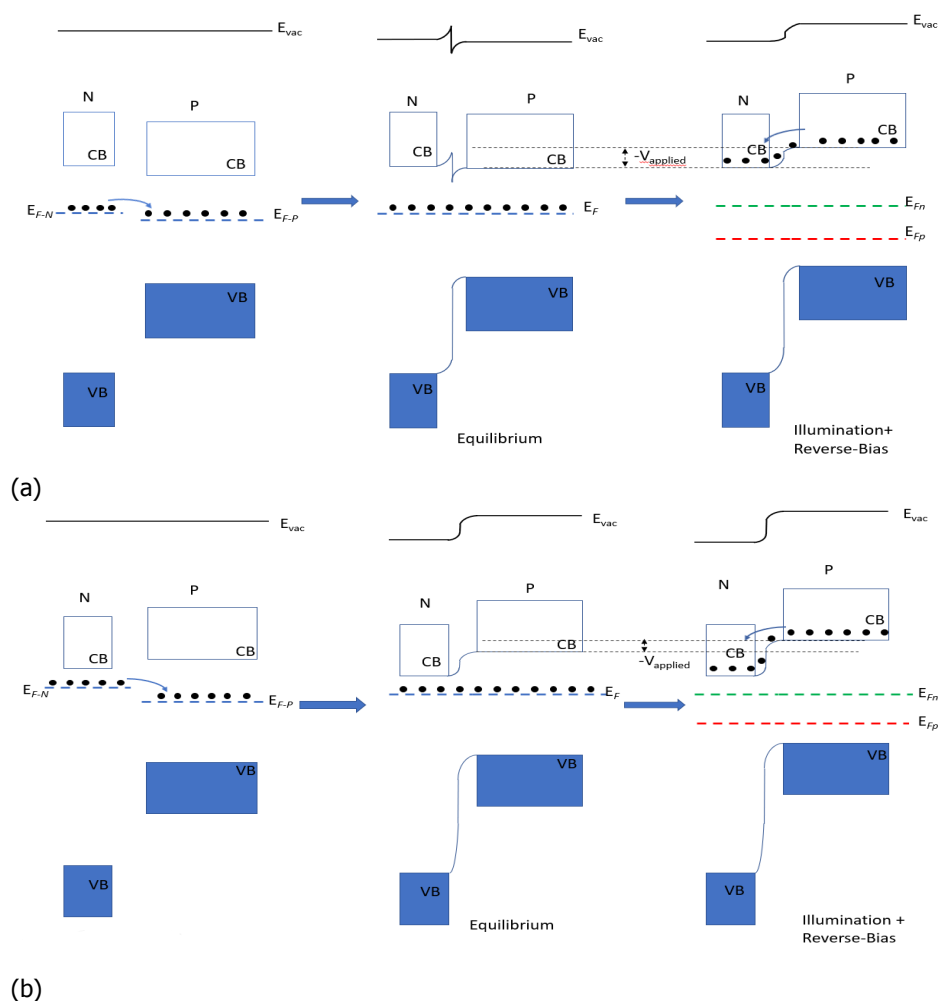
(a)

(b)

Figure 4.9: A schematic showing the band bending that occurs at the metal oxide/PbS layer interface in the case of a metal oxide layer with a) a low doping density and b) a higher doping density. The right most diagrams in both the scenarios show how the interface reacts to the application of a reverse bias voltage when the device is under illumination.

Summarizing the results in this section, it was observed that despite showing promising results with the TRMC measurements, TiO_2 proved to be the worst of the 3 metal oxide layers used in this thesis when used in conjunction with PbS QD layers in QDSCs. This was attributed to the low doping density and unfavourable energy level alignment of TiO_2 with respect to the deep energy levels of PbI_2 capped PbS QDs as this lead to unfavourable band bending as seen in Figure 4.9a. To prove this hypothesis, the devices using a ZnO solgel metal oxide layer that showed a mild "S" shape in the curvature (in comparison to the steep "S" shape in the J-V curves of devices with TiO_2) were soaked in UV light for different duration since this is a known method to improve the doping density of ZnO. As expected, the S shape reduced with UV soaking of the devices allownig us to conclude that improving the doping density or pushing down the energy levels of TiO_2 (and ZnO solgel) films could lead to better PbS QDSCs.

4.2.2. Effect of n-doped metal oxide layer thickness

As seen in the previous section, best device performance was observed in devices with ZnO films prepared from ZnO NC. A thickness series of this metal oxide layer was performed to further optimize the performance of the devices. Figure 4.11 shows the results obtained by varying the thickness of the ZnO layer and the devices with a 20 nm ZnO film showed best results. Profilometry scans performed on the films with different thicknesses show a thickness of ≈30 nm and 20 nm as seen in Figures A.3a,
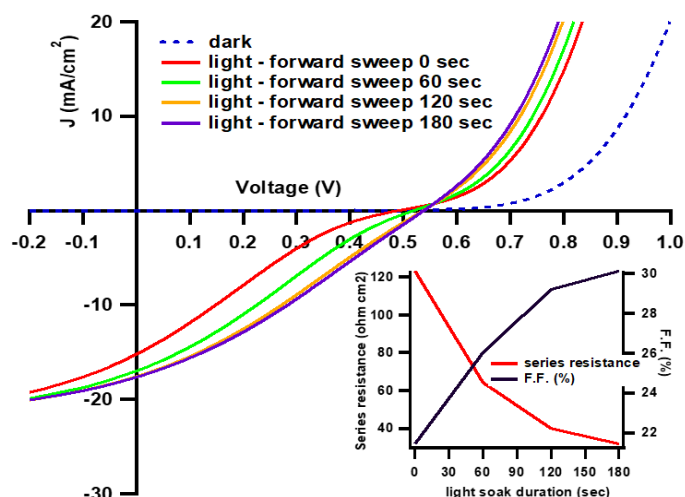
Figure 4.10: Effect of lightsoaking the ZnO layer, prepared via solgel route, on the performance of QDSCs. Prolonged lightsoaking was seen to remove the "S" shape in the plots and also improve the external parameters like the F.F and series resistance as seen in the inset.

Light soaking duration (sec)	V_{OC} (V)	J_{SC} (mA/cm^2)	F.F.(%)	P.C.E (%)
0	0.479	15.06	21.43	1.55
60	0.508	16.88	26.02	2.23
120	0.524	17.50	29.19	2.68
180	0.527	17.60	30.12	2.79

Table 4.4: Compilation of evolution of external parameters under light soaking of a QDSC with a ZnO layer made *via* the solgel route.

A.3b. The thickness of the other device with a thinner films was extrapolated to be 18 nm.

As mentioned before, the oxygen vacancies present in the lattice of the ZnO layer lead to an excess of positive charge in the ZnO film. To preserve charge neutrality in the film, it is possible that electrons flow into the film to balance this excess positive charge, leaving behind a film with excess electrons that gives it an n-doping. However, these oxygen vacancies also act as trap sites that assist in the recombination of charge carriers which is detrimental to device performance. This limits the total thickness of the n-type layer. Conversely, a too thin film could limit the total charges present in the film that in turn reduces the thickness of the depletion layer formed in the absorber layer. Observing the results, we can concur that the 30 nm ZnO film was too thick that the loses due to recombination at the high number of trap sites dominated, causing poor performance of the devices while the 18 nm film was too thin that it did not have enough charge carriers to produce a wide enough space-charge region in the absorber layer leading to a thicker quasi-neutral region. Thus, in this thesis, 20 nm was found to be the ideal thickness for the ZnO NC film that had a high enough charge carrier density to produce a wide space charge region and minimized the carrier recombination losses to not cause any significant impact to deteriorate device performance.
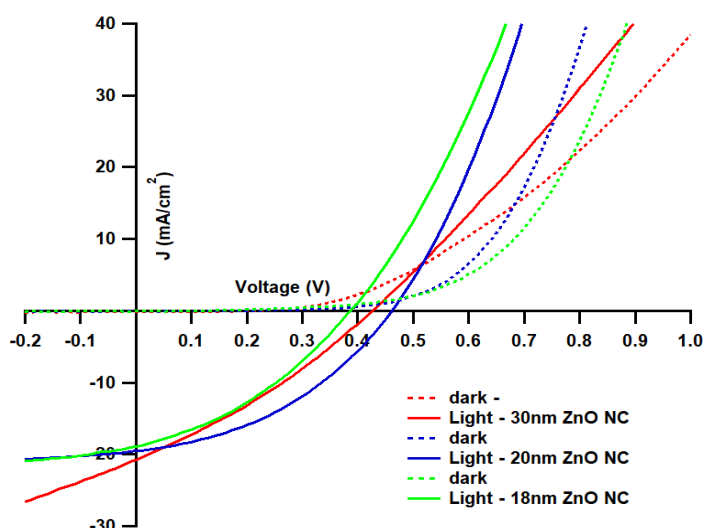
Figure 4.11: Effect of metal oxide layer thickness (ZnO NC) on the performance of QDSCs made with all their PbS layers spin coated and ligand exchanged inside a N_2 filled glovebox. Best results are seen on the device with a 20 nm thick ZnO layer while thicker and thinner layers seemed to be detrimental to device performance. A comparison of the absorption sepctra of the CQD solution used to make devices with 30 nm thick ZnO layer and the remaining devices is shown in Figure A.10

4.3. Electrochemical Doping

As mentioned in Section 2.5, increasing the diffusion length by improving surface passivation of the QDs and increasing the depletion width by increasing the doping density of the n-type metal oxide layer are two of the main approaches that have been used in improving QDSC performance. However, electrochemical doping of thin films has gained popularity in recent times with Houtepen and colleagues demonstrating the same in reference [82]. Using this concept to dope QD layers could lead to a controllable doping method as opposed to other methods like atomic doping wherein the actual doping amount cannot be precisely controlled. The following section shall detail efforts at implementing electrochemical doping techniques into solar cell devices.

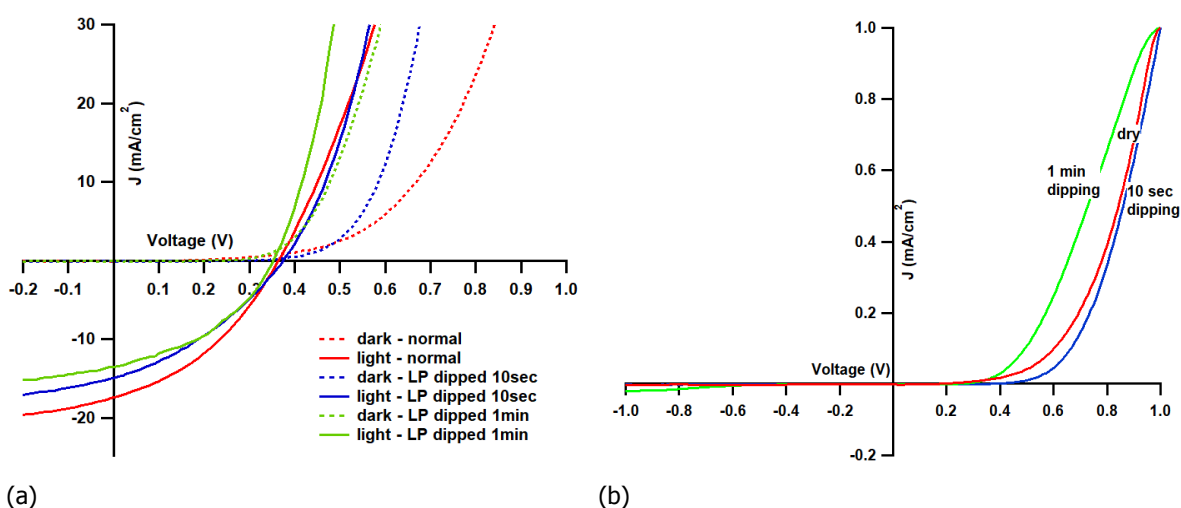(a)   (b)

Figure 4.12: a. Effect of dipping the entire QDSC stack in an electrolyte ($LiClO_4$ - referred to as LP) on the performance of QDSCs (made similar to the champion device). The dark curves were seen to change due to a possible change in the doping concentration in the device stack contrary to our theory that the ions would screen the ions in the depletion layer. b. Normalized diode curves of the device under dark before and after electrolyte dipping. Color coding is the same as in the adjacent figure. While the cut in voltage for the diodes under all three conditions is almost the same, the curvature of the graphs change after the diode start conducting denoting a possible change in the ideality factor of the device.

To begin with, the effect of exposure of an entire QDSC stack to an electrolyte solution was probed to determine the behaviour of the device under exposure to ions in an electrolyte. An electrolyte with mobile ions and a volatile solvent was chosen for the quick diffusion of ions through the stack and the easy evaporation of the solvent without leaving behind any residue. A 0.1M solution of lithium perchlorate ($LiClO_4$) [LP] in anhydrous acetonitrile was prepared in a N_2 environment for this purpose. In this experiment, fully prepared QDSC stacks were dipped in the electrolyte solution for different time periods following which they were dried and then tested, the results of which are shown in Figure 4.12a.

Our initial hypothesis as seen in Figure 4.13 expected the ions to diffuse through the layers in the stack towards the charges present in the depletion region and screen the built-in electric field. In drift driven devices like QDSCs, the charges in the depletion layer produce an electric field that induces the drift transport of photogenerated carriers. In such a system, screening of the charges in the depletion region would nullify the effect of the built in electric field thereby resulting in a loss of rectifying and photovoltaic behaviour across the device under dark and light conditions respectively. However, the results in Figure 4.12a show somewhat different results than what was expected. It was observed that the threshold voltage of the dark curves of the device as well as the J_{SC} of the device under illumination reduced with increased exposure to the electrolyte. While this shows that the screening of charges probably did not occur in full, the change in device performance with time of exposure to the electrolyte prompted us to believe that the diffusion of the ions through films was not complete. Since ions move under the influence of an external electric field, it was decided to apply a bias across the devices while exposing it to the electrolyte. It is also predicted that a longer duration of electrolyte exposure could allow the complete diffusion of ions inside the device leading to an end result as hypothesized in 4.13. Analyzing the results in Figure 4.12a and 4.12b, the observed change in the curvature of the normalized dark J-V plot shows that the exposure of the QDSC stack to the electrolyte possibly leads to a change in the ideality factor the saturation in the diode equation (Equation 4.2). However, due to the difficulty in pinpointing the exact reason behind this behaviour, it was decided to use a more systematic approach in approaching the task at hand.
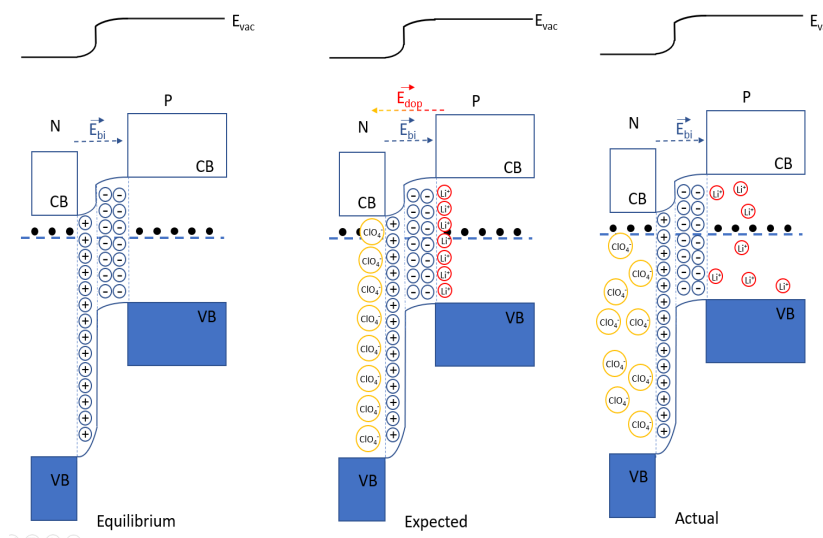

Figure 4.13: Our initial hypothesis of the electrolyte exposure suggested that the ions in the electrolyte would screen the ions in the space-charge region but the opposite was observed due to probable lack of ion diffusion.

While in most literature, the heterojunction is assumed to be the dominant junction in QDSCs fabricated by our method, Rekemeyer et al. [94] showed that the junction at the absorber layer/HTL interface was indeed the dominant junction. Due to the ambiguity involved in deciding the dominant junction, it was decided that both junctions be done away with and we try to electrochemically dope a thin film of PbS QDs (160 nm) in a simple FTO/PbS/Ag configuration (which is also a QD Schottky junction solar cell configuration). The band structure of this configuration is shown in the "Equilibrium" part of Figure 4.14. In the following experiments with this configuration, the J-V characteristics was first

measured in the dark followed by "electrochemical doping" and a second round of J-V characterization under dark and illumination. The steps involved in electrochemical doping (ED) are the application a drop of electrolyte on the film and the immediate application of a forward/ reverse bias for a duration exceeding the time taken for the solvent to evaporate. The preliminary results of electrochemical
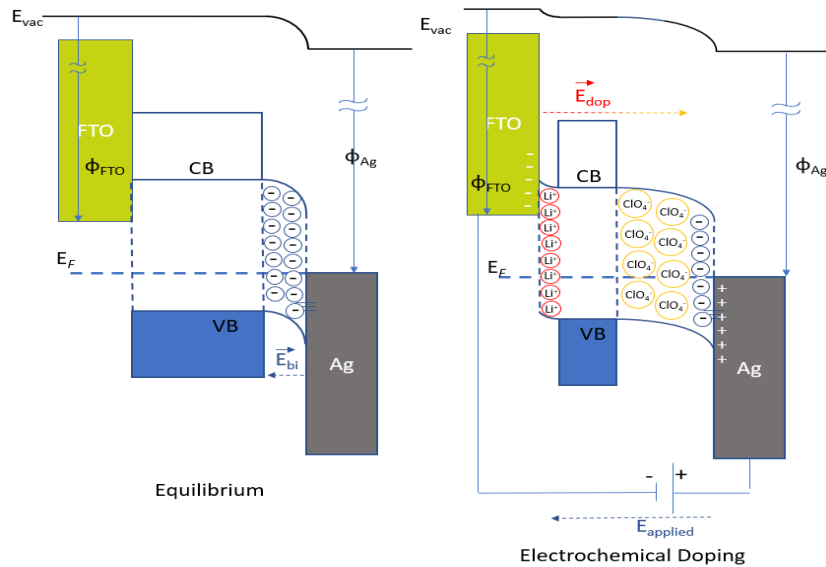

Figure 4.14: On the left hand side diagram, a basic Schottky junction device is shown with its depletion region at the rear contact between the Ag and PbS. As per our initial hypothesis of the electrolyte exposure, it is possible that the ions in the electrolyte screened the ions in the space-charge region which however led to a band bending as seen in the right hand side diagram .

doping are shown in Figure 4.15a. Under dark conditions, without any electrolyte exposure, a clear rectifying behaviour is observed with a high threshold voltage. Under illumination though, these devices hardly show any photovoltaic behaviour which is possibly due to the very small depletion region formed at the PbS/Ag interface leading to a thick quasi-neutral region. However, post electrochemical doping (exposure of the film to the electrolyte and a simultaneous application of a forward bias), more interesting observations can be made. While prior to ED, the device conducts only after a positive threshold voltage, after ED, a different behaviour is observed with the diode conducting in both directions with different threshold voltages. The measurements were repeated to check that diode breakdown had not occurred and it was confirmed that there was no diode breakdown. To ensure that this change in behaviour of the device was not due to the application of a bias voltage alone, a separate experiment was devised to compare the effect of applying a forward and reverse bias with and without any electrolyte on the device behaviour under dark, the results of which are seen in Figure 4.15b. Here, we observe that without any electrolyte exposure, the application of a forward bias (+0.5V) reduced the threshold voltage of the dark curve while a reverse bias (-0.5V) increased the threshold voltage of the dark curve of the device. Another important observation in these curves is that the "rectifying" behaviour of the diode which allows it to conduct only under positive voltage stays. However, on introducing the electrolyte and electrochemically doping it with a reverse bias, the rectifying behaviour was lost and the diode began conducting in both directions with a very low threshold voltage. Comparing these results with the electrochemical doping under a forward bias (+0.5V) in Figure 4.15a we can observe that the forward biasing leads to a sharper spike in current at the threshold voltage. These reason behind these interesting observations can be explained by the schematic shown in Figure 4.14.

(a)   (b)
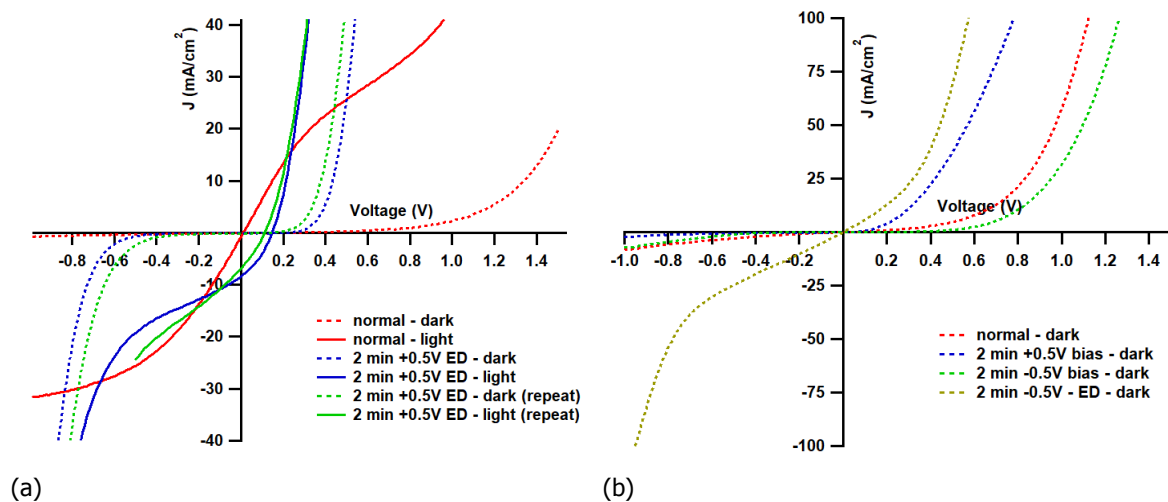
Figure 4.15: a. Effect of electrochemical doping (ED) by applying a forward bias (+0.5V) on the Schottky junction PbS QDSC during exposure to the electrolyte (LiClO$_4$). Post electrolyte treatment, the Schottky junction behaviour is lost and a sort of a metal-semiconductor-metal junction behaviour is observed in the dark. Under light, photovoltaic behaviour was observed post electrolyte treatment. b. A comparison of the effect of applying a bias voltage across the QDSC with and without the electrolyte on the dark J-V curves. The application of forward (+0.5V) or reverse biases (-0.5V) without any electrolyte (blue and green curves) changes the threshold voltage while maintaining diode behaviour whereas the rectification of the device is lost when electrochemical doping (ED) (golden brown curve) is done.

During electrochemical doping, the application of an external electric field on the device is expected to attract the ions in the electrolyte towards electrodes with a charge opposite to that of the ions. This "gating" is performed until the solvent dries to prevent propagation of ions, away from the respective electrodes and ensure their subsequent sticking near the intended electrodes. Once these ions are locked at their respective electrodes, they screen the external electric field by forming an equal and opposite electric field inside the PbS layer and retain this electric field even when the external bias is removed. However, due to the accumulation of charges at each end of the PbS layer, it is possible that opposite charges are induced electrostatically in the electrodes at both the interfaces leading to dipole moments on either side of the PbS layer which subsequently gives rise to band bending as seen in Figure 4.14. It is expected that, the accumulation of ions leads to an increase in the depletion width at the rear interface which marginally improves the photovoltaic behaviour of the electrochemically doped films. In addition, it is also possible that the introduction of band bending at the front inter- face (FTO/PbS) could lead to a rectifying behaviour in reverse bias due to a small depletion region formation which could explain the double diode like behaviour under dark conditions. While this effec- tively destroys the "rectifying" behaviour of a diode, it was hypothesized that the reverse case where a "non-rectifying" device could be made rectifying with electrochemical doping could be possible. A few symmetric metal-semiconductor-metal devices were fabricated towards achieving this but due to the time constraint involved in this thesis, none of them could be made to work. Figures A.11a and A.11b show the configuration of the device and the results obtained.

Thus, the observations from the experiments on electrochemical doping can be summarized as follows. The preliminary tests showed that the PbS QD films show a definite change in behaviour on exposure to an electrolyte solution which confirms the diffusion of ions through the porous QD films which is the first step electrochemical doping. Since the duration of electrolyte exposure of the QD films was limited to a within 1 minute during the course of this thesis, it is possible that the permeation of ions through the QD film is slow which is why we weren't able to obtain conclusive evidence. However, this can lead to possible future work that can focus on conducting a systematic study to determine the optimal duration of exposure to ensure complete permeation of the ions into the bulk of the QD films. The second round of experiments showed that electrochemical doping of the films, wherein the films were exposed to an electrolyte and simultaneously "gated" by a bias across them, was able to partially improve the photovoltaic behaviour of the QD films. Additionally, a change in the behaviour of the device on changing the polarity of the biasing during electrochemical doping showed that ion diffusion through the film could possibly be controlled by the magnitude and polarity of the gating voltage which

provides secondary evidence of the possibility of electrochemical doping of QD films. Finally, due to time constraints associated with the completion of this thesis, no change in the rectifying behaviour of the symmetric metal-semiconductor-metal devices could be established that would present conclusive evidence of electrochemical doping. However, the above results provide a good amount of evidence towards the possibility of this doping method that can encourage further research in this field. As an additional idea, it could be beneficial to work on means to fix the ions at their locations by either freezing the solvent at room temperature or using solvents that can be made to polymerize under controlled conditions..

5

Conclusions and Recommendations

In conclusion, PbS QDSCs were successfully fabricated for the first time at TU Delft. The ideal configuration involved using a 20 nm thick ZnO layer made using ZnO NCs, 240 nm thick PbS layer with QDs in the top 80nms capped with MPA ligands and the remaining capped with PbI_2, a 50 nm layer of MoO_x and a 250 nm layer of silver to finish the back contact. Despite promising conductivity and lifetime measurements of TiO_2 in the TRMC, it was found to not provide good results in combination with PbS QDs in solar cell devices possibly due to a low doping density. While controlled air oxidation of the top HTL layers was observed to improve the F.F. and P.C.E of the solar cell devices, exposure to excessive moisture (RH > 50%) was found to impact the devices negatively. Hence, an air-free synthesis method combined with a fabrication protocol involving partial QD film stack development inside the glovebox was used in achieving our champion device. Electrochemical doping of the PbS layers was attempted and some evidence of the influence of the ions in the electrolyte on device performance was observed. While one of the goals of the thesis was to convert a non rectifying PbS film into a rectifying diode, due to time constraints, this was not achieved.

While this thesis systematically studied the effects of processing conditions and materials on QDSC development, there are some recommendations that can be suggested for future research. $TiCl_4$ treatment on TiO_2 (followed by annealing) has been shown to lower the CB of TiO_2 by inducing a dipole moment on the surface[96]. Since this could potentially improve the performance of our QDSC devices with TiO_2, this treatment can be studied to see if the champion solar cell efficiency achieved in this thesis can be exceeded. In addition, Fermi level and CB positions of the different metal oxide layers could be studied with the help of an electrochemical setup or an x-ray photoelectron spectroscopy (XPS) to verify the many hypotheses in this thesis. The metal-semiconductor-metal devices fabricated in the last 2 weeks of this thesis duration showed ohmic behaviour either due to the fabrication in ambient conditions that led to pinhole formation or due to an unfavourable band bending. Optimizing the device configuration by fabricating devices with different PbS layer thicknesses inside the GB could help narrow down the actual reason for the said behaviour of these devices. Additionally, the electrochemical doping procedure could also be improved by using different electrolyte solutions with salts that have ions that are mobile enough to diffuse through the QD solids under an electric field but large enough to be locked in their positions when the solvent evaporates. Another approach in this regard is to use solvents like polyethylene glycol (PEG) that freeze (or polymerize) under room temperature and lock the ions in their intended place. Finally, it has to be noted that lead is a carcinogenic material and using it in a "clean technology" like solar energy is an opposing ideal. It is important that we utilize the knowledge obtained from PbS solar cells in the development of solar cells of other QD materials like indium phosphide (InP). Thus, this thesis has successfully laid the foundation for QDSC research at TU Delft and also introduced a novel pathway towards achieving a simple and accurate doping mechanism for QD films.

A

Appendix

A.1. Thickness measurements

Material	average thickness $\pm$ error(nm)
PbS - 1 layer	43.34 $\pm$ 1.65
PbS - 2 layers	78.43 $\pm$ 2.71
PbS - 3 layers	116.00 $\pm$ 1.00
MoOx	57.02 $\pm$ 1.15
Ag	260.60 $\pm$ 3.96
ZnO NC (900rpm)	32.16 $\pm$ 2.79
ZnO NC(2000rpm)	21.65 $\pm$ 1.84
ZnO solgel (3000rpm)	35.55 $\pm$ 0.38
TiO$_2$ (14000rpm)	42.89 $\pm$ 3.00

Table A.1: Thickness measurements of the different layers in the QDSC stack. To measure the actual thickness of each individual spin coated PbS layer and ensure repeatibility, measurements were taken upto 3 layers for PbS alone.
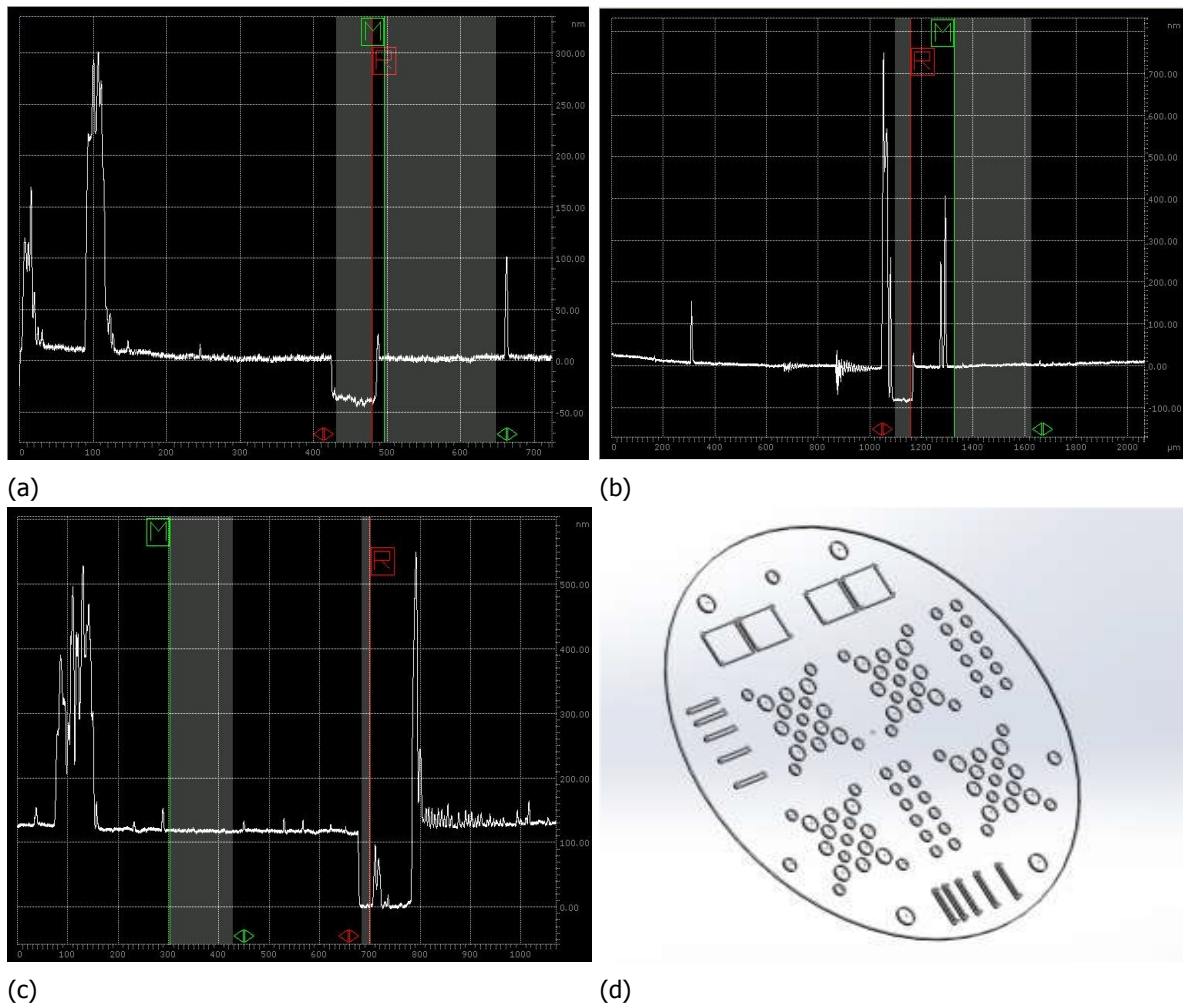
(a)

(b)

(c)

(d)

Figure A.1: Thickness measurements of PbS layers, spin coated with 20 mg/mL CQD solution in octane at 1400 rpm and solid state ligand exchanged inside a glovebox. a. 1 layer, b. 2 layers, c. 3 layers. Measurements were performed on a Dektak profiler. The measurements of 3 different layers shows the repeatability of the spin coating precedure in depositing ≈40 nm layers. d.The evaporation mask used to control the shape of the back contacts deposited. While the 4 segments corresponding to substrates of (2.45 x 2.45) cm was frequently used, other segments were also occasionally used for smaller substrates.
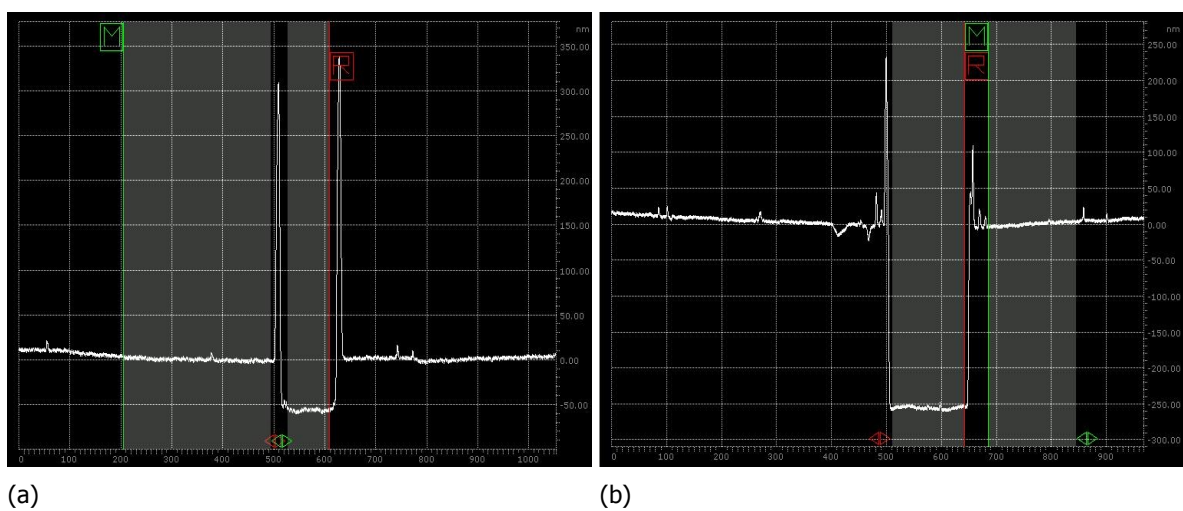

(a)

(b)

Figure A.2: a, b. Profilometry measurements on the MoOx (b) and Ag (c) layers showed that 50 nm was deposited using the mentioned process conditions.
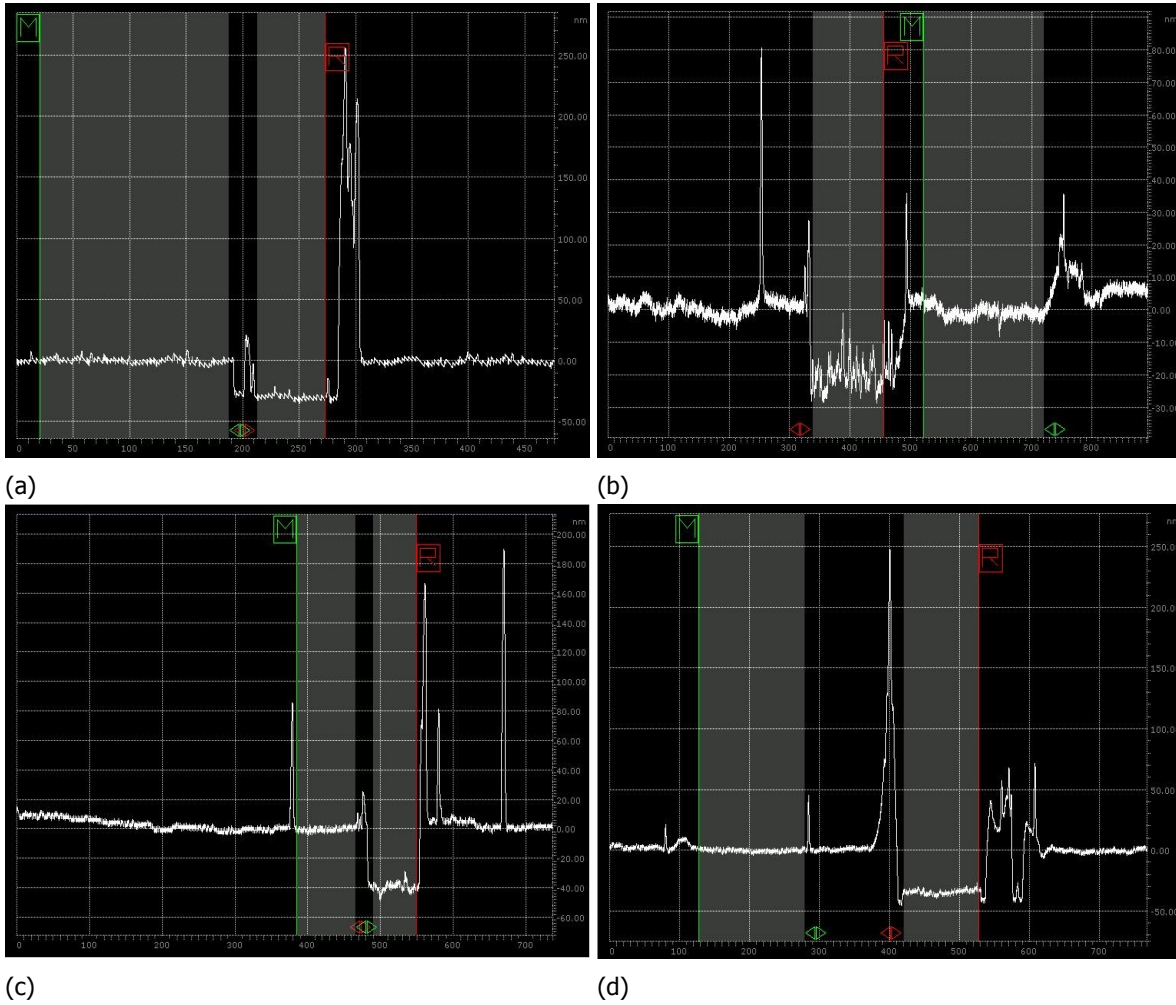
(a)

(b)

(c)

(d)

Figure A.3: Thickness measurements of different metal oxide layers used in the thesis. ZnO NCs in ethanol as described in Section 3.1 spin coated on ITO substrates at a. 900 rpm and b. 2000rpm. Both films were annealed at 260°C. c. TiO$_2$ prepared *via* the solgel method, spin coated at 1400 rpm as prepared in Section 3.2.2 on quartz substrates and annealed at 450°C. d. ZnO prepared *via* the solgel method, spin coated at 3000 rpm as prepared in Section 3.2.1 on quartz substrates and annealed at 200°C. Measurements were performed on a Dektak profiler.
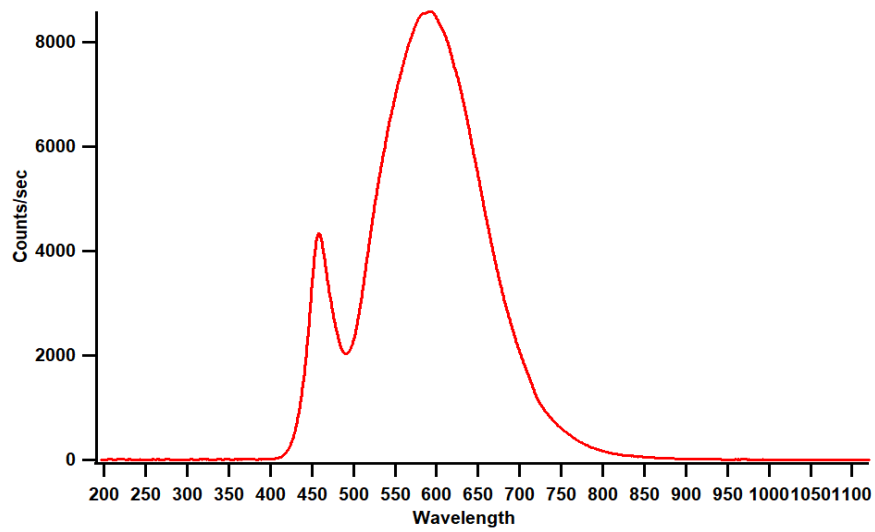
A.2. Results

Figure A.4: The shape of the spectrum of the LED lamp used as a stand by for the solar simulator. While this does not show the actual spectral intensity, it is solely used to depict the shape of the spectrum.
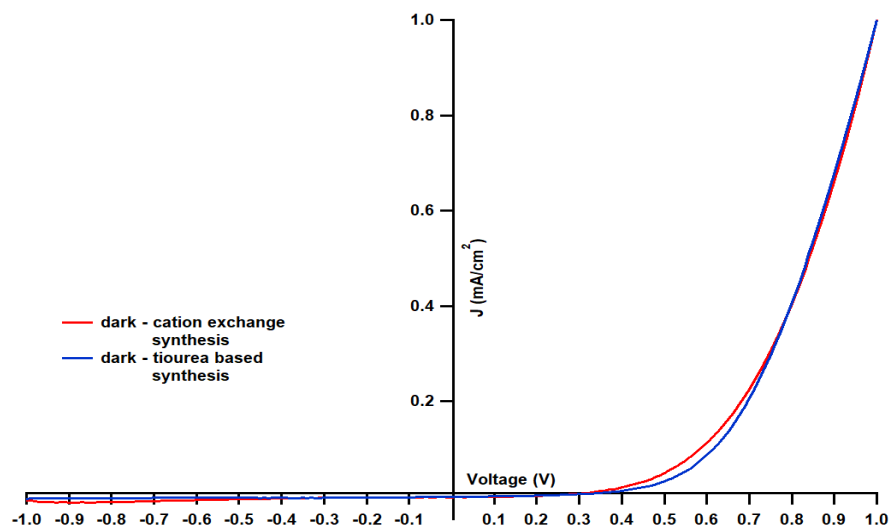

Figure A.5: The data of the dark curves of the two different synthesis methods were normalized to oberve the diode behaviour of both curves. Due to their close matching, it can be approximated that the ideality factor (n) and the saturation current (I_0) of both the devices were comparable to each other.
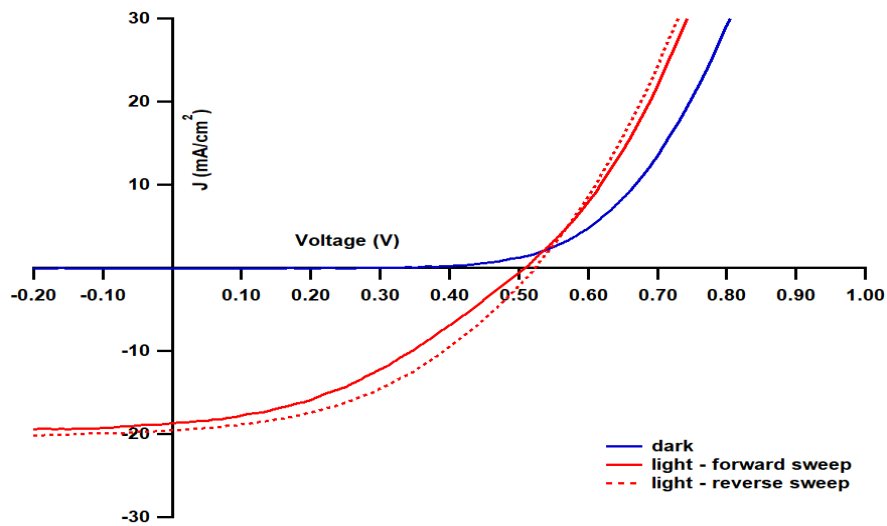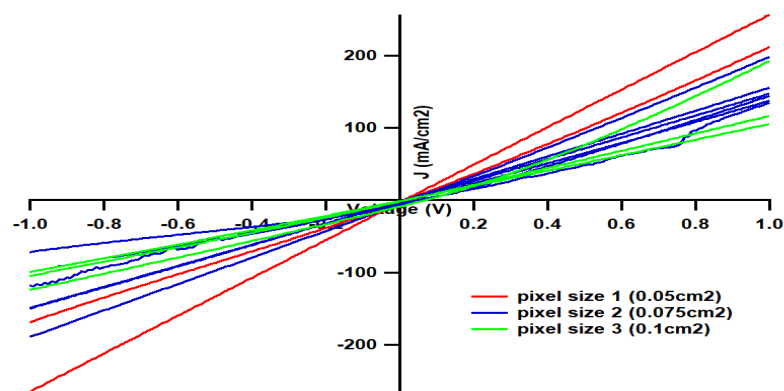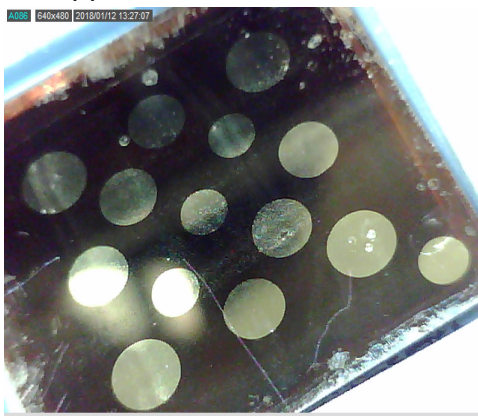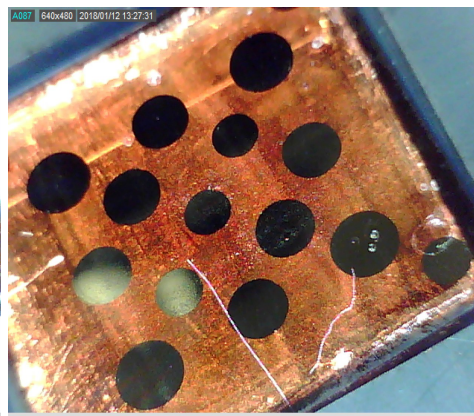
Figure A.6: The J-V curves of a device with ZnO NC, a I^- capped PbS absorber layer and a HTL made from EDT capped PbS QDs. The I^- ligand was obtained from tetramethylammonium iodide (TMAI) instead of the usual tetrabutylammonium iodide (TBAI). These devices showed almost similar behaviour to the devices made with absorber layers made of PbI_2 capped PbS layers.

(a)

(b)   (c)

Figure A.7: a. The J-V curves of the various devices under illumination fabricated during the beginning of the thesis that formed shunts due to the high moisture content in the surroundings and also in the reagents used. b,c. Pictures of the actual devices fabricated under dark (b) and under illumination (c).
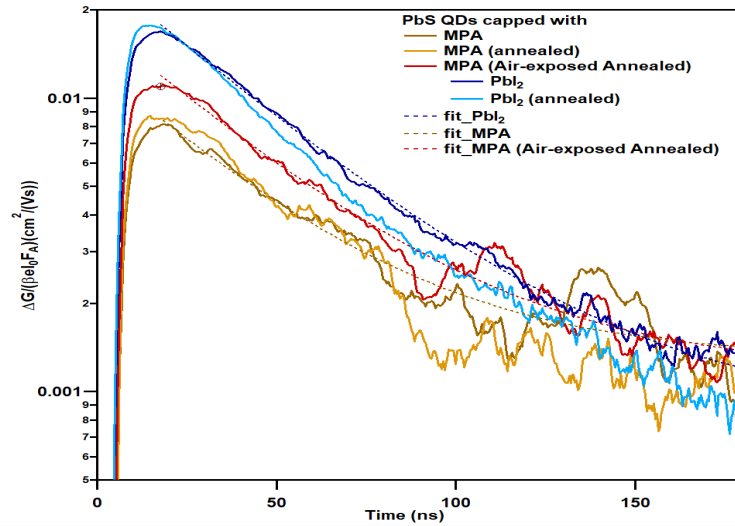
Figure A.8: The conductivity decay curves were fitted with exponential equations to obtain the lifetime values of charge carriers in PbS films with different capping ligands. While data for the PbI_2 capped PbS films was fitted well with a single exponential curve, the data for MPA capped PbS films were fitted with double exponential curves and the lifeteime calculated by a weighted average of the two lifetimes obtained.

	PbI_2 capped, unannealed	MPA capped, unannealed	MPA capped, annealed+air exposed
A_1	0.025844±0.0001	0.0043569±56.7	0.0055127±0.896
A_2	-	0.0070287±56.7	0.01123±0.895
τ_1 (ns)	41.94±0.67	40.03±0.12	46.26±2.74
τ_2 (ns)	-	38.03±0.18	37.78±4.67

Table A.2: Coefficients for lifetime calculation from TRMC plots obtained by the fitting the data in single and double exponential equation.

The formula for the weighted average used to measure the total lifetime was :

$$\tau = \frac{A_1\tau_1 + A_2\tau_2}{A_1 + A_2} \tag{A.1}$$

This gave weighted lifetime values of 38.796 and 40.572 nanoseconds (ns) for the MPA capped "unannealed" and "annealed with air exposure" PbS films respectively.
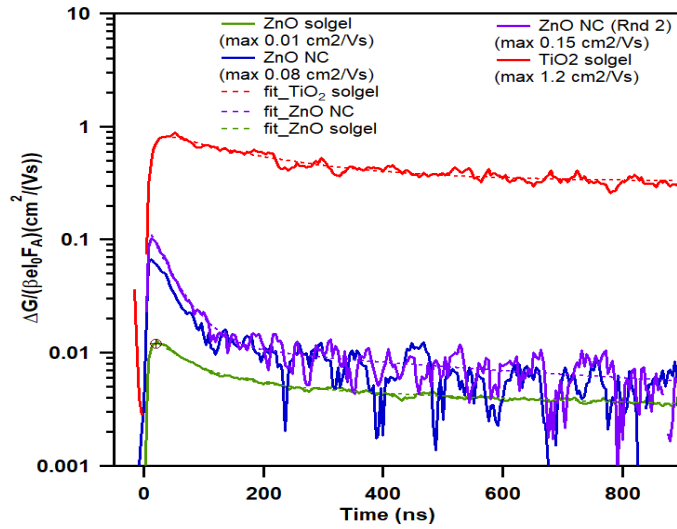
Figure A.9: Actual TRMC conductivity vs time decay plots showing maximum mobility achieved by the charge carriers in the different metal oxide films. The lifetime of charge carriers was obtained like earlier by fitting the plots to an exponential (TiO_2 or a double exponential fit (ZnO NC and solgel).

	TiO_2 solgel	ZnO NC	ZnO solgel
A_1	0.62769	0.0090218	0.0028678
A_2	-	0.13521	0.0097514
τ_1 (ns)	187.02	625.47	505.20
τ_2 (ns)	-	37.12	61.80

Table A.3: Coefficients for lifetime calculation from TRMC plots obtained by the fitting the data in single and double exponential equation.

Using equation A.2, the weighted lifetime values for charge carriers in ZnO NC and solgel films was calculated to be 73.92 ns and 162.57 ns respectively. Combining these values with the mobility of charge carriers (μ) obtained for each metal oxide layer, the diffusion length (L_D) of charge carriers was calculated using the following formula :

$$L_D = (6\frac{k_B T}{q}\tau\mu)^{1/2} \tag{A.2}$$

The resultant diffusion length values were 1.86 μm, 414.3 nm and 158.6 nm for TiO_2, ZnO NC and ZnO solgel films.
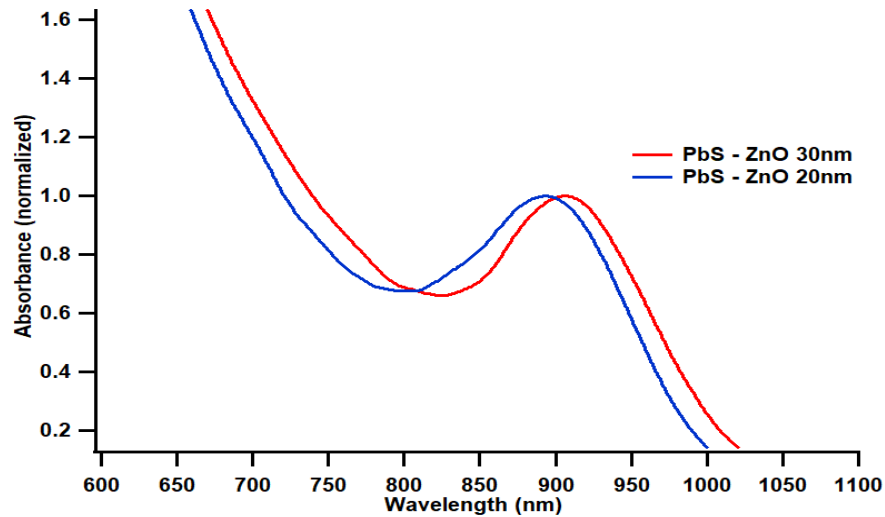
Figure A.10: Data for the J-V curves of the QDSC devices with 30 nm ZnO NC film was obtained from a different batch of PbS CQD solution as the 20 nm and 18 nm ZnO NC film QDSC devices. A comparison of the normalized absorption spectra of the two batches of PbS shows that the first exciton peak is nearly the same (905 nm for 30 nm film and 895 nm for the 20 nm and 18 nm films which translates to a band gap of 1.37 eV and 1.39 eV respectively [39])

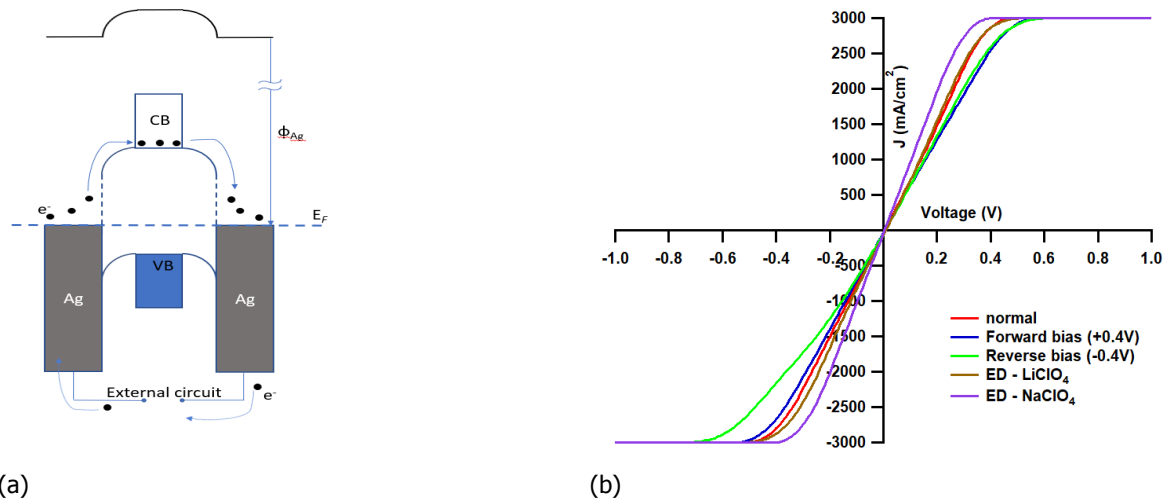(a)   (b)

Figure A.11: a. Possible bandbending in the metal-semiconductor-metal configuration under dark conditions. The junctions on both sides are ohmic in nature for electrons that probably allows their free movement during voltage scans b. A comparison of the effect of voltage soaking, and electrochemical doping of the PbS films in the metal-semiconductor-metal configuration. ED - refers to electrochemical doping.

Calculation of total mass of Lead used in the Thesis project

Total Number of devices = $\approx$150 (average of 3 devices a day, 3 times a week, 4 months)

Area of devices = 2.45 x 2.45 cm^2

Average thickness = 240 nm

Total volume of material used = 2.45 x 2.45 x 240 x 10^{-7} = 1440.6 x 10 $^{-7}$ c.c

Density of PbS = 7.6 g/c.c

Mass of PbS used in thesis = 7.6 x 1440.6 x 10^{-7} = 0.0010948 g

Mass of Pb used in thesis = $\frac{207}{239}$ x 0.0010948 = 0.000948 g = 0.948 mg

Bibliography

[1] EIA, *International Energy Outlook 2017 Overview,* U.S. Energy Information Administration **IEO2017**, 143 (2017), arXiv:EIA-0484(2013) [DOE] .

[2] NASA, *Climate change: How do we know?* .

[3] REN21, *Renewable and Sustainable Energy Reviews*, Vol. 72 (2017) pp. 1256–1270.

[4] International Renewable Energy Agency, *Renewable Energy Statistics 2017* (2017) p. 348.

[5] United Nations, *Paris Agreement,* 21st Conference of the Parties **21932**, 3 (2015), arXiv:arXiv:1011.1669v3 .

[6] R. Blandford and M. Watkins, *This Month in Physics History: April 25, 1954: Bell Labs Demonstrates the First Practical Silicon Solar Cell,* APS News **18**, 2 (2009).

[7] Kaneka Corpration, *New World Record Established for Conversion Efficiency in a Crystalline Silicon Solar Cell,* (2017).

[8] G. Carr, *Sunny Uplands,* (2012).

[9] *PV Market status,* .

[10] International Renewable Energy Agency (IRENA), *SpringerReference* (2014) pp. 1–8, arXiv:arXiv:1011.1669v3 .

[11] W. Shockley and H. J. Queisser, *Detailed balance limit of efficiency of p-n junction solar cells,* Journal of Applied Physics **32**, 510 (1961), arXiv:9809069v1 [arXiv:gr-qc] .

[12] G. Conibeer, *Third-generation photovoltaics,* Materials Today **10**, 42 (2007), arXiv:arXiv:1011.1669v3 .

[13] O. E. Semonin, J. M. Luther, and M. C. Beard, *Quantum dots for next-generation photovoltaics,* Materials Today **15**, 508 (2012).

[14] G. H. Carey, L. Levina, R. Comin, O. Voznyy, and E. H. Sargent, *Record charge carrier diffusion length in colloidal quantum dot solids via mutual dot-to-dot surface passivation,* Advanced Materials **27**, 3325 (2015).

[15] O. E. Semonin, O. E. Semonin, J. M. Luther, S. Choi, H.-y. Chen, J. Gao, A. J. Nozik, and M. C. Beard, *Peak external photocurrent quantum efficiency exceeding 100% via MEG in a Quantum Dot Solar Cell,* Science **334**, 1530 (2011).

[16] A. J. Nozik, M. C. Beard, J. M. Luther, M. Law, R. J. Ellingson, and J. C. Johnson, *Semiconductor quantum dots and quantum dot arrays and applications of multiple exciton generation to third-generation photovoltaic solar cells,* Chemical reviews **110**, 6873 (2010).

[17] E. M. Sanehira, A. R. Marshall, J. A. Christians, S. P. Harvey, P. N. Ciesielski, L. M. Wheeler, P. Schulz, L. Y. Lin, M. C. Beard, and J. M. Luther, *Enhanced mobility $CsPbI_3$ quantum dot arrays for record-efficiency, high-voltage photovoltaic cells,* Science Advances **3**, eaao4204 (2017).

[18] A. H. Smets, K. Jager, O. Isabella, R. A. Swaaij, and M. Zeman, *Solar Energy - The physics and engineering of photovoltaic conversion, technologies and systems*, January 2000 (UIT Cambridge Ltd., 2016).

[19] D. A. Neaman, *Semiconductor Physics and Devices: Basic Principles*, 4th ed. (McGraw-Hill COmpanies, Inc., 2012).

[20] T. L. Brown, H. E. LeMay Jr., B. E. Bursten, C. J. Murphy, and P. M. Woodward, *Chemistry, The central science*, 12th ed. (Pearson Education, Inc., 2012).

[21] C. R. Kagan, E. Lifshitz, E. H. Sargent, and D. V. Talapin, *Building devices from colloidal quantum dots,* Science **353** (2016), 10.1126/science.aac5523.

[22] A. J. Houtepen, *Charge injection and transport in quantum confined and disordered systems*, Ph.D. thesis, Utrecht University (2007).

[23] M. C. Beard, J. M. Luther, and A. J. Nozik, *The promise and challenge of nanostructured solar cells,* Nature Nanotechnology **9**, 951 (2014).

[24] C. B. Murray, D. J. Norris, and M. G. Bawendi, *Synthesis and Characterization of Nearly Monodisperse CdE (E = S, Se, Te) Semiconductor Nanocrystallites,* Journal of the American Chemical Society **115**, 8706 (1993), arXiv:93/1515-87 [0002-7863] .

[25] T. Sugimoto, F. Shiba, T. Sekiguchi, and H. Itoh, *Spontaneous nucleation of monodisperse silver halide particles from homogeneous gelatin solution I: Silver chloride,* Colloids and Surfaces A: Physicochemical and Engineering Aspects **164**, 183 (2000).

[26] C. R. Kagan and C. B. Murray, *Charge transport in strongly coupled quantum dot solids,* Nature Nanotechnology **10**, 1013 (2015).

[27] A. J. Nozik, *Specrtoscopy and hot electron relaxation dynamics in Semiconductor quantum wells and quantum dots,* Renewable Energy , 193 (2001).

[28] P. Kambhampati, *Hot exciton relaxation dynamics in semiconductor quantum dots: Radiationless transitions on the nanoscale,* Journal of Physical Chemistry C **115**, 22089 (2011).

[29] V. I. Klimov, *Optical Nonlinearities and Ultrafast Carrier Dynamics in Semiconductor Nanocrystals,* The Journal of Physical Chemistry B **104**, 6112 (2000).

[30] P. Guyot-Sionnest, M. Shim, C. Matranga, and M. Hines, *Intraband relaxation in cdse quantum dots,* Phys. Rev. B **60**, R2181 (1999).

[31] S. Xu, A. A. Mikhailovsky, J. A. Hollingsworth, and V. I. Klimov, *Hole intraband relaxation in strongly confined quantum dots: Revisiting the "phonon bottleneck" problem,* Phys. Rev. B **65**, 045319 (2002).

[32] D. Bozyigit, N. Yazdani, M. Yarema, O. Yarema, W. M. M. Lin, S. Volk, K. Vuttivorakulchai, M. Luisier, F. Juranyi, and V. Wood, *Soft surfaces of nanomaterials enable strong phonon interactions,* Nature **531**, 618 (2016), arXiv:NIHMS150003 .

[33] M. C. Beard, J. M. Luther, O. E. Semonin, and A. J. Nozik, *Third generation photovoltaics based on multiple exciton generation in quantum confined semiconductors,* Accounts of Chemical Research **46**, 1252 (2013).

[34] M. C. Beard, *Multiple exciton generation in semiconductor quantum dots,* Journal of Physical Chemistry Letters **2**, 1282 (2011).

[35] V. I. Klimov and D. W. McBranch, *Femtosecond $1P$-to-$1S$ electron relaxation in strongly confined semiconductor nanocrystals,* Phys. Rev. Lett. **80**, 4028 (1998).

[36] C. B. Murray, a. C. Kagan, and M. Bawendi, *Synthesis and characterization of monodisperse nanocrystals and close-packed nanocrystal assemblies,* Annual Review of Materials Science **30**, 545 (2000).

[37] M. A. Hines and G. D. Scholes, *Colloidal PbS Nanocrystals with Size-Tunable Near-Infrared Emission: Observation of Post-Synthesis Self-Narrowing of the Particle Size Distribution,* Advanced Materials **15**, 1844 (2003).

[38] L. Cademartiri, J. Bertolotti, R. Sapienza, D. S. Wiersma, G. Von Freymann, and G. A. Ozin, *Multigram scale, solventless, and diffusion-controlled route to highly monodisperse PbS nanocrystals*, Journal of Physical Chemistry B **110**, 671 (2006).

[39] I. Moreels, K. Lambert, D. D. Muynck, F. Vanhaecke, D. Poelman, J. C. Martins, G. Allan, and Z. Hens, *Size-Dependent Optical Properties of Colloidal {PbS} Quantum Dots*, ACS Nano **3**, 3023 (2009).

[40] I. Moreels, Y. Justo, B. De Geyter, K. Haustraete, J. C. Martins, and Z. Hens, *Size-tunable, bright, and stable PbS quantum dots: A surface chemistry study*, ACS Nano **5**, 2004 (2011).

[41] M. C. Weidman, M. E. Beck, R. S. Hoffman, F. Prins, and W. A. Tisdale, *Monodisperse, air-stable PbS nanocrystals via precursor stoichiometry control*, ACS Nano **8**, 6363 (2014).

[42] J. Zhang, J. Gao, E. M. Miller, J. M. Luther, and M. C. Beard, *Diffusion-controlled synthesis of PbS and PbSe quantum dots with in situ halide passivation for quantum dot solar cells*, ACS Nano **8**, 614 (2014).

[43] J. M. Pietryga, D. J. Werder, D. J. Williams, J. L. Casson, R. D. Schaller, V. I. Klimov, and J. A. Hollingsworth, *Utilizing the lability of lead selenide to produce heterostructured nanocrystals with bright, stable infrared emission*, Journal of the American Chemical Society **130**, 4879 (2008).

[44] J. Zhang, B. D. Chernomordik, R. W. Crisp, D. M. Kroupa, J. M. Luther, E. M. Miller, J. Gao, and M. C. Beard, *Preparation of Cd/Pb Chalcogenide Heterostructured Janus Particles via Controllable Cation Exchange*, ACS Nano **9**, 7151 (2015).

[45] M. P. Hendricks, M. P. Campos, G. T. Cleveland, I. J.-l. Plante, and J. S. Owen, *Substituted Thioureas : A Tunable Library of Precursors to Metal Sulfide Nanocrystals*, Science (2015), 10.1126/science.aaa2951.

[46] Y. Cho, B. Hou, J. Lim, S. Lee, S. Pak, J. Hong, P. Giraud, A. R. Jang, Y. W. Lee, J. Lee, J. E. Jang, H. J. Snaith, S. M. Morris, J. I. Sohn, S. Cha, and J. M. Kim, *Balancing Charge Carrier Transport in a Quantum Dot P-N Junction toward Hysteresis-Free High-Performance Solar Cells*, ACS Energy Letters **3**, 1036 (2018).

[47] A. G. Pattantyus-abraham, �. I. J. Kramer, �. A. R. Barkhouse, X. Wang, G. Konstantatos, R. Debnath, L. Levina, I. Raabe, M. K. Nazeeruddin, and E. H. Sargent, *Depleted-Heterojunction Colloidal Quantum Dot Solar Cells*, ACS Nano **4**, 3374 (1800).

[48] P. Hoyer and R. Könenkamp, *Photoconduction in porous TiO2 sensitized by PbS quantum dots*, Applied Physics Letters **66**, 349 (1995).

[49] T. Ju, R. L. Graham, G. Zhai, Y. W. Rodriguez, A. J. Breeze, L. Yang, G. B. Alers, and S. A. Carter, *High efficiency mesoporous titanium oxide PbS quantum dot solar cells at low temperature*, Applied Physics Letters **97**, 3 (2010).

[50] J. M. Luther, M. Law, M. C. Beard, Q. Song, M. O. Reese, R. J. Ellingson, and A. J. Nozik, *Schottky solar cells based on colloidal nanocrystal films*, Nano Letters **8**, 3488 (2008).

[51] K. W. Johnston, A. G. Pattantyus-Abraham, J. P. Clifford, S. H. Myrskog, S. Hoogland, H. Shukla, E. J. Klem, L. Levina, and E. H. Sargent, *Efficient Schottky-quantum-dot photovoltaics: The roles of depletion, drift, and diffusion*, Applied Physics Letters **92** (2008), 10.1063/1.2896295.

[52] P. R. Brown, D. Kim, R. R. Lunt, N. Zhao, M. G. Bawendi, J. C. Grossman, and V. Bulovi, *Energy Level Modification in Lead Sulfide Quantum Dot Thin Films through Ligand Exchange*, ACS nano **8**, 1 (2014).

[53] A. R. Kirmani, A. Kiani, M. M. Said, O. Voznyy, N. Wehbe, G. Walters, S. Barlow, E. H. Sargent, S. R. Marder, and A. Amassian, *Remote molecular doping of colloidal quantum dot photovoltaics*, ACS Energy Letters **1**, 922 (2016).

[54] C.-h. M. Chuang, P. R. Brown, V. Bulović, and M. G. Bawendi, *Improved performance and stability in quantum dot solar cells through band alignment engineering,* Nature Materials **13**, 796 (2014).

[55] X. Lan, O. Voznyy, A. Kiani, F. P. García De Arquer, A. S. Abbas, G. H. Kim, M. Liu, Z. Yang, G. Walters, J. Xu, M. Yuan, Z. Ning, F. Fan, P. Kanjanaboos, I. Kramer, D. Zhitomirsky, P. Lee, A. Perelgut, S. Hoogland, and E. H. Sargent, *Passivation Using Molecular Halides Increases Quantum Dot Solar Cell Performance,* Advanced Materials **28**, 299 (2016).

[56] X. Lan, O. Voznyy, F. P. García De Arquer, M. Liu, J. Xu, A. H. Proppe, G. Walters, F. Fan, H. Tan, M. Liu, Z. Yang, S. Hoogland, and E. H. Sargent, *10.6% Certified Colloidal Quantum Dot Solar Cells Via Solvent-Polarity-Engineered Halide Passivation,* Nano Letters **16**, 4630 (2016), arXiv:1408.1149 .

[57] Y. Wang, K. Lu, L. Han, Z. Liu, G. Shi, H. Fang, S. Chen, T. Wu, F. Yang, M. Gu, S. Zhou, X. Ling, X. Tang, J. Zheng, M. A. Loi, and W. Ma, *In Situ Passivation for Efficient PbS Quantum Dot Solar Cells by Precursor Engineering,* Advanced Materials **1704871**, 1 (2018).

[58] M. Liu, F. P. G. De Arquer, Y. Li, X. Lan, G. H. Kim, O. Voznyy, L. K. Jagadamma, A. S. Abbas, S. Hoogland, Z. Lu, J. Y. Kim, A. Amassian, and E. H. Sargent, *Double-Sided Junctions Enable High-Performance Colloidal-Quantum-Dot Photovoltaics,* Advanced Materials **28**, 4142 (2016).

[59] K. Lu, Y. Wang, Z. Liu, L. Han, G. Shi, H. Fang, J. Chen, X. Ye, S. Chen, F. Yang, A. G. Shulga, T. Wu, M. Gu, S. Zhou, J. Fan, M. A. Loi, and W. Ma, *High-Efficiency PbS Quantum-Dot Solar Cells with Greatly Simplified Fabrication Processing via " Solvent-Curing ",* Advanced Materials **1707572**, 1 (2018).

[60] M. Liu, O. Voznyy, R. Sabatini, F. P. García De Arquer, R. Munir, A. H. Balawi, X. Lan, F. Fan, G. Walters, A. R. Kirmani, S. Hoogland, F. Laquai, A. Amassian, and E. H. Sargent, *Hybrid organic-inorganic inks flatten the energy landscape in colloidal quantum dot solids,* Nature Materials **16**, 258 (2017).

[61] J. Choi, Y. Kim, J. W. Jo, J. Kim, B. Sun, G. Walters, F. P. García de Arquer, R. Quintero-Bermudez, Y. Li, C. S. Tan, L. N. Quan, A. P. T. Kam, S. Hoogland, Z. Lu, O. Voznyy, and E. H. Sargent, *Chloride Passivation of ZnO Electrodes Improves Charge Extraction in Colloidal Quantum Dot Photovoltaics,* Advanced Materials **29**, 1 (2017).

[62] K. S. Jeong, J. Tang, H. Liu, J. Kim, A. W. Schaefer, K. Kemp, L. Levina, X. Wang, S. Hoogland, R. Debnath, L. Brzozowski, E. H. Sargent, and J. B. Asbury, *Enhanced mobility-lifetime products in PbS colloidal quantum dot photovoltaics,* ACS Nano **6**, 89 (2012).

[63] R. W. Crisp, D. M. Kroupa, A. R. Marshall, E. M. Miller, J. Zhang, M. C. Beard, and J. M. Luther, *Metal Halide Solid-State Surface Treatment for High Efficiency PbS and PbSe QD Solar Cells,* Scientific Reports **5**, 1 (2015).

[64] A. H. Ip, S. M. Thon, S. Hoogland, O. Voznyy, D. Zhitomirsky, R. Debnath, L. Levina, L. R. Rollny, G. H. Carey, A. Fischer, K. W. Kemp, I. J. Kramer, Z. Ning, A. J. Labelle, K. W. Chou, A. Amassian, and E. H. Sargent, *Hybrid passivated colloidal quantum dot solids,* Nature Nanotechnology **7**, 577 (2012).

[65] Z. Ning, Y. Ren, S. Hoogland, O. Voznyy, L. Levina, P. Stadler, X. Lan, D. Zhitomirsky, and E. H. Sargent, *All-inorganic colloidal quantum dot photovoltaics employing solution-phase halide passivation,* Advanced Materials **24**, 6295 (2012).

[66] Z. Ning, O. Voznyy, J. Pan, S. Hoogland, V. Adinolfi, J. Xu, M. Li, A. R. Kirmani, J. P. Sun, J. Minor, K. W. Kemp, H. Dong, L. Rollny, A. Labelle, G. Carey, B. Sutherland, I. Hill, A. Amassian, H. Liu, J. Tang, O. M. Bakr, and E. H. Sargent, *Air-stable n-type colloidal quantum dot solids,* Nature Materials **13**, 822 (2014).

[67] Z. Ning, H. Dong, Q. Zhang, O. Voznyy, and E. H. Sargent, *Solar Cells Based on Inks of n □ Type Colloidal Quantum Dots,* ACS Nano , 10321 (2014).

[68] A. Kiani, B. R. Sutherland, Y. Kim, O. Ouellette, L. Levina, G. Walters, C. T. Dinh, M. Liu, O. Voznyy, X. Lan, A. J. Labelle, A. H. Ip, A. Proppe, G. H. Ahmed, O. F. Mohammed, S. Hoogland, and E. H. Sargent, *Single-step colloidal quantum dot films for infrared solar harvesting,* Applied Physics Letters **109** (2016), 10.1063/1.4966217.

[69] I. J. Kramer and E. H. Sargent, *The Architecture of Colloidal Quantum Dot Solar Cells : Materials to Devices,* Chemical Reviews (2014).

[70] S. M. Willis, C. Cheng, H. E. Assender, and A. A. Watt, *The transitional heterojunction behavior of PbS/ZnO colloidal quantum dot solar cells,* Nano Letters **12**, 1522 (2012).

[71] A. R. Kirmani, F. P. García De Arquer, J. Z. Fan, J. I. Khan, G. Walters, S. Hoogland, N. Wehbe, M. M. Said, S. Barlow, F. Laquai, S. R. Marder, E. H. Sargent, and A. Amassian, *Molecular Doping of the Hole-Transporting Layer for Efficient, Single-Step-Deposited Colloidal Quantum Dot Photovoltaics,* ACS Energy Letters **2**, 1952 (2017).

[72] M. J. Speirs, D. M. Balazs, D. N. Dirin, M. V. Kovalenko, and M. A. Loi, *Increased efficiency in pn-junction PbS QD solar cells via NaHS treatment of the p-type layer,* Applied Physics Letters **110** (2017), 10.1063/1.4978444.

[73] Z. Ren, Z. Kuang, L. Zhang, J. Sun, X. Yi, Z. Pan, X. Zhong, J. Hu, A. Xia, and J. Wang, *Enhancing Electron and Hole Extractions for Efficient PbS Quantum Dot Solar Cells,* Solar RRL **1**, 1700176 (2017).

[74] R. Azmi, H. Aqoma, W. T. Hadmojo, J. M. Yun, S. Yoon, K. Kim, Y. R. Do, S. H. Oh, and S. Y. Jang, *Low-Temperature-Processed 9% Colloidal Quantum Dot Photovoltaic Devices through Interfacial Management of p-n Heterojunction,* Advanced Energy Materials **6**, 1 (2016).

[75] Z. Jin, M. Yuan, H. Li, H. Yang, Q. Zhou, H. Liu, X. Lan, M. Liu, J. Wang, E. H. Sargent, and Y. Li, *Graphdiyne : An Efficient Hole Transporter for Stable High-Performance Colloidal Quantum Dot Solar Cells,* Advanced functional materials , 5284 (2016).

[76] Y. Zhang, G. Wu, C. Ding, F. Liu, Q. Huang, Y. Ogomi, S. Hayase, T. Toyoda, R. Wang, J. Otsuki, and Q. Shen, *Improvement of Photovoltaic Performance of Colloidal Quantum Dot Solar Cells Using Organic Small Molecule as Hole-Selective Layer,* Journal of Physical Chemistry Letters (2017), 10.1021/acs.jpclett.7b00683.

[77] Y. J. Jeong, J. H. Song, S. Jeong, and S. J. Baik, *PbS Colloidal Quantum Dot Solar Cells with Organic Hole Transport Layers for Enhanced Carrier Separation and Ambient Stability,* IEEE Journal of Photovoltaics **8**, 493 (2018).

[78] J. Tang, H. Liu, D. Zhitomirsky, S. Hoogland, X. Wang, M. Furukawa, L. Levina, and E. H. Sargent, *Quantum Junction Solar Cells Supplementary Information,* Nano Letters **12**, 4889 (2012).

[79] J. Gao, J. M. Luther, O. E. Semonin, R. J. Ellingson, A. J. Nozik, and M. C. Beard, *Quantum Dot Size Dependent $J - V$ Characteristics in Heterojunction ZnO/PbS Quantum Dot Solar Cells,* Nano Letters **11**, 1002 (2011).

[80] J. Gao, C. L. Perkins, J. M. Luther, M. C. Hanna, H. Y. Chen, O. E. Semonin, A. J. Nozik, R. J. Ellingson, and M. C. Beard, *N-type transition metal oxide as a hole extraction layer in PbS quantum dot solar cells,* Nano Letters **11**, 3263 (2011).

[81] A. M. Schimpf, K. E. Knowles, G. M. Carroll, and D. R. Gamelin, *Electronic Doping and Redox-Potential Tuning in Colloidal Semiconductor Nanocrystals,* Accounts of Chemical Research **48**, 1929 (2015).

[82] S. Gudjonsdottir, W. van der Stam, N. Kirkwood, W. H. Evers, and A. J. Houtepen, *The role of dopant ions on charge injection and transport in electrochemically doped quantum dot films,* Journal of the American Chemical Society , jacs.8b01347 (2018).

[83] Y. Hu, Z. D. Rengert, C. McDowell, M. J. Ford, M. Wang, A. Karki, A. T. Lill, G. C. Bazan, and T. Q. Nguyen, *Doping Polymer Semiconductors by Organic Salts: Toward High-Performance Solution-Processed Organic Field-Effect Transistors,* ACS Nano **12**, 3938 (2018).

[84] A. Wood, M. Giersig, M. Hilgendorff, A. Vilas-Campos, L. M. Liz-Marzán, and P. Mulvaney, *Size Effects in Zno: The Cluster to Quantum Dot Transition,* Australian Journal of Chemistry **56**, 1051 (2003).

[85] *High-efficiency quantum-dot light-emitting devices with enhanced charge injection,* Nature Photonics **7**, 407 (2013).

[86] M. Ohyama, H. Kozuka, and T. Yoko, *Sol-Gel Preparation of Transparent and Conductive Aluminum-Doped Zinc Oxide Films with Highly Preferential Crystal Orientation,* Journal of the American Ceramic Society **81**, 1622 (2005).

[87] B. D. Chernomordik, A. R. Marshall, G. F. Pach, J. M. Luther, and M. C. Beard, *Quantum Dot Solar Cell Fabrication Protocols,* (2017).

[88] H. Zhang, B. R. Hyun, F. W. Wise, and R. D. Robinson, *A generic method for rational scalable synthesis of monodisperse metal sulfide nanocrystals,* Nano Letters **12**, 5856 (2012).

[89] C. H. Cheung, W. J. Song, and S. K. So, *Role of air exposure in the improvement of injection efficiency of transition metal oxide/organic contact,* Organic Electronics: physics, materials, applications **11**, 89 (2010).

[90] C.-H. M. Chuang, A. Maurano, R. E. Brandt, G. W. Hwang, J. Jean, T. Buonassisi, V. Bulović, and M. G. Bawendi, *Open-circuit voltage deficit, radiative sub-bandgap states, and prospects in quantum dot solar cells,* Nano Letters **15**, 3286 (2015), pMID: 25927871.

[91] J. Tang, K. W. Kemp, S. Hoogland, K. S. Jeong, H. Liu, L. Levina, M. Furukawa, X. Wang, R. Debnath, D. Cha, K. W. Chou, A. Fischer, A. Amassian, J. B. Asbury, and E. H. Sargent, *Colloidal-quantum-dot photovoltaics using atomic-ligand passivation,* Nature Materials **10**, 765 (2011).

[92] J. Tang, L. Brzozowski, D. A. R. Barkhouse, X. Wang, R. Debnath, R. Wolowiec, E. Palmiano, L. Levina, A. G. Pattantyus-Abraham, D. Jamakosmanovic, and E. H. Sargent, *Quantum dot photovoltaics in the extreme quantum confinement regime: The surface-chemical origins of exceptional air- and light-stability,* ACS Nano **4**, 869 (2010), arXiv:1011.1669v3 .

[93] B. Martín-García, Y. Bi, M. Prato, D. Spirito, R. Krahne, G. Konstantatos, and I. Moreels, *Reduction of moisture sensitivity of PbS quantum dot solar cells by incorporation of reduced graphene oxide,* Solar Energy Materials and Solar Cells **183**, 1 (2018).

[94] P. Rekemeyer, C.-H. M. Chuang, M. G. Bawendi, and S. Gradecak, *Minority Carrier Transport in Lead Sulfide Quantum Dot Photovoltaics,* Nano Letters , acs.nanolett.7b02916 (2017).

[95] T. J. Savenije, A. J. Ferguson, N. Kopidakis, and G. Rumbles, *Revealing the dynamics of charge carriers in polymer:fullerene blends using photoinduced time-resolved microwave conductivity,* Journal of Physical Chemistry C **117**, 24085 (2013).

[96] P. M. Sommeling, B. C. O'Regan, R. R. Haswell, H. J. P. Smit, N. J. Bakker, J. J. T. Smits, J. M. Kroon, and J. A. M. Van Roosmalen, *Influence of a TiCl4 post-treatment on nanocrystalline TiO 2 films in dye-sensitized solar cells,* Journal of Physical Chemistry B **110**, 19191 (2006).

Acknowledgements

The past one year at the OM group of the Applied sciences faculty has been an amazing experience and I would like to thank everyone of you who has been a part of my journey that has culminated in my master thesis.

To begin with, Ryan, thank you for being an amazing mentor. You have been nothing short of spectacular in teaching, guiding and motivating me in conducting scientific research. You pushed through trying times while training me though the basics of lab work and while at times I wonder how you did it (God bless you for that !), I'm also super grateful that you did it. Your inputs to this thesis have been invaluable and I will always be grateful for those innumerable times you took time off your busy schedule to patiently iron out the wrinkles in my understanding of fundamental concepts.

Arjan, thank you for giving me this wonderful opportunity to have worked on a topic of my choice. I still vividly remember the day I sat in your office to talk to you about my interest in quantum dot solar cells and though its been a long journey (it sure did feel so!), I think I've come out of it a more knowledgeable person. I must admit, there were times when I doubted my ability to continue with the group but I guess it was your enthusiasm at that 5% device that partially kept me from quitting. And speaking of the 5% device, thank you for that wonderful dinner :). I would also like to thank you for your valuable inputs during our biweekly Monday morning discussions that helped me shape the course of my research.

Next, I'd like to thank all the other post docs and PhD students of the OM group. I have enjoyed all our discussions, however short they may have been have. A special thanks to Solrun for helping me out with the zinc oxide synthesis (which got me to my 5% device ;)). I guess its safe to assume that I've been around for a while when I say that I've seen more than two batches of bachelor students come and go in the student room but guys, coming to work everyday wouldn't have been fun if it weren't for you all. A special shout out to Bob and Vidya for your kind words of encouragement and burning the midnight oil along side me in my quest to achieve my 5% device.

Also, I would like to thank my family back in India for providing me with the opportunity to study abroad at TU Delft and their moral support throughout this journey. Finally, Saranya, I can't thank you enough for the innumerable times you put up with me (over the phone) when the going got tough and for cheering me up when I needed it the most.